

## Experimental Observation of Non-Ideal Compressible Fluid Dynamics with Application in Organic Rankine Cycle Power Systems

Mathijssen, Tiemo

**DOI**

[10.4233/uuid:147f6475-1b33-4a5a-9e65-abe63a3865ff](https://doi.org/10.4233/uuid:147f6475-1b33-4a5a-9e65-abe63a3865ff)

**Publication date**

2017

**Document Version**

Final published version

**Citation (APA)**

Mathijssen, T. (2017). *Experimental Observation of Non-Ideal Compressible Fluid Dynamics: with Application in Organic Rankine Cycle Power Systems*. [Dissertation (TU Delft), Delft University of Technology]. <https://doi.org/10.4233/uuid:147f6475-1b33-4a5a-9e65-abe63a3865ff>

**Important note**

To cite this publication, please use the final published version (if applicable).  
Please check the document version above.

**Copyright**

Other than for strictly personal use, it is not permitted to download, forward or distribute the text or part of it, without the consent of the author(s) and/or copyright holder(s), unless the work is under an open content license such as Creative Commons.

**Takedown policy**

Please contact us and provide details if you believe this document breaches copyrights.  
We will remove access to the work immediately and investigate your claim.

**EXPERIMENTAL OBSERVATION OF NON-IDEAL  
COMPRESSIBLE FLUID DYNAMICS**

WITH APPLICATION IN ORGANIC RANKINE CYCLE POWER SYSTEMS



# **EXPERIMENTAL OBSERVATION OF NON-IDEAL COMPRESSIBLE FLUID DYNAMICS**

WITH APPLICATION IN ORGANIC RANKINE CYCLE POWER SYSTEMS

## **Proefschrift**

ter verkrijging van de graad van doctor  
aan de Technische Universiteit Delft,  
op gezag van de Rector Magnificus prof. ir. K. C. A. M. Luyben,  
voorzitter van het College voor Promoties,  
in het openbaar te verdedigen op maandag 29 mei 2017 om 10:00 uur

door

**Tiemo MATHIJSEN**

ingenieur luchtvaart en ruimtevaart  
geboren te Bandung, Indonesië.

Dit proefschrift is goedgekeurd door de promotoren:

Prof. dr. P. Colonna  
Prof. dr. A. Guardone

Samenstelling promotiecommissie:

Rector Magnificus  
Prof. dr. P. Colonna  
Prof. dr. A. Guardone

voorzitter  
Technische Universiteit Delft, promotor  
Politecnico di Milano, promotor

Onafhankelijke leden:

O-Univ. Prof. Dipl.-Ing. Dr. Tech. A. Kluwick  
Prof. dr. D.J.E.M. Roekaerts  
Prof. dr. S. Hickel  
Dr. A. Wheeler  
K. Link  
Prof. dr. F. Scarano

Technische Universität Wien  
Technische Universiteit Delft  
Technische Universiteit Delft  
Cambridge University  
Siemens AG  
Technische Universiteit Delft, reservelid



This research is funded by the Dutch Technology Foundation STW, Applied Science Division of NWO, the Technology Program of the Dutch Ministry of Economic Affairs (grant # 11143).

*Keywords:* Non-ideal compressible fluid dynamics, nonclassical gasdynamics, dense gas dynamics, rarefaction shock wave, shock tube, liquid-vapour critical point, dynamic modeling

*Printed by:* Ipskamp drukkers

*Front & Back:* Schlieren image during the starting process in a reflection nozzle. © H.O. Amann.

Copyright © 2017 by T. Mathijssen

ISBN 978-94-92516-53-4

An electronic version of this dissertation is available at  
<http://repository.tudelft.nl/>.

# CONTENTS

|   |           |
|---|-----------|
| <b>Summary</b>  | <b>1</b>  |
| <b>Samenvatting</b>   | <b>5</b>  |
| <b>1 Introduction</b>   | <b>9</b>  |
| 1.1 Non-ideal compressible fluid dynamics . . . . .   | 9         |
| 1.2 Theory of non-ideal compressible fluid dynamics . . . . .   | 10        |
| 1.3 Compressions in the nonclassical regime . . . . .   | 16        |
| 1.4 Expansions in the nonclassical regime . . . . .   | 18        |
| 1.5 NICFD flows in shock tubes . . . . .  | 21        |
| 1.6 Applications . . . . .  | 25        |
| 1.7 Motivation for the study . . . . .  | 26        |
| 1.8 Outline of the thesis . . . . .   | 26        |
| <b>2 Flexible Asymmetric Shock Tube: a facility for wave propagation speed measurements in dense gases</b>                                  | <b>27</b> |
| 2.1 Introduction . . . . .  | 27        |
| 2.2 The FAST and the experimental procedure . . . . .   | 28        |
| 2.2.1 Equipment & procedure . . . . .   | 28        |
| 2.2.2 Instruments, Data acquisition & Control . . . . .   | 34        |
| 2.3 Facility characterization . . . . .   | 36        |
| 2.3.1 Vacuum and pressure sealing . . . . .   | 36        |
| 2.3.2 Compression shock experiment in nitrogen . . . . .  | 37        |
| 2.3.3 Rarefaction wave experiments using incondensable gases . . . . .  | 39        |
| 2.4 Rarefaction waves in siloxane D <sub>6</sub> . . . . .  | 44        |
| 2.5 Conclusion & Future Work . . . . .  | 48        |
| <b>3 Gasdynamic experiments in the predicted BZT region of siloxane D<sub>6</sub></b>   | <b>51</b> |
| 3.1 Introduction . . . . .  | 51        |
| 3.2 Thermodynamic conditions . . . . .  | 52        |
| 3.3 Wave speed measurements . . . . .   | 61        |
| 3.4 Shock formation? . . . . .  | 64        |
| 3.5 Prediction of experimental value of $T$ . . . . .   | 71        |
| 3.6 Conclusion & Recommendations . . . . .  | 73        |
| <b>4 Simulations of NICFD shock tube flows in the vapour-liquid critical point region using a thermodynamic model based on scaling laws</b> | <b>77</b> |
| 4.1 Introduction . . . . .  | 77        |
| 4.2 Thermodynamic model . . . . .   | 79        |
| 4.3 Numerical solver . . . . .  | 81        |

|          |  |            |
|----------|--|------------|
| 4.4      | Simulation results . . . . .   | 82         |
| 4.4.1    | Simulations of nonclassical waves in methane . . . . .                                     | 82         |
| 4.4.2    | Shock formation . . . . .  | 88         |
| 4.4.3    | Simulation of transcritical nonclassical flows starting from single phase states . . . . . | 93         |
| 4.5      | Conclusion . . . . .   | 99         |
| <b>5</b> | <b>Dynamic modeling of ORC Power Systems</b>   | <b>101</b> |
| 5.1      | Introduction . . . . .   | 101        |
| 5.2      | Modeling Methodology . . . . .   | 103        |
| 5.2.1    | Requirements . . . . .   | 103        |
| 5.2.2    | Object-Oriented Modeling . . . . .   | 104        |
| 5.2.3    | Model Re-Use . . . . .   | 104        |
| 5.3      | Case Study: a 150 kW <sub>e</sub> High-Temperature Turbogenerator . . . . .                | 105        |
| 5.4      | System Model . . . . .   | 107        |
| 5.4.1    | Model Modularity . . . . .   | 107        |
| 5.4.2    | Turbo-Pump and Electrical Generator Models . . . . .                                       | 108        |
| 5.4.3    | Evaporator . . . . .   | 109        |
| 5.4.4    | Recuperator . . . . .  | 110        |
| 5.4.5    | Condenser . . . . .  | 111        |
| 5.4.6    | Lubrication Circuit and Other Piping . . . . .   | 111        |
| 5.4.7    | Working Fluid . . . . .  | 111        |
| 5.4.8    | Control System. . . . .  | 112        |
| 5.4.9    | Outlook . . . . .  | 112        |
| 5.5      | Validation . . . . .   | 113        |
| 5.5.1    | Experimental Apparatus . . . . .   | 113        |
| 5.5.2    | Measurements and Experiments . . . . .   | 113        |
| 5.5.3    | Simulations . . . . .  | 115        |
| 5.5.4    | Results . . . . .  | 115        |
| 5.6      | Perspectives on Challenging Control Problems . . . . .                                     | 118        |
| 5.7      | Concluding Remarks . . . . .   | 123        |
| <b>6</b> | <b>Conclusion &amp; Outlook</b>  | <b>125</b> |
|          | <b>Bibliography</b>  | <b>127</b> |
|          | <b>Acknowledgements</b>  | <b>135</b> |
|          | <b>Curriculum Vitae</b>  | <b>137</b> |

# SUMMARY

Non-ideal compressible fluid dynamics (NICFD) is the branch of fluid dynamics dealing with flows, whose fluid properties deviate from those of the ideal gas. Typically such flows occur in the dense gas, supercritical and liquid-vapour mixture domain. A good indicator to determine whether a flow can be classified as pertaining to NICFD, is the fundamental derivative of gasdynamics  $\Gamma$ . In ideal gases, the value of  $\Gamma$  is constant. NICFD occurs whenever the value of  $\Gamma$  is variable among the thermodynamic states of the considered fluid flow. In case the fluid is in thermodynamic states featuring negative values of  $\Gamma$ , nonclassical gasdynamic flow features can be exhibited, such as dilating compression fans, steepening of isentropic rarefaction waves, and rarefaction shock waves (RSWs).

NICFD is encountered in a variety of industrial processes. Notable examples in the energy sector are turbine flows in organic Rankine cycle power plants, compressor flows in supercritical CO<sub>2</sub> power systems, and CO<sub>2</sub> capture and sequestration processes. In refrigeration and heat pump systems, such flows occur in the dense-gas and liquid-vapour two-phase regime of throttling valves, compressors and ejectors. Other examples in which NICFD is encountered include turbo-machinery, pipe flow and nozzle flows in the oil and gas industry, and CO<sub>2</sub> nozzles in the pharmaceutical industry. Experimental data in dense vapours of high molecular fluids and on NICFD flows is scarce. Measurements of dense gas flows of complex organic fluids contribute to the improvement of thermodynamic models and to the understanding of NICFD. Moreover, despite the theory of nonclassical gasdynamics being well established, no compelling experimental evidence of nonclassical phenomena is available in literature. Measurements of an RSW would provide the validation of NICFD theory. The objective of the research documented in this dissertation is experimental study of NICFD flows. In particular, the generation and measurement of nonclassical flow phenomena, such as RSWs, would be of particular scientific interest, given their peculiarity and the absence of incontrovertible experimental proof of their existence.

To this end, the Flexible Asymmetric Shock Tube (FAST) is commissioned at Delft University of Technology. It is a 9-meter-long stainless steel shock tube complemented with a vapour generator and a flow return pipe, creating a closed sealed system that can be filled with a large variety of fluids. The fluid can be heated and kept any desired pressure or temperature within the facility limitations of 20 bar and 400 °C. A fast-acting valve opens to generate a rarefaction or compression wave. Four high-speed pressure transducers record the propagating wave at different locations in the tube, which are correlated to retrieve the wave propagation speed. A series of experiments in incondensable gases is conducted for validation purposes. First, a compression shock wave in nitrogen is generated. The wave propagation speed is found within 0.5 % of the theoretical value predicted with the Rankine-Hugoniot equations. In addition, a rise time of 30  $\mu$ s for the pressure transducers is estimated. Second, rarefaction experiments are conducted in several gases, and a method devised to estimate the speed



of sound. The calculated speeds of sound are within approximately 2 % of theoretical values.

Finally, rarefaction experiments in siloxane D<sub>6</sub> are conducted at various pressure and temperature levels. The local wave propagation speed is found to be within 8 % of the theoretically predicted value, and the speed of sound differs 1.6 % of the value, predicted by the arguably best available thermodynamic model. This difference is surprisingly small, given the large uncertainty of the thermodynamic model. A total of 5 experiments with thermodynamic conditions inside, and in the vicinity of the predicted negative- $\Gamma$  region are successfully conducted. These experiments confirm the feasibility of the original idea. Moreover, the measurements support the validity of the NICFD theory in several ways. For example, in a rarefaction experiment, the estimated speed of sound varies considerably for small variations of the thermodynamic states of the fluid, while the wave propagation speed variation is small, as must be the case of flows of fluids in thermodynamic states with  $\Gamma$  close to zero. Some observations of the results of experiments may suggest the occurrence of nonclassical phenomena, but more repeatable experiments will have to be performed in order to reach certainty about the existence of the inversion of gasdynamic features in flows.

Another region featuring negative  $\Gamma$  has recently been identified in the two-phase region in the vicinity of the vapour-liquid critical point of any compressible substance. Conventional thermodynamic models based on equations of state fail to accurately predict the thermodynamic quantities in the vapour-liquid critical point region, specifically in the case of derived quantities such as  $\Gamma$ . Only models based on so-called scaling laws are valid and accurate in this region. One such model is implemented in a in-house software for fluid thermodynamic properties estimation and linked to a fluid dynamic solver in order to numerically predict flows accurately in the vicinity of the vapour-liquid critical point. Simulations of shock tube flows are conducted to confirm the feasibility of the generation of nonclassical NICFD phenomena, and to aid in the design of experiments to validate their existence. For example, an experiment using CO<sub>2</sub> has been devised, in which both initial states in a shock tube are in the single-phase region and on the same isotherm. This greatly eases the realisation of the thermodynamic conditions and the test itself. Another scientifically interesting finding of this study is that the rarefaction shock admissibility region extends into the supercritical region, albeit marginally, for thermodynamic states very close to the vapour-liquid critical point.

Finally, more applied research on a system in which NICFD may occur is also conducted. The system is an organic Rankine cycle (ORC) power plant, in which the nozzle of the turbine operates in the NICFD regime. In order to study system dynamics and control, a library of fully modular and reusable component models was developed for dynamic lumped-element simulations. A case study was considered, namely the transient performance of a 150 kW turbogenerator system, which was fully modeled and simulated. The simulation results are validated against experimental data from two distinct sources. One source is from an operational power plant, which is used as a bottoming cycle, having the exhaust gas of two diesel engines as thermal energy supply. The other data source is an experimental campaign, utilizing a unit on a test bench, which is specifically carried out with the purpose to generate validation data. All simulated thermodynamic variables agree to within 1 % of the measured

value at steady-state operation of the plant. At 60 % of the original load, the accuracy of the model reduces to approximately 3 % of the measured value at steady-state operation. The main features of the transient response of the plant are predicted correctly, but in this case the difference between the calculated and the measure values can be as high as 25 %. Dynamic models of ORC systems obtained by reusing component models described here can thus be used in simulation studies aimed at improving control and transient operation of ORC power plants. Such systems can be used e.g. in waste-heat recovery in trucks, or in concentrated solar energy.



# SAMENVATTING

Niet-ideale compressibele vloeistofdynamica (NICFD) is de tak van stromingsleer dat zich bezig houdt met stromingen, waarbij de vloeistofeigenschappen afwijken van degene, die door de ideale gaswet gedicteerd worden. Zulk soort stromingen vindt typisch plaats in het domein van dichte gassen, superkritische vloeistoffen of mengsels van damp en vloeistof. Een goede indicator of een stroming als NICFD geklassificeerd kan worden, is de fundamentele afgeleide van de gasdynamica  $\Gamma$ . In ideale gassen is de waarde van  $\Gamma$  constant. NICFD vindt plaats zodra de waarde van  $\Gamma$  variabel is in de thermodynamische toestanden van de stroming. Als de stof zich in een toestand bevindt met een negatieve waarde van  $\Gamma$ , kunnen zich niet-klassieke stromingseigenschappen voordoen, zoals uitdijende compressiewaaiers, het steiler worden van isentrope expansiegolven, en expansie schokgolven (RSWs).

NICFD komt in verscheidene industriële processen voor. Voorbeelden in de energiesector zijn turbinestromingen in organische Rankine cyclus (ORC) energiecentrales, compressorstromingen in superkritische CO<sub>2</sub> energiecentrales, en CO<sub>2</sub> opvang- and scheidingsprocessen. In koel- en warmtepompsystemen komen zulke stromingen voor in het dichte-gas en het damp-vloeistof tweefasen regime van smookkleppen, compressoren en injectoren. Andere voorbeelden waarin NICFD voorkomt zijn turbomachines, pijpstromingen en straalbuizen in de olie- en gasindustrie, en CO<sub>2</sub> straalbuizen in de farmaceutische industrie. Experimentele data in dichte gassen van substanties met een hoog molecuulair gewicht en van NICFD stromingen is schaars. Metingen van stromingen in het dichte-gas regime van complexe organische fluïdi dragen bij aan het verbeteren van thermodynamische modellen en aan het begrijpen van NICFD. Ondanks dat de theorie van niet-klassieke gasdynamica reeds gevestigd is, is er bovendien geen overtuigend bewijs van niet-klassieke fenomenen beschikbaar in de literatuur. Metingen van een RSW zou het experimentele bewijs vormen van de NICFD theorie. Het doel van het onderzoek, dat in deze dissertatie beschreven is, is de experimentele studie naar NICFD stromingen. In het bijzonder zou het de wetenschappelijk interesse wekken, om niet-klassieke stromingsfenomenen, zoals RSW's, op te wekken en te meten, vanwege hun eigenaardigheid en vanwege de afwezigheid van onweerlegbaar experimenteel bewijs van hun bestaan.

Hiervoor is de Flexibele Asymmetrische Shockbuis (FAST) aan de Technische Universiteit Delft in bedrijf gesteld. Het is een 9-meter lange roestvast stalen schokbuis, waar een damp-generator en een terugstroompijp aan toegevoegd is, zodat het een dicht gesloten systeem vormt dat met een grote verscheidenheid aan vloeistoffen gevuld kan worden. De vloeistof kan worden verwarmd en op iedere gewenste druk en temperatuur gehouden worden binnen de grenzen van de faciliteit van 20 bar en 400 °C. Een snelwerkende klep opent om een expansie of compressiegolf te genereren. Vier hoge-snelheidsdruksensoren registreren de zich voortbewegende golf op verschillende plaatsen in de buis, die gecorreleerd worden om de voortplantingssnelheid te achterhalen. Een serie experimenten in oncondenseerbare

gassen zijn uitgevoerd op verschillende druk en temperatuurniveau's. Als eerste is een compressieschokgolf in stikstof opgewekt. De voortplantingssnelheid van de golf valt binnen 0.5 % van de theoretische waarde, welke met de Rankine-Hugoniot vergelijkingen is voorspeld. Tevens werd de aanlooptijd van de druksensoren op 30  $\mu\text{s}$  geschat. Als tweede zijn expansie-experimenten in verschillende gassen uitgevoerd, en is een methode ontwikkeld om de geluidssnelheid te achterhalen. De berekende geluidssnelheden vallen binnen circa 2 % van de theoretische waarden.

Uiteindelijk zijn expansie-experimenten in siloxaan  $\text{D}_6$  uitgevoerd op verschillende druk en temperatuurniveau's. De lokale golfvoortplantingssnelheid valt binnen 8 % van de theoretische voorspelde waarde, en de geluidssnelheid verschilt 1.6 % van de waarde die geschat is met het aannemelijk beste beschikbare thermodynamische model. Dit verschil is verbazingwekkend klein, gezien de grote onzekerheid van het thermodynamisch model. In totaal zijn 5 experimenten succesvol uitgevoerd met thermodynamische condities binnen, of in de nabijheid van de voorspelde regio van negatieve  $\Gamma$ -waarden. Deze experimenten bevestigen de haalbaarheid van het originele idee. Bovendien ondersteunen deze metingen de validiteit van de NICFD theorie op verschillende manieren. In een expansie-experiment verandert bijvoorbeeld de geschatte geluidssnelheid vrij veel bij slechts kleine veranderingen in de thermodynamische toestand van het fluïdum, terwijl de veranderlijkheid van de golfvoortplantingssnelheid klein is, zoals te verwachten is voor stromingen van fluïdi met een thermodynamische toestand waarin  $\Gamma$  nabij 0 is. Hoewel enkele observaties in de resultaten van de experimenten het optreden van niet-klassieke fenomenen suggereren, zijn meer herhaalbare experimenten nodig om zekerheid te krijgen over het bestaan van de inversie van gasdynamische kenmerken in stromingen.

Recentelijk is nog een gebied met negatieve  $\Gamma$  geïdentificeerd in het tweefasen gebied nabij het damp-vloeistof kritische punt van alle samendrukbare substanties. Conventionele thermodynamische modellen, gebaseerd op toestandsvergelijkingen, falen in het voorspellen van thermodynamische grootheden in het damp-vloeistof kritische punt gebied, vooral voor afgeleide grootheden zoals  $\Gamma$ . Enkel modellen gebaseerd op zogenaamde schaalwetten zijn geldig en nauwkeurig in dit gebied. Een zo'n model is geïmplementeerd in de eigen software voor de schatting van thermodynamische eigenschappen, en is verbonden met een vloeistofmechanische solver om numeriek stromingen met thermodynamische staten in de nabijheid van het damp-vloeistof nauwkeurig te voorspellen. Simulaties van schokbuisstromingen zijn uitgevoerd om de haalbaarheid van het genereren van niet-klassieke NICFD fenomenen te bevestigen, en om het ontwerpen van experimenten gericht op het valideren van hun bestaan te helpen. Er is bijvoorbeeld een experiment in  $\text{CO}_2$  bedacht, waarin beide begintoestanden in de schokbuis zich in het éénfasegebied en op dezelfde isotherm bevinden. Dit maakt de realisatie van de thermodynamische condities en de test zelf een stuk eenvoudiger. Een andere wetenschappelijk interessante bevinding van deze studie dat het toelaatbaarheidsgebied van expansieschokgolven zich uitstrekt tot in het superkritische gebied, weliswaar marginaal, voor thermodynamische toestanden zeer dicht op het damp-vloeistof kritische punt.

Als laatste is een meer toegepast onderzoek uitgevoerd aan een systeem waarin NICFD kan

voorkomen. Het systeem is een organische Rankine cyclus (ORC) energiecentrale, waarvan de straalpijp van de turbine in het NICFD gebied functioneert. Om systeemdynamica en -beheersing te bestuderen, is een bibliotheek van volledig modulaire en herbruikbare modellen van componenten ontwikkeld, voor het uitvoeren van dynamische simulaties van zogenaamde geconcentreerde-elementen. Een casus van de transiënte prestatie van een 150 kW turbogenerator-systeem is beschouwd, welke volledig gemodelleerd en gesimuleerd is. De simulatieresultaten zijn gevalideerd met experimentele data uit twee bronnen. Een bron is afkomstig van een operationele energiecentrale, welke als ballastcyclus is uitgevoerd, waarbij het uitlaatgas van twee dieselmotoren de bron van thermische energie vormt. De andere databron is een experimentele campagne, welke is uitgevoerd met het doel om validatiedata te genereren, waarbij gebruik is gemaakt van een systeem op een testbank. Alle gesimuleerde thermodynamische variabelen komen overeen binnen 1 % van de gemeten waarden in stabiele toestand. Op 60 % van de originele belasting, vermindert de nauwkeurigheid van het model zich tot 3 % van de gemeten waarden in stabiele toestand. De hoofdkenmerken van de transiënte reactie van de centrale zijn correct voorspeld, maar in dit geval kan het verschil tussen de berekende en de gemeten waarde oplopen tot 25 %. Dynamische modellen van ORC systemen, die verkregen zijn door de componentmodellen te hergebruiken, kunnen dus in simulatiestudies gebruikt worden, met als doel het beheersen en transiënte gebruik van ORC energiecentrales. Zulke systemen kunnen gebruikt worden in bijvoorbeeld gebruik van restwarmte op vrachtwagens en in geconcentreerde zonne-energie.



# 1

## INTRODUCTION

### 1.1. NON-IDEAL COMPRESSIBLE FLUID DYNAMICS

Compressible fluid dynamics is a branch of fluid mechanics which describes the dynamics of fluids in the so-called compressible regime. The governing equations rely on an equation of state model for the fluid that relate the thermodynamic quantities used in the conservation equations, notably pressure  $P$ , density  $\rho$  and temperature  $T$ . For most applications in gasdynamics, the ideal gas law with constant specific heats suffices to close the system of equations. Van der Waals [1] added co-volume and intermolecular forces to the ideal gas law, which defined an equation of state capable of describing liquid and vapour states, after which he continued and discovered the principle of corresponding states [2]. The Van der Waals equation predicts that close to condensation and to the critical point in gases, significant deviation from the ideal gas law occurs. Non-ideal compressible fluid dynamics (NICFD) encompasses the field of fluid mechanics studying the motion of fluids in the dense-vapour, dense-vapour-liquid and supercritical thermodynamic region. Following Landau and Lifshitz [3] and Hayes [4], the fundamental derivative of gasdynamics  $\Gamma$  is defined as

$$\Gamma \equiv 1 + \frac{\rho}{c} \left( \frac{\partial c}{\partial \rho} \right)_s, \quad (1.1)$$

in which  $c$  is the speed of sound and  $s$  is the entropy. Thompson [5] refers to the thermodynamic property  $\Gamma$  as the fundamental derivative of gasdynamics for its importance in gasdynamics. For ideal gases,  $\Gamma$  is constant and equal to  $(\gamma + 1)/2$ , in which  $\gamma$  is the ratio of specific heats. Since  $\gamma$  is always greater than one,  $\Gamma$  is always greater than one. NICFD occurs whenever  $\Gamma$  is variable among the thermodynamic states of the considered fluid flow [6]. Such flows are characterized by, among other interesting phenomena, a quite different variation of the sound speed compared to that of ideal gases.

Bethe [7] developed the theory of shock waves for an arbitrary equation of state, while Zel'dovich [8] independently theorised that shock waves can be both of the compressive and expansive type, depending on the sign of  $\Gamma$ . In ideal gases, shock waves of the compressive type occur



in many instances, e.g. in the flow of air around supersonic aircraft and in supersonic turbines. Rarefaction shock waves (RSWs) violate the second law of thermodynamics in ideal gases by featuring a decrease in entropy through the shock wave, unlike compressive shock waves, which feature an entropy increase. Consequently, RSWs are not admissible in ideal gases. Thompson [5] realised that for negative values of  $\Gamma$ , the admissibility constraint reverses and only RSWs are admissible, while compressive shock waves can not occur. The branch of fluid dynamics dealing with flows featuring negative values of  $\Gamma$  is called non-classical gas dynamics. More recently, Zamfirescu *et al.* [9] discovered that the admissibility region for RSWs, the so-called rarefaction shock wave region (RSR) extends beyond the region of negative  $\Gamma$ .

Despite the theory being well established within the scientific community, there is no compelling experimental evidence of the existence of such an RSW. A first attempt to prove the existence of RSWs was carried out in the former USSR by Borisov *et al.* [10] and Kutateladze *et al.* [11], who claimed they had measured a RSW in Freon-13 (trifluorochloromethane,  $\text{CClF}_3$ ). Ferguson *et al.* [12], Cramer and Sen [13], Thompson [14] and Nannan *et al.* [15] confuted this finding and an alternative interpretation of that experiment was given by pointing towards critical point phenomena and two-phase effects. Recent studies by Nannan *et al.* [15] show that  $\Gamma$  is indeed negative in the vapour-liquid critical point region of any common pure fluid, and that RSWs are thus possible if a fluid is expanded from thermodynamic states in the vicinity of the critical point [16].

In the early 2000's, a shock tube experiment aimed at the detection and measurement of RSWs has been pursued at the University of Colorado at Boulder by Ferguson *et al.* [17]. The working fluid was PP10 (Perfluorofluorene,  $\text{C}_{13}\text{F}_{22}$ ), the proposed operating temperature 360 °C, and the pressure 15.5 bar, and a configuration with a diaphragm was adopted. The experiment failed because the working fluid underwent thermal decomposition due to the high operating temperature, and possibly to the lack of precautionary measures to avoid the presence of air and moisture within the fluid, which are known catalytic agents of thermal degradation [18, 19]. In addition, the repeatable rupture of the shock tube diaphragm proved critical due to the relatively small pressure difference and the large acoustic impedance of the fluid [20, 21]. Furthermore the duration of preparatory activities for the experiments was relatively long since the diaphragm had to be replaced after each test.

## 1.2. THEORY OF NON-IDEAL COMPRESSIBLE FLUID DYNAMICS

Among other interesting phenomena, NICFD flows feature a quite different dependence of the speed of sound on the temperature variation and on other flow variables. This different variation affects the propagation of waves. Since the effects of viscosity and thermal conductivity are limited to small regions within the flow, i.e. the boundary and shock layer, the Euler equations adequately describe the bulk flow in the NICFD regime, instead of reverting to the full Navier-Stokes equations. The Euler equations can be written as a function of only a single independent thermodynamic variable in case a homentropic flow is assumed. Although the flow is not always homentropic, this is a useful assumption, for reasons that will become clear in the following. The pressure is related to the density by introducing the

speed of sound as

$$c^2 = \left( \frac{\partial P}{\partial \rho} \right)_s, \quad (1.2)$$

Following Thompson [6] and choosing  $P$  as the independent variable, using this definition of the speed of sound, by combining the continuity and momentum equation, for 1-dimensional unsteady compressible flow, the conservation equation can be written as

$$\left[ \frac{\partial}{\partial t} + (u \pm c) \frac{\partial}{\partial x} \right] (u \pm F) = 0. \quad (1.3)$$

in which the thermodynamic function  $F$  is defined as

$$F = \int_{P_0}^P \frac{dP}{\rho c} = \int_{c_0}^c \frac{dc}{\Gamma - 1}. \quad (1.4)$$

Now these equations are first order quasi-linear hyperbolic partial differential equations, which can be solved, e.g., with the method of characteristics. In a 1-dimensional flow, waves propagate through the fluid with velocity  $u + c$ , or  $u - c$  for a wave running in positive or negative  $x$ -direction respectively. This shows that small disturbances, since a homentropic flow is assumed, propagate through the fluid with a velocity with respect to the local flow velocity that is equal to the speed of sound. In short,

$$w^\pm = u \pm c. \quad (1.5)$$

Characteristic curves are curves in a space-time ( $x-t$ ) diagram, whose slope equals the propagation speed  $w$  of an isentropic wave. For so-called simple waves, see Thompson [6], a quantity called the Riemann invariant is conserved along these characteristic curves, after Georg Friedrich Bernhard Riemann. The Riemann invariant is defined as

$$J^\pm = u \pm F, \quad (1.6)$$

From one characteristic curve to the next, the Riemann invariant can feature a different value. These results are valid for all fluids. In case the ideal gas assumption holds, the value of  $F$  equals  $(\gamma + 1)/2$ , which is always greater than one. Consequently, the value of  $F$  is integrable and the Riemann invariant can be written as

$$J^\pm = u \pm \frac{2}{\gamma - 1} c. \quad (1.7)$$

The derivative of the speed of sound can be inferred from equation (1.4) and reads

$$\frac{dc}{dP} = \frac{\Gamma - 1}{\rho c}. \quad (1.8)$$

Since both the density and speed of sound feature only positive values, the value of  $\Gamma$  determines the sign of the derivative of speed of sound with respect to pressure. For ideal gases, the value of  $\Gamma$  is greater than 1, such that with a the pressure increase, e.g. in a compression, the speed of sound increases. In a similar manner, the speed of sound decreases in rarefactions. In NICFD, the value of  $\Gamma$  can vary. For example, the value of  $\Gamma$  goes to infinity when

the critical point is approached from the supercritical region [15]. As a result, positive values of  $\Gamma$  are found in the single phase critical point region, much greater than the ideal gas value. Consequently in this thermodynamic region, variations in pressure induce a much stronger effect on the speed of sound. On the other hand, values of  $\Gamma$  below 1 are found in the dense gas region of fluids of sufficient molecular complexity. Consequently, in such cases, the speed of sound actually decreases in a compression, and increases in a rarefaction. When  $\Gamma$  has a constant value of 1, the speed of sound would remain unaffected with any pressure variation at constant entropy. The latter is a rather hypothetical case, since typically also the value of the thermodynamic quantity  $\Gamma$  is variable in the NICFD regime.

The wave propagation speed for pressure variations is different than the variation of the speed of sound. The reason for this difference is because a pressure variation not only results in variation of thermodynamic properties, such as the speed of sound, but also in the local flow velocity. Using equation 1.4 and after rewriting, as shown by Thompson [5, 6], the isentropic variation of wave speed is written as

$$\frac{dw}{dP} = \frac{d(c+u)}{dP} = \frac{\Gamma}{\rho c}. \quad (1.9)$$

For ideal gases,  $\Gamma$  is always positive, such that a pressure increase induces an increase in wave propagation speed. Whenever  $\Gamma$  takes a negative value, a pressure increase induces a decreasing wave propagation speed. Whenever this happens, the realm of nonclassical gas-dynamics is entered. It is possible to distinguish different regimes depending on the value of  $\Gamma$ , see figure 1.1. In a compression, if  $\Gamma > 1$ , the speed of sound increases, and so does the wave propagation speed. The flow of an ideal gas falls in this category. For  $0 < \Gamma < 1$ , a compression occurs with a decreasing sound speed, but still an increasing wave propagation speed. Only for  $\Gamma < 0$ , both speed of sound and wave propagation speed decrease. Two special cases are  $\Gamma = 1$ , in which the speed of sound remains unaltered with pressure variations and  $\Gamma = 0$ , in which the wave propagation speed remains unaltered with pressure variations.

The variation in wave propagation speed affects the formation of shock waves. In unsteady flows, initially smooth pressure variations change waveform as they propagate through the medium, because of the variation of the wave propagation speed. Using the example of the positive pressure variation, as the right-running wave propagates in a one-dimensional tube, the part of the wave at a higher pressure travels faster than the lower pressure portion. Consequently, the wave steepens, until a pressure discontinuity, i.e. a shock wave, forms, see figure 1.2. In this example, the flow is classical and a compression shock wave is formed. In the nonclassical case, the wave propagation speed decreases with pressure, and the faster travelling rear-side of the wave takes over the high-pressure part of the wave, and an RSW is formed, see figure 1.3. For the case in which  $\Gamma = 0$ , the wave propagates completely unaltered and no shockwave is formed.  $\Gamma$  can be written in a convenient way as a function of specific volume, speed of sound and pressure as

$$\Gamma \equiv \frac{v^3}{2c^2} \left( \frac{\partial^2 P}{\partial v^2} \right)_s. \quad (1.10)$$

In this way, it becomes apparent that in the thermodynamic  $P$ - $v$ -diagram of a fluid, the curvature of the isentrope reveals the sign of  $\Gamma$ , since specific volume and speed of sound can

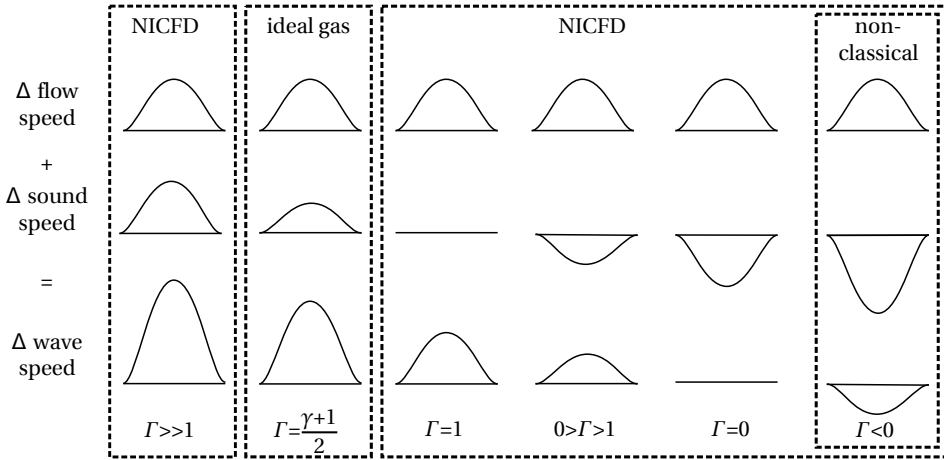


Figure 1.1: Schematic variation of the flow speed, speed of sound and wave propagation speed as a function of a triangular pressure increase for different values of  $\Gamma$ . The variation in flow speed is independent of the value of  $\Gamma$ , but the speed of sound is not. The change in wave propagation speed is the sum of the variation in flow speed and variation in speed of sound.

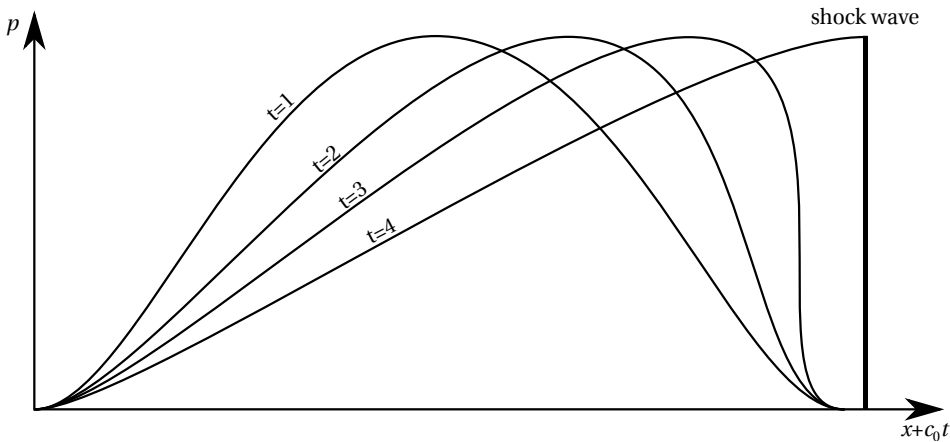


Figure 1.2: A schematic example of wave steepening of an initial symmetric smooth pressure disturbance traveling in the right direction in the classical regime. The waveform of the disturbance changes as it propagates, and steepens on the compressive side, while it dilates on the rarefaction side. At  $t = 3$ , part of the compression exhibits a vertical pressure profile, which is the moment a shock wave starts. At  $t = 4$ , a fully formed shock is displayed.

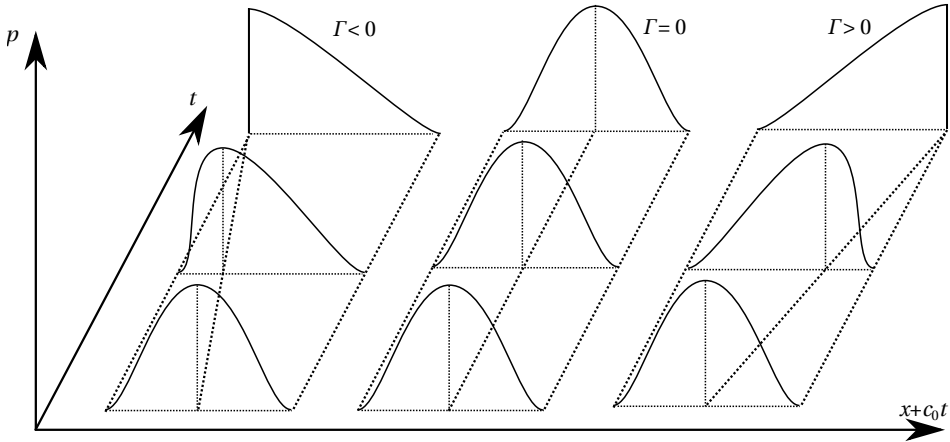


Figure 1.3: Wave propagation for the classical and nonclassical regime. In the classical regime with  $\Gamma > 0$ , a compression shockwave is formed. For the case with  $\Gamma = 0$ , the wave propagates unaltered. For the nonclassical case with  $\Gamma > 0$ , a rarefaction shockwave is formed.

only attain positive values. Two zones of negative  $\Gamma$  have been predicted to occur in simple compressible substances, based on thermodynamics. The so-called BZT region, named after scientists Bethe, Zel'dovich and Thompson, is a region of negative  $\Gamma$  that is predicted to occur in fluids formed by sufficiently complex molecules [22]. It is located in the single-phase vapour region close to the dew line, see figure 1.4. By definition, isotherms are horizontal at the vapour-liquid critical point, and consequently feature a concave section in the vapour region. Isentropes of molecularly complex fluids, due to their large heat capacity, approach their isotherms, and are also predicted to feature a concave section in this region. The other region, recently discovered by Nannan *et al.* [15], is a negative  $\Gamma$  region predicted for thermodynamic states in the vapour-liquid phase in the vicinity of the critical point in any fluid. Due to the increased heat capacity in the proximity of the critical point, isentropes are close to horizontal in this region. In the supercritical regime, isentropes feature very convex curvatures in the  $P$ - $v$ -diagram, and consequently very high values of  $\Gamma$ , going to infinity at the critical point. In the two-phase region, the curvature is concave, and feature negative values of  $\Gamma$ , going to minus infinity when the critical point is approached from this side. This region of negative  $\Gamma$  also gives rise to the possibility of nonclassical gasdynamic phenomena, such as RSWs [16].

Shock waves exhibit an entropy increase, and the assumption of homentropic flow is not valid anymore. Consequently also their propagation speed is different. In particular, it is higher than the speed of sound. The discontinuous change in thermodynamic and flow properties are described by the jump equations, theorised independently by Rankine [23] and Hugoniot [24]. These equations are derived by applying the mass, momentum and energy conservation equations to a control volume that encloses the shock and moves at the same velocity as the shock. Under the assumption that the fluid is in thermodynamic equilibrium on both sides of the shock, and the shock layer is of negligible thickness, the conser-

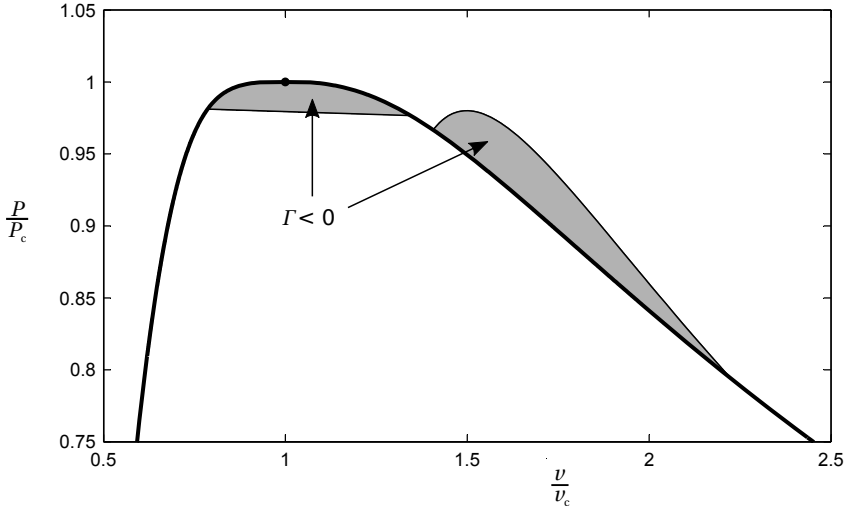


Figure 1.4: Pressure - volume diagram of a BZT fluid, with the regions of negative  $\Gamma$  displayed. There are two regions featuring a negative value of  $\Gamma$ . One zone is in the two-phase regime, just below the critical point. The other zone is the BZT zone in the vapour region, which is only exhibited by molecularly complex fluids.

vation equations are

$$\rho_A w_A = \rho_B w_B, \quad (1.11)$$

$$P_A + \rho_A w_A^2 = P_B + \rho_B w_B^2, \quad (1.12)$$

$$h_A + \frac{w_A^2}{2} = h_B + \frac{w_B^2}{2}, \quad (1.13)$$

in which  $h$  is defined as the enthalpy, and subscript A and B denote the pre-shock and post-shock state respectively. When equation 1.11 and 1.12 are combined one can obtain

$$J^2 = (\rho_A w_A)^2 = (\rho_B w_B)^2 = -\frac{P_B - P_A}{v_B - v_A}, \quad (1.14)$$

with  $J$  defined as the mass flux. In a  $P$ - $v$  plane, it describes a straight line, called the Rayleigh line. Equation 1.13 can be manipulated symbolically in order to obtain

$$h_B - h_A = \frac{1}{2} (P_B - P_A) (v_B + v_A). \quad (1.15)$$

This equation is convenient because it is independent of the reference frame and contains only thermodynamic variables. The curve that is described implicitly by this thermodynamic condition is called the shock adiabat. It describes the possible post-shock thermodynamic conditions from certain given thermodynamic initial conditions. Neither the Hugoniot line, also referred to as adiabat, nor the Rayleigh line indicate whether the shock is of the compression or rarefaction type. This is determined by two other criteria: the entropy and mechanical condition. Since the Rayleigh and Hugoniot line are not analogous to isentropes, a change in entropy level is apparent. The second law of thermodynamics prescribes

that entropy can only increase. This leaves only the possibility for either a compressive shock wave, or an RSW. This also implies that in a shock wave, entropy is produced, and consequently it is an irreversible process. The second criterion is the mechanical criterion. The works from Lax [25] and Oleinik [26] show that the pre-shock Mach number must be greater or equal than one, and the post-shock Mach number must be smaller or equal to one, so  $M_A \geq 1 \geq M_B$ . This condition can be written in terms of thermodynamic variables  $P$  and  $v$  as

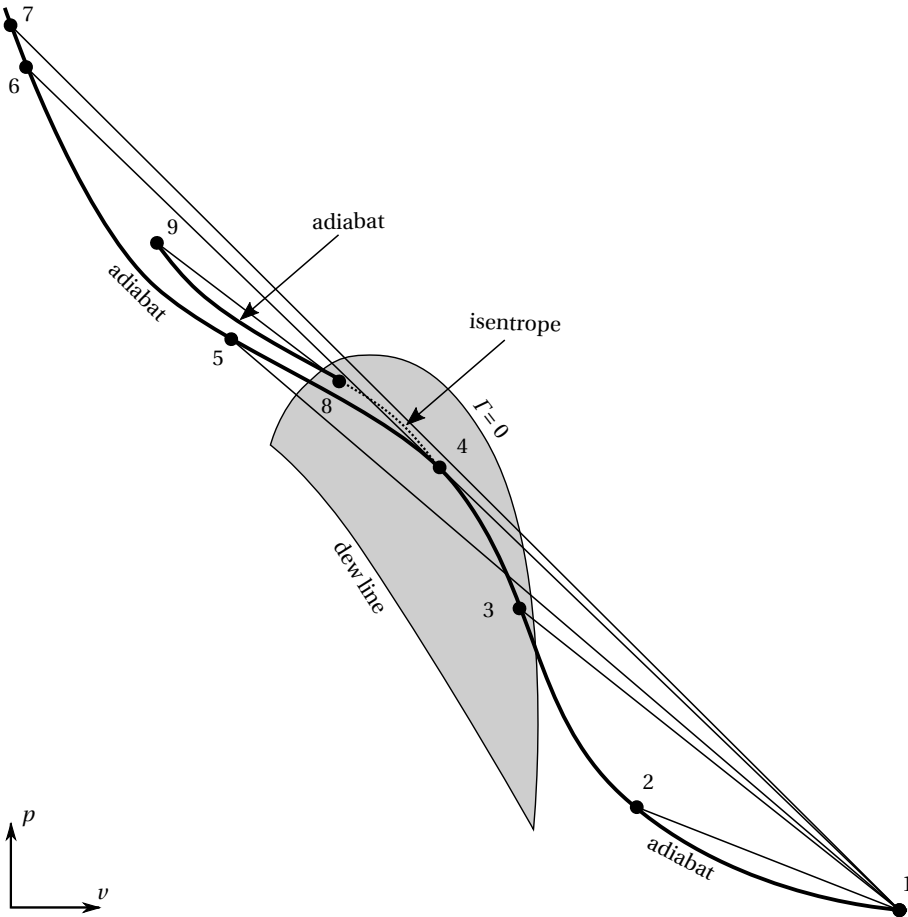
$$\left(\frac{\partial P}{\partial v}\right)_{HR_{A,B}} \leq \frac{[P]}{[v]} \leq \left(\frac{\partial P}{\partial v}\right)_{HR_{A,A}} \quad (1.16)$$

### 1.3. COMPRESSIONS IN THE NONCLASSICAL REGIME

Within a region of positive  $\Gamma$ , an isentropic compression in an unsteady simple flow steepens and can form a shock wave, while an expansion dilates and forms a rarefaction fan. Within a region of negative  $\Gamma$ , an isentropic expansion in an unsteady simple flow steepens and can form a RSW, while a compression dilates and forms a compression fan. Zamfirescu *et al.* [9] show that in case the thermodynamic region features regions of both a positive and a negative value of  $\Gamma$ , it is possible for both compression shocks and RSWs to occur. Moreover, they show that it is also possible for compression shocks to occur in the negative  $\Gamma$  region, and that the admissibility region for RSWs extends beyond the region of negative  $\Gamma$ .

It is often convenient to determine the admissibility of shock waves in a graphical manner. In a  $P$ - $v$ -diagram, the Hugoniot line and Rayleigh line are drawn. The mechanical admissibility condition implies that the Rayleigh line does not intersect the Hugoniot line from the initial state. Consequently, the Rayleigh line must lie completely above the Hugoniot line for compression shock waves and completely below the Rayleigh line for expansion shock waves. An example for a compression is given in figure 1.5, with a schematic size of the BZT region. The initial state is at point 1, which is chosen to be an arbitrary point in the positive- $\Gamma$  region, at a lower pressure, but within short distance of those pertaining to states in the BZT region.

Starting from point 1 in figure 1.5, a compression to point 2 encompasses states that are fully within the positive  $\Gamma$  domain. The Hugoniot line is therefore convex and the Rayleigh line is completely above the Hugoniot line. This compression shock is admissible. Point 3 lies within the negative  $\Gamma$  domain. A compression shock from point 1 to point 3 is however still admissible, since the Rayleigh line still lies completely above the Hugoniot line. The compression to point 4 is still admissible, but the Rayleigh line is tangent to the Hugoniot line in point 4. Consequently the post shock state features a sonic speed [9], and the entropy is at a local maximum [27]. A wave with these characteristics is called a post-sonic shock wave. A shock wave to point 5 is inadmissible. The Rayleigh line crosses the Hugoniot line, violating the mechanical stability criterion. All solutions to the system of equations 1.14 and 1.15, on the same Hugoniot line from point 4 to point 6 are inadmissible for this reason. Starting from point 6 and at higher pressures on the same Hugoniot line, show post-shock states that provide admissible solutions. The shock from point 1 to point 6 is a composite wave, formed by a post-sonic shock from 1 to 4 and a pre-sonic shock from point 4 to 6. The latter is pre-sonic because the Rayleigh line is tangent to the Hugoniot line in the pre-shock



| start | end | type   |
|-------|-----|--|
| 1     | 2   | classical shockwave  |
| 1     | 3   | classical shockwave  |
| 1     | 4   | post-sonic shockwave   |
| 1     | 5   | inadmissible   |
| 1     | 6   | post-sonic shockwave + pre-sonic shockwave                   |
| 1     | 7   | classical shockwave  |
| 1     | 8   | post-sonic shockwave + compression fan                       |
| 1     | 9   | post-sonic shockwave + compression fan + pre-sonic shockwave |

Figure 1.5: Compression possibilities with an initial state outside the BZT zone.



state at point 4. For post-shock states at higher pressures, e.g. point 7, a single shock wave can be formed, which is neither pre-sonic nor post-sonic, but passes through the negative  $\Gamma$  region. For post-shock pressures below point 6, e.g. point 9, the result is a composite wave. In this case, a post-sonic shock forms from point 1 to 4, followed by a nonclassical compression fan from point 4 to point 8, after which a pre-sonic shock follows from point 8 to point 9.

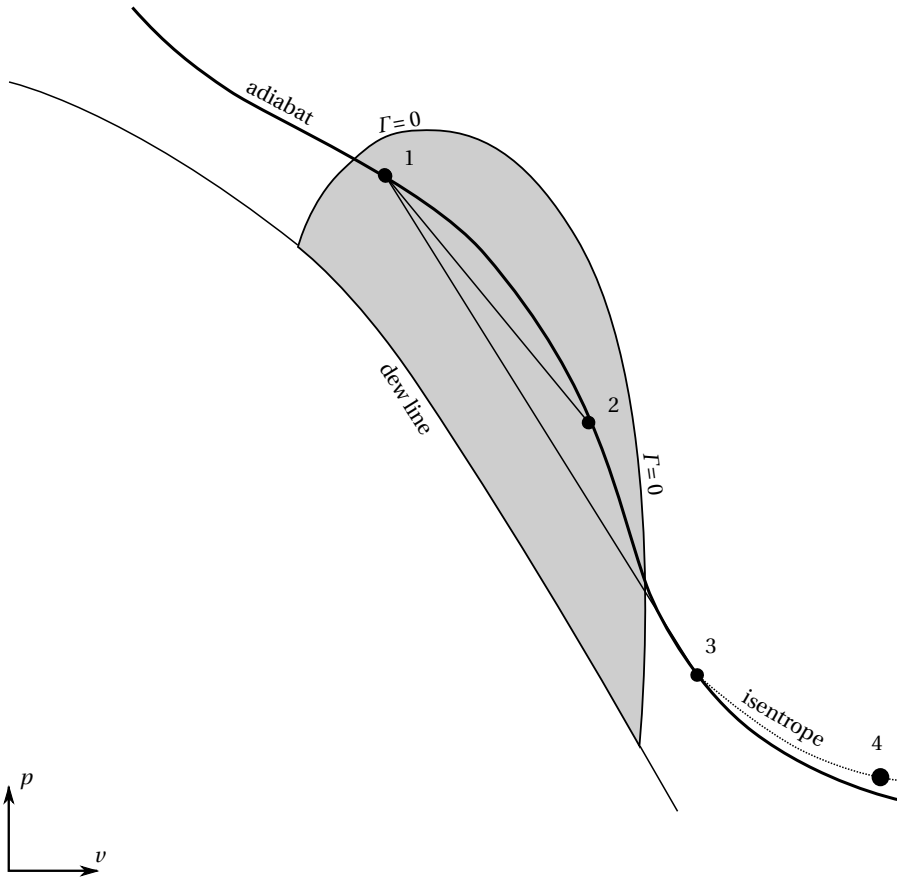
#### 1.4. EXPANSIONS IN THE NONCLASSICAL REGIME

The treatment of rarefaction shock waves is similar to that of compression shock waves, treated in section 1.3. It can be summarized in three steps: first the possibilities for RSWs starting in the negative  $\Gamma$  region are described, then RSWs starting in the positive  $\Gamma$  region, but within the double-sonic locus, are presented. Finally possibilities for RSWs to occur with a starting point outside the double-sonic locus are discussed.

Figure 1.6 shows the  $P$ - $v$ -diagram with an adiabat drawn from the starting point at a thermodynamic state within the negative  $\Gamma$  region. If the post-shock state is also within the negative  $\Gamma$  region, e.g. point 2, the adiabat is fully concave. Consequently the Rayleigh line is always below the Hugoniot line, thus the RSW is admissible. In case the post-shock state is outside the negative  $\Gamma$  region, the RSW is still admissible, as long as the Rayleigh line does not cross the Hugoniot line, which is up to point 3. At point 3, the Rayleigh line is tangent to the adiabat. A shock wave connecting such post-shock state would have a sonic post-shock flow. Any further rarefaction, e.g. to point 4, would occur isentropically from point 3 and creates a rarefaction fan.

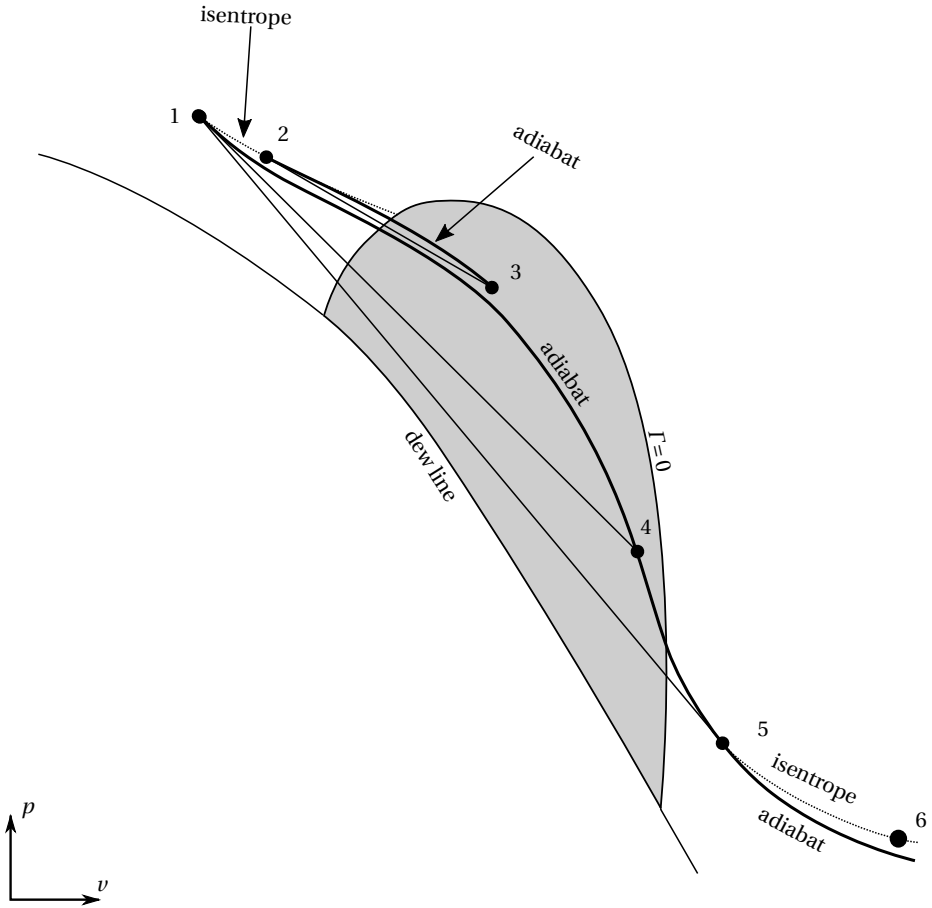
If the initial state lies at a higher pressure than the states within the negative  $\Gamma$  region, but in its close vicinity, it may be possible for RSWs to occur. An example is displayed in figure 1.7 with initial state 1. In case the post-shock state is point 2, the rarefaction encompasses solely states in the positive  $\Gamma$  region. Consequently, only compression shock waves are admissible, and an initial rarefaction profile dilates and follows the isentrope. In case the flow expands into the negative  $\Gamma$  domain, e.g. to point 3, part of the rarefaction can form a RSW. The initial part of the rarefaction still takes place isentropically, until the isentrope is tangent to the adiabat through the post-shock state, which is at point 2. This is the starting point for an RSW, which has a sonic pre-shock state. The Rayleigh line is not tangent to the Hugoniot line at the post-shock state, such that the post-shock Mach number is not equal to unity. For a post-shock state with a lower pressure in the negative  $\Gamma$  domain, the Rayleigh line becomes steeper. This results in the initial pre-sonic shock state to occur at a higher pressure. For the expansion from point 1 to point 4, the pre-sonic shock state occurs immediately at point 1. Expansions with post-shock state between point 4 to point 5 can occur entirely through a shock that has neither a pre-sonic nor a post-sonic shock state. With point 5 as post-shock state, the Rayleigh line is tangent to the adiabat at point 5, and the post-shock state is sonic, which is the limiting case. Expansions with a final state featuring a lower pressure than the pressure of point 5, e.g. an expansion to point 6, take place with a post-sonic shock to point 5 followed by an isentropic expansion fan.

Now consider the situation when the initial thermodynamic state lies far from the BZT re-



| start | end | type                             |
|-------|-----|----------------------------------|
| 1     | 2   | RSW                              |
| 1     | 3   | post-sonic RSW                   |
| 1     | 4   | post-sonic RSW + rarefaction fan |

Figure 1.6: RSW possibilities with the initial state in the BZT zone.



| start | end | type                             |
|-------|-----|----------------------------------|
| 1     | 2   | rarefaction fan                  |
| 1     | 3   | rarefaction fan + pre-sonic RSW  |
| 1     | 4   | pre-sonic RSW                    |
| 1     | 5   | post-sonic RSW                   |
| 1     | 6   | post-sonic RSW + rarefaction fan |

Figure 1.7: Shock wave possibilities with an initial state outside the BZT zone, but within the admissibility domain of RSWs. Because it is within the double-sonic locus, the Hugoniot line from the initial state passes through the BZT zone.

gion, e.g. point 1 in figure 1.8. Expansions not going through the negative  $\Gamma$  region follow the isentrope and dilate in a rarefaction fan. Only in case part of the expansion takes place in the negative  $\Gamma$  region, e.g. an expansion from point 1 to point 4, an RSW can be formed, which develops a pre-sonic RSW starting at point 3, with the thermodynamic starting point when the Rayleigh line is tangent to the isentrope. Expansions from the same initial conditions to even lower post-shock pressures result in an RSW with a higher pre-shock pressure. Consequently, a smaller part of the expansion takes place isentropically. The limit for the RSW is reached when the expansion is down to point 5, when the post-shock speed equals the sonic speed. Both pre-shock and post-shock state have sonic conditions and this shock is called a double-sonic shock wave. For rarefactions to a lower pressure than point 5, e.g. to point 6, the initial isentropic rarefaction fan is followed by a double-sonic shock and continues as an isentropic rarefaction fan. Such a flow is shown schematically in figure 1.9. The double-sonic RSW is the maximum pressure difference RSW that can occur [28] on the adiabat under consideration. The double-sonic locus is obtained by connecting the pre-shock and post-shock states of all possible double-sonic shocks. This gives the admissibility domain of RSWs or the rarefaction shock wave region (RSR) [9]. More details can be found in the work of Kluwick [27].

## 1.5. NICFD FLOWS IN SHOCK TUBES

Shock tubes are arguably the experimental device of choice for the study of NICFD, as they have been already successfully used for measurements of shocks and unsteady wave propagation in fluids. Examples include shock tubes for the study of non-equilibrium vapour condensation [29], droplet condensation in expansion tubes [30] and studies of particle-dense flow fields [31].

Wave propagation can be studied in shock tubes by separating a tube into two compartments, and bringing each part in the desired thermodynamic conditions. By suddenly connecting the two compartments, waves propagate into each compartment. The removal of the physical boundary between the two compartments typically needs to be executed in an almost instantaneous manner in order to be able to observe desired phenomena. This is often done by breaking a diaphragm or opening a fast-acting valve. The propagation of isentropic waves through the shock tube provides information on the value of  $\Gamma$ , see equation 1.9. A schematic example of the local isentropic wave propagation speed as a function of the pressure drop of a classical rarefaction is given in figure 1.10, for both an ideal gas case and a NICFD case. The slope of the wave speed provides information on the sign of  $\Gamma$ .  $\Gamma$  is greater than zero for both cases in this example, because the wave propagation speed decreases with decreasing pressure. Note that the horizontal axis displays a negative pressure difference. For the ideal gas case, the slope varies only as a result of the varying density and speed of sound, as  $\Gamma$  is constant. For the NICFD case, the value of  $\Gamma$  varies as well, which can result in both a steeper slope and a less steep slope if compared to the ideal gas case.  $\Gamma$  remains positive, since the wave propagation speed monotonously decreases in the rarefaction. A qualitative estimation of the sign of  $\Gamma$  can thus be made, but the value of the density and speed of sound are required, if one wants to obtain a quantitative estimate of  $\Gamma$ . It is also possible to encounter processes in which the isentropic wave propagation speed increases. Examples are a classical compression in an ideal gas, and a nonclassical rarefaction, when  $\Gamma$

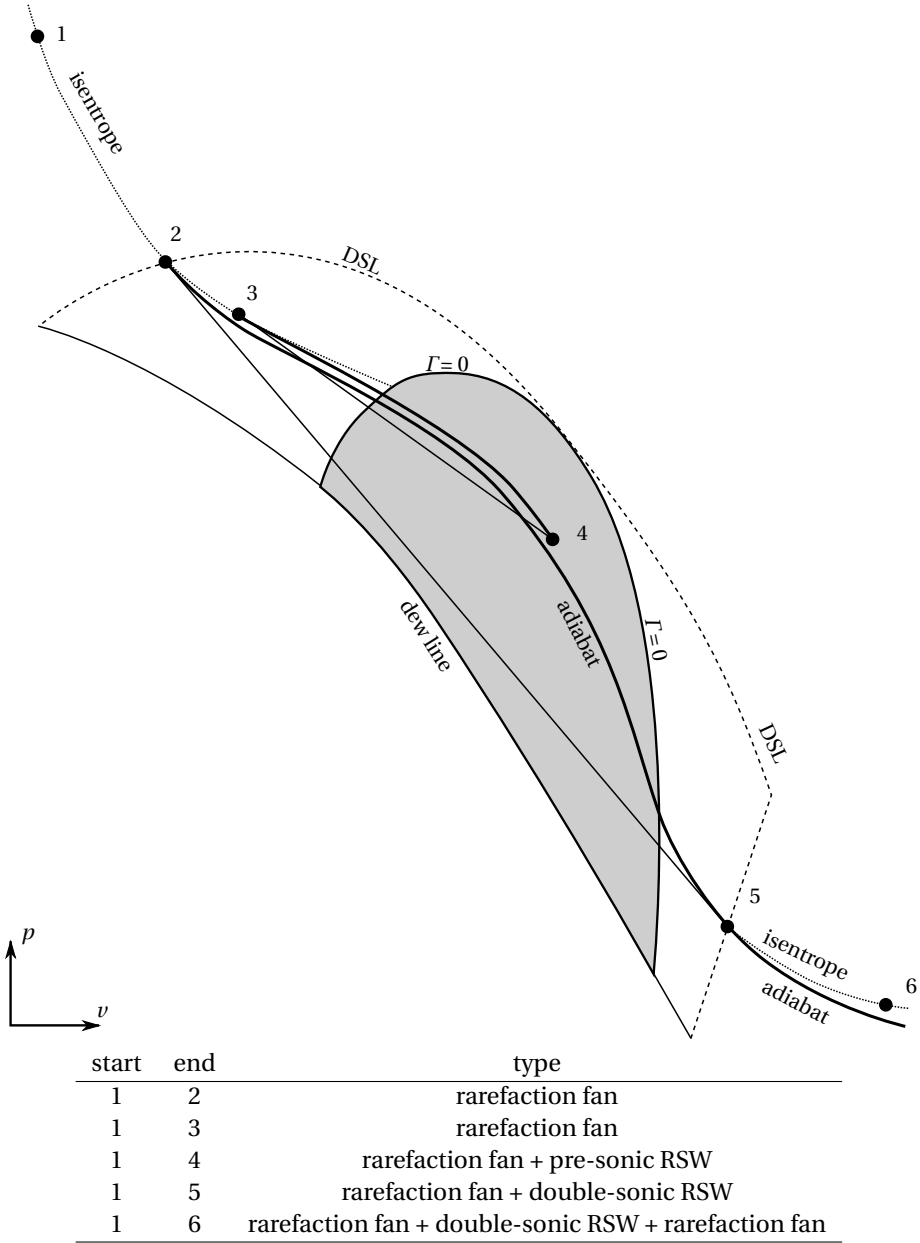


Figure 1.8: Shock wave possibilities with an initial state outside the double-sonic locus with a Hugoniot line that passes through the BZT region. The first part of the expansion will always be in the form of a rarefaction fan, and a formed RSW will always have pre-sonic conditions, and optionally post-sonic conditions.

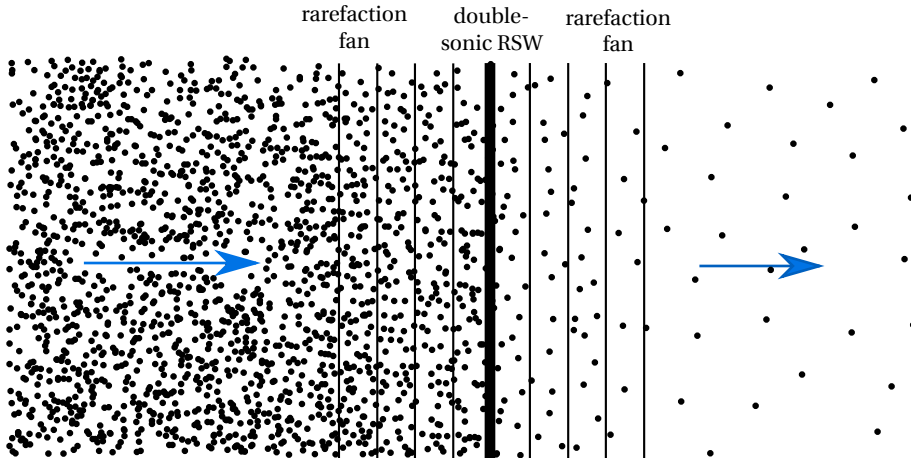


Figure 1.9: Schematic representation of a continuous expansion consisting of a rarefaction fan, a double-sonic RSW, and another rarefaction fan in the reference frame of the double-sonic RSW. The rarefaction fans dilate, such that isentropic rarefaction waves move away from the double-sonic RSW. The blue arrow indicates the fluid velocity. Dots are used to schematically indicate the fluid density.

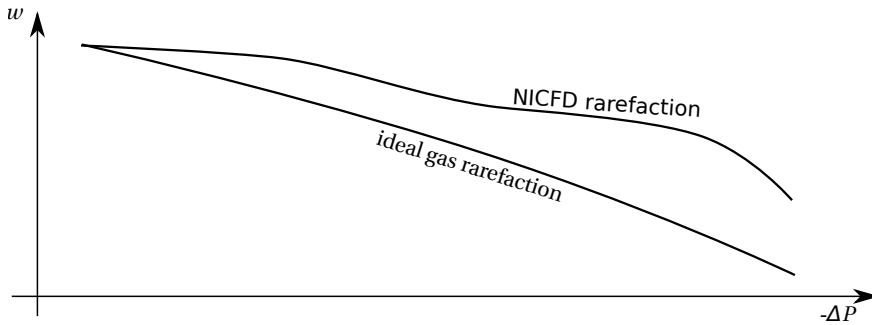


Figure 1.10: Schematic diagram of wave propagation speed vs. pressure drop of a rarefaction in an ideal gas and in a NICFD case. Note that the horizontal axis displays a negative pressure difference in this image. In an ideal gas, the slope of the wave propagation speed changes due to variation in the density and speed of sound. For the NICFD case, the value of  $\Gamma$  is an additional parameter. Since the wave propagation speed is monotonously decreasing, the value of  $\Gamma$  is always positive in these examples.

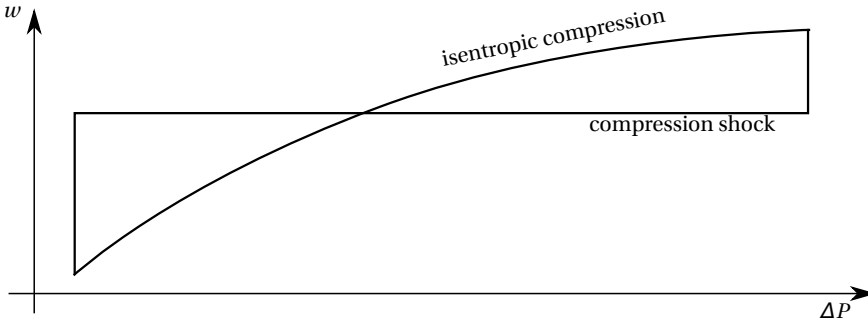


Figure 1.11: Schematic diagram of wave propagation speed vs. pressure difference of a compression in an ideal gas. Note that the horizontal axis displays a positive pressure difference in this image. In the isentropic example the wave propagation speed is higher at higher values of the pressure, which can lead to formation of shock waves. A shock wave displays a pressure discontinuity that moves at constant speed, which shows up as a horizontal line in this diagram.

is smaller than zero. A schematic example of a classical compression in an ideal gas is displayed in figure 1.11. Since the pressure difference is positive in a compression, and  $\Gamma$  is also positive for an ideal gas, the isentropic local wave propagation speed increases. Note that the horizontal axis now displays a positive pressure difference. An increasing wave propagation speed can lead to the formation of a shock. The pressure increase then takes place discontinuously, and the shock propagation speed is constant, resulting in a horizontal line in the diagram. Shock formation typically takes place at a certain distance upstream from the location of the diaphragm or valve [32], because the rupture of the diaphragm or the opening of a valve requires a finite time. It occurs when characteristic curves merge, as described in section 1.2. The diaphragm breaking mechanism or valve opening sequence itself also influences the formation and strength of a shock wave [33]. In addition, the value of  $\Gamma$  also influences the formation process, since it is related to the variation in wave propagation speed. For shocks, the entropy is no longer constant, but is third-order dependent on the shock strength [6], and can be estimated by

$$[s] = \frac{1}{T_1} \left( \frac{\partial^2 v}{\partial R^2} \right)_s [P]^3 + O([P]^4), \quad (1.17)$$

in which the subscript 1 denotes the pre-shock state. Information on the pre-shock value of  $\Gamma$  can be extracted, following Thompson [6], by using the definition of  $\Gamma$  from equation 1.10 and rewriting this equation as

$$\frac{T_1 [s]}{c_1^2} = \frac{1}{6} \Gamma_1 \Pi^3 + O(\Pi^4), \quad (1.18)$$

in which  $\Pi = [P] / \rho_1 c_1^2$ . In the nonclassical case, the fluid in parts of the shock tube is in a thermodynamic state featuring negative values of  $\Gamma$ . This is exhibited in a variety of ways. In case a compression takes place in the fluid, the wave propagation speed decreases for thermodynamic states at a higher pressure than the initial state, resulting in a dilating compression fan. In case a rarefaction is considered, either shock formation has taken place,

which results in the presence of RSWs in the flow, or shock formation has not taken place yet. In the latter case, the wave propagation speed increases for thermodynamic states at a lower pressure than that of the initial state.

## 1.6. APPLICATIONS

Despite the lack of experimental information regarding fluid flows occurring in the NICFD regime, these type of flows are encountered in a variety of industrial processes. Notable examples are flows, occurring within turbomachinery of novel technologies for the conversion of renewable energy sources, like Organic Rankine Cycle (ORC) power systems [34–36], whereby the working fluid is an organic compound, e.g. a hydrocarbon or siloxane. If the power output is low and/or the temperature of the energy source is moderate or low, the use of an organic substance as working fluid allows to obtain high efficiency and other advantages if compared to conventional steam power plants. The reason is that the volume flow through the ORC expander is higher, due to the large heat capacity of the fluid. Consequently, the speed of sound in such fluids is low, and the Mach number through the nozzle expander high, often highly supersonic. Supersonic flows can induce shock waves, propagating through the channels of the machine, impinging on its surfaces, and causing boundary layer detachment. Such flow fields result in comparatively low isentropic efficiency of the expander, and can cause mechanical failure. Moreover, NICFD flows in nozzles of supersonic turbines are significantly different than flows of ideal-gases [37], which impacts the optimal shape of such components [38, 39]. NICFD effects in components of ORC power plants are currently not considered in the working fluid selection, which is done on system level [40]. A better understanding of NICFD flows together with experimental information on the sound propagation in conditions that are typical of high-temperature ORC turbines helps improving the design of this unconventional turbomachinery, both in terms of efficiency and of reliability.

Heat pumps feature a thermodynamic cycle in which the compression takes place in the vapour phase close to the dew line, and consequently the flow can occur in the NICFD regime. Especially the design of high temperature heat pump compressors can benefit from the knowledge of NICFD as shocks can be significantly reduced in strength or avoided altogether [41].

The compressor of supercritical carbon dioxide (scCO<sub>2</sub>) power systems operates close to the critical point [42], where  $\Gamma$  is known to be highly variable. Recent research using computational fluid dynamic simulations has shown that expansions in the two-phase regime, close to the vapour-liquid critical point, are possible to occur [43] and can display nonclassical effects, such as RSWs. These are all examples of applications and of scientific research to which the work documented here contributes additional knowledge.



## 1.7. MOTIVATION FOR THE STUDY

Measurements in dense vapours of high molecular weight fluids are scarce [44, 45]. Flow measurements in the dense vapour region of complex organic fluids can contribute to the improvement of thermodynamic models and to the understanding of NICFD. Experimental evidence of nonclassical gasdynamic phenomena in the single-phase vapour region is still lacking.

Currently, a number of research efforts in the field of non-ideal compressible fluid dynamics are being performed, and cover the range from fundamental to applied studies. At Politecnico di Milano a supersonic vapour wind tunnel is under development for the study of dense gas flows. First results related to flows of siloxane MDM have been documented by Spinelli *et al.* [46], though the setup can operate with different fluids. Future efforts will focus on the flow of mixtures of dense gas compounds. A small experimental ORC power system is being commissioned at Lappeenranta University of Technology. Contrary to many experimental low power ORC systems employing volumetric expanders [47], this 10 kW system adopts a high-speed turbine in a hermetically sealed system in which the working fluid is also used as a lubricant. Another experimental facility, named ORC hybrid Integrated Device (ORCHID), is being commissioned at Delft University of Technology [48]. The system implements a high-temperature regenerated ORC, and it can feed with dense vapour either a supersonic nozzle for fundamental research or an experimental 10 kW ORC turbine. This allows the study of both fundamental flow fields, as well as ORC turbines.

The objective of the research documented in this PhD thesis is the commissioning of a facility for studying NICFD flows, and experiments on such flows, aimed at the generation and measurement of particular nonclassical gasdynamic phenomena such as RSWs. Measurements of an RSW would provide the experimental validation of NICFD theory. Flow measurements in the dense vapour region of complex organic fluids contribute to the improvement of thermodynamic models and to the understanding of NICFD.

## 1.8. OUTLINE OF THE THESIS

The thesis is structured as follows. Chapter 2 describes the commissioning of the Flexible Asymmetric Shock Tube (FAST). It is a Ludwieg tube type setup designed to study the NICFD flows in dense vapours of organic fluids. This chapter also shows results from preliminary wave speed measurements in ideal incondensable gases and in the vapour of dodecamethylcyclohexasiloxane ( $D_6$ ) at values of  $\Gamma$  predicted to be between 0.8 and 0.9. Chapter 3 presents the results and analysis of wave speed measurements in  $D_6$ , in which the thermodynamic conditions feature a value  $\Gamma$  predicted to be below 0. Some possibilities for experiments in the two-phase vapour-liquid critical point region are discussed in chapter 4. The study is conducted by means of computational fluid dynamic simulations of shock tube flows. The last chapter of the thesis is devoted to a study on the unsteady operation of a 150 kW ORC power plant by means of simulations using a lumped-parameter dynamic system model. The conclusions and an outlook into the future of NICFD is given in chapter 6.

# 2

## FLEXIBLE ASYMMETRIC SHOCK TUBE: A FACILITY FOR WAVE PROPAGATION SPEED MEASUREMENTS IN DENSE GASES

Selected contents from:

Mathijssen, T., Gallo, M., Casati, E., Nannan, N., Zamfirescu, C., Guardone, A., Colonna, P., The flexible asymmetric shock tube: A Ludwig tube facility for wave propagation measurements in high-temperature vapours of organic fluids. *Exp. Fluids* 56:10, October (2015), 11 pages.

### 2.1. INTRODUCTION

This chapter documents the Flexible Asymmetric Shock Tube (FAST) set-up and the first experimental results of wave propagation measurements in the dense vapour of  $D_6$ . The FAST is an unconventional Ludwig tube designed and installed at Delft University of Technology [49], in the Netherlands, with the aim of studying wave propagation in the dense vapour of organic compounds, and in particular of providing the first experimental proof of the existence of nonclassical gasdynamic phenomena. Figure 2.1 shows a schematic overview of a rarefaction wave experiment and figure 2.2 of the facility. The charge tube (CT) is filled with the dense organic vapour and kept at the desired pressure and temperature. The fast-opening valve (FOV), initially closed, is opened, thus allowing the fluid to flow towards the low pressure plenum (LPP), which is maintained at a lower pressure. Consequently a rarefaction travels into the CT. If the thermodynamic state of the fluid is within the rarefaction shock region [9], the rarefaction steepens and forms a nonclassical RSW or mixed wave field. Outside the rarefaction shock region, a classical rarefaction fan forms.

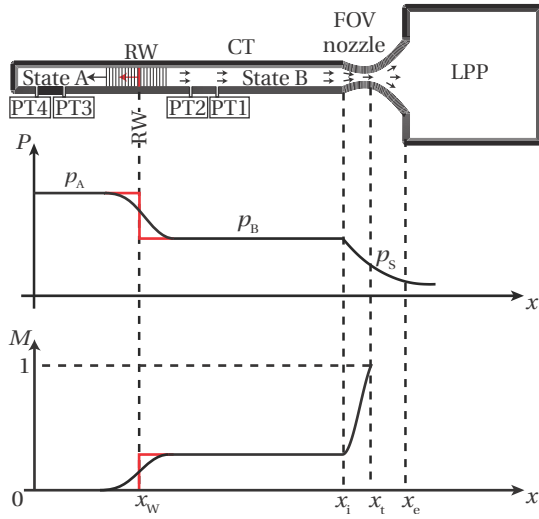


Figure 2.1: Schematic overview of a rarefaction wave experiment. The upper charts shows the qualitative pressure profile after the opening of the FOV separating the charge tube (CT) from the reservoir (LPP). The lower chart shows that a rarefaction propagates into the charge tube at sonic speed  $W$  for a classical rarefaction fan (in black) or at supersonic speed for a RSW (in red). The fluid is accelerated from rest condition A to condition B and flows into the reservoir through the nozzle. At the nozzle throat, sonic conditions S are attained. The pressure is captured by pressure transducers PT1 to PT4.

A description of the set-up is provided in section 2.2: it provides details about the components equipping the complete system as-built, about the procedure of an experiment, and an overview of the control and data acquisition system. The results of the characterization of the setup, demonstrating the correct operation of the facility and validating the measurement systems are reported and discussed in section 2.3. In section 2.4 results from preliminary rarefaction wave measurements in  $D_6$  are reported. Section 2.5 summarizes concluding remarks and outlines future work.

## 2.2. THE FAST AND THE EXPERIMENTAL PROCEDURE

The mechanical and heating equipment is described in section 2.2.1 by outlining the procedure of a typical experiment. The measurement and monitoring instruments as well as the control system are briefly reported in section 2.2.2.

### 2.2.1. EQUIPMENT & PROCEDURE

A schematic representation of the FAST is reported in figure 2.2. All pipes, vessels, and parts in contact with the working fluid are made of stainless steel (316Ti). Before starting an experiment, the working fluid undergoes a purification process to remove air and moisture as much as possible, which are known to promote decomposition at high temperature. The fluid is passed through a  $3\text{\AA}$  molecular sieve and a filter to remove any residual solid particle, before it flows into a stainless steel Swagelok cylinder (type 304L-HDF-81CAL). The cylinder

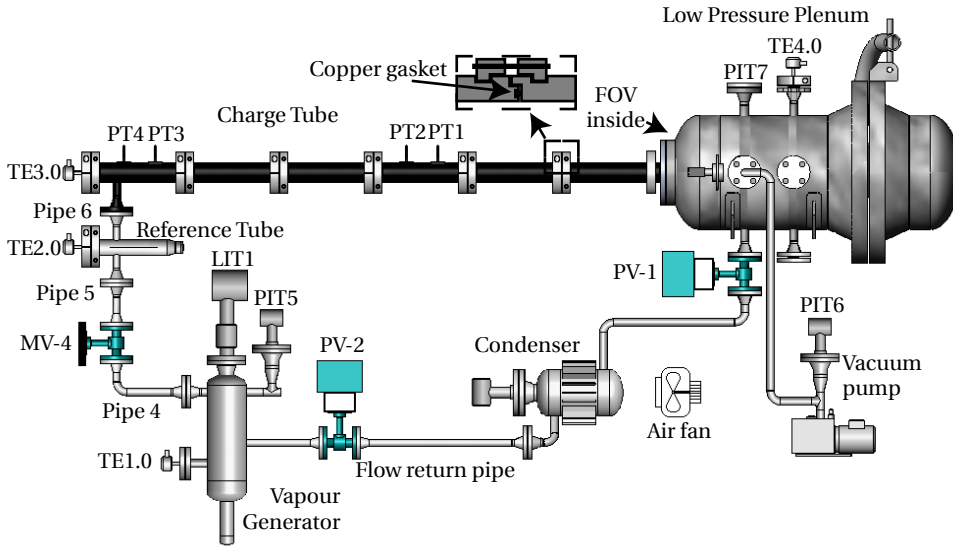


Figure 2.2: Overview of the FAST setup. The fast-opening valve is placed inside the low pressure plenum.

is closed using a Swagelok 2-way low temperature valve (type SS-8UW-TF) and any incondensable gases are removed by means of a Pfeiffer vacuum pump (type Duo 5 M) down to the vapour pressure of the fluid, which in case of pure  $D_6$  is predicted to be approximately 2 Pa at ambient conditions [49, 50]. The cylinder is then immersed into liquid nitrogen, which freezes the fluid and releases any dissolved impurities that are removed by using the vacuum pump after the fluid has melted. This freezing-thawing procedure is repeated a minimum of 2 times, before connecting the cylinder to pipe 1 of the vapour generator, which is displayed in figure 2.4. The facility is initially evacuated and closed off by a high temperature Swagelok 2-way valve (type SS-8UW-HT). Upon opening this valve, the working fluid flows under gravity forces through pipe 1 into the vapour generator, a custom made 5.9 liter stainless steel vessel, designed to heat and evaporate the working fluid up to the desired pressure under isochoric conditions. At the bottom of the vessel, the liquid can be extracted through a manually operated Tyco 19.05 mm globe valve (type Megastar) connected to flange F1 (figure 2.4) for gaschromatographic analyses or in case the fluid is to be replaced.

In order to attain the desired pressure and temperature, the fluid is first heated isochorically while enclosed in the vapour generator (valves MV-4 and PV-2 closed, see figure 2.2) by means of electrical heaters enveloping the bottom, mid and top sections of the vessel. Preliminary tests highlighted that accumulation of condensed fluid occurred in unheated sections of the vessel, specifically in pipe 2 (figure 2.4), inducing unwanted instabilities in the working fluid temperature when it flows back in the bulk, causing problems with the control system. In order to prevent these phenomena, all the walls of the vapour generator have been heated to limit the condensation of the working fluid.

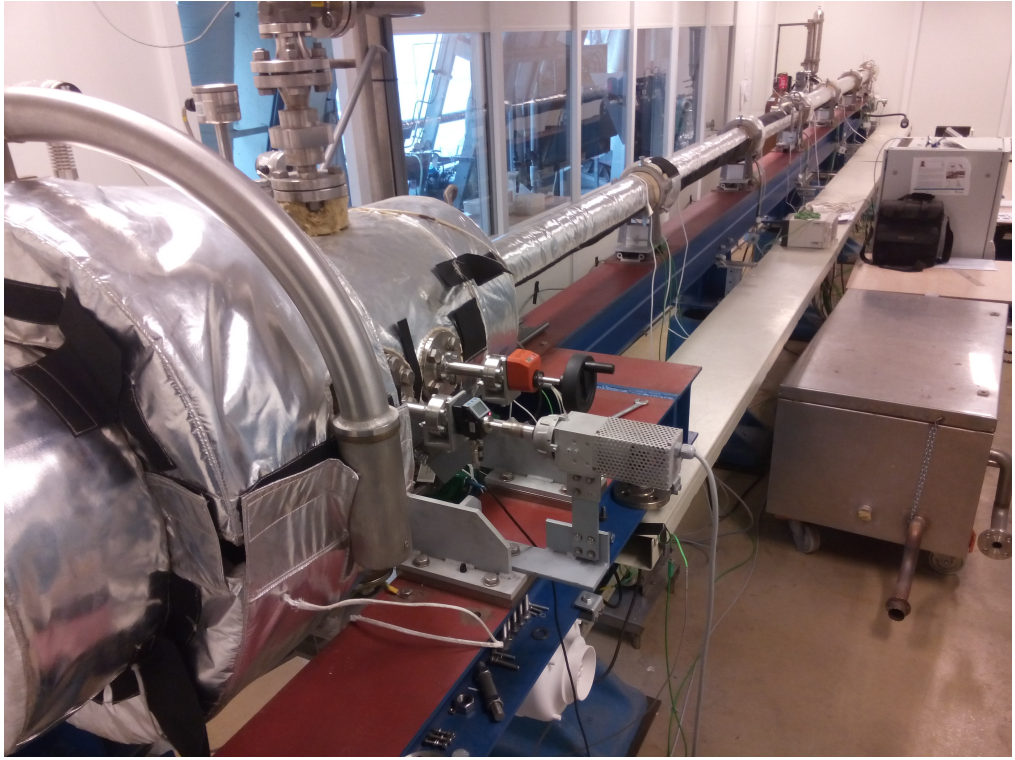


Figure 2.3: Picture of the FAST setup.

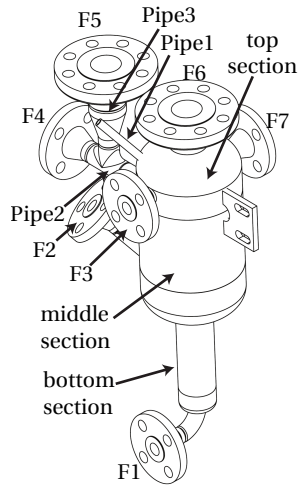


Figure 2.4: Drawing of the vapour generator. The numbers correspond to the flanges connecting with the following equipment: F1: outlet to extract liquid, F2: PT-100 sensor, F3: return pipe from the LPP, F4: burst disc, F5: static pressure transducer, F6: liquid level meter, F7: reference tube

Most of the thermal energy is supplied to the vapour generator by a 1.5-kW Kurval ceramic band heater (custom built ETB HRHK-type) covering the bottom section, see figure 2.4, because the lower part of the vapour generator is always in contact with liquid. This ensures a high heat transfer coefficient between the heater and the liquid fluid inside the vessel and helps avoiding hot spots that could trigger thermal decomposition of the fluid. A KWX 2-mm conducting graphite layer (type KU-CBGA2000-0H) inserted between the band heater and the metal wall solved initial problems due to insufficient thermal contact between the band heaters and the wall. Thanks to its high in-plane thermal conductivity, the graphite layer conducts the supplied thermal power uniformly along the metal wall, thus ensuring an even surface temperature distribution. The main section of the vessel is heated by a 2.8-kW ceramic band heater (custom built ETB HRHK-type), also in combination with a 2-mm conducting graphite layer. At the top of the vessel, it was impossible to place a band heater due to the presence of numerous flanges. Instead, a 6-m long 1-kW Welvy Joule dissipation heating wire (type HSQ/060) is used. A second heating wire of the same type is wrapped around pipe 2 and 3, see figure 2.4, and a third one around pipe 4 connected at flange 7, see figure 2.2, in combination with a 2-mm graphite layer. Heat transfer from the vapour generator to the environment is limited as much as possible by a layer of minimum 50 mm rockwool insulation.

A safety precaution against pressure runaway in the vapour generator is implemented at flange F4 (figure 2.4) in the form of a combination of an Eriks rupture disc that bursts at a pressure of 27 bar with 5 % tolerance, which is followed by an Eriks 1 inch diameter spring-loaded safety valve (type 30.2) that is actuated at 27 bar. The burstdisc is placed in front of the safety valve, such that the latter is not in contact with the hot working fluid, and can thus be made of a cheap material. The safety valve is placed to contain the fluid as much as possible in the vapour generator in case of breaking of the rupture disc.

Once the desired pressure is attained in the vapour generator, a manually operated Tyco 19.05-mm globe valve MV-4 (type Megastar) is opened and vapour flows through pipe 4 to the reference tube (RT) and charge tube (CT), see figure 2.2.

The purpose of the RT is to finely control the degree of superheating of the vapour and to provide a reference for the thermal control of the CT, as further explained in section 2.2.2. The RT is a 500-mm-long tube with an internal diameter of 40 mm and 15-mm thick walls. The thickness of the walls enhances an even distribution of the thermal power, which is needed to obtain a uniform temperature and to avoid hot spots. The thermal energy is supplied by two Tyco custom-made heating jackets around the tube, which includes a 25-mm glass silk insulation layer. A 335 W version is placed around the RT and a 180 W version around the flange of the RT. The heating jacket is chosen because an even temperature distribution is guaranteed by the manufacturer. Around pipe 6, see figure 2.2, a 2.1-m-long 370 W Welvy Joule dissipation heating wire (type HSQ/021) is wrapped with a 2-mm thick graphite layer placed underneath to ensure good thermal contact, because the small diameter of the pipe does not allow for a heating jacket.

The geometry of the CT and of the RT are identical, except for their length. The CT is composed of six pipe segments, each 1520 mm long. The pipe segments feature a male-to-female

connection, such that the segments overlap for 20 mm, see figure 2.2. The male side has a groove accommodating a red copper seal. A coupling holds the two segments together. This construction allows for satisfactory sealing both in case the inner volume is at superatmospheric pressure, or at subatmospheric conditions, and for accurate alignment. The CT assembly measures 9 m in total and is placed on a sliding support to allow for its thermal expansion when at high temperature, which is 55 mm at 400°C. Each pipe segment has been machined from a metal block to ensure maximum straightness and it is electrolytically polished on its inner surface to a roughness of 0.05  $\mu\text{m}$ . Each segment is fitted with a custom made Tyco 950 W Glass Silk heating jacket, which includes a 25-mm-thick insulation layer. The couplings between the elements are fitted with two 0.5-m Welvy 180-W Joule heating electric wire (type: HBQ/005), covered by a 25-mm glass silk insulation layer. Immersion of temperature sensors in the CT would inherently disturb the flow field of interest. Instead, the outside wall temperature is measured both in the RT and CT. Due to the same dimensions of the reference tube and the charge tube, the total length being the only exception, the same temperature is imposed on the charge tube walls as on the RT. This results in the same fluid temperature inside the tube, under the assumption that the length of the tube has a negligible influence.

The end of the CT is closed off by the FOV, arguably the most complex mechanical part of the setup, see figure 2.5. This custom-designed stainless steel valve, designed to open within 4 ms, is able to operate at high temperatures without lubrication to avoid contamination of the working fluid. It might however be expected that the siloxane working fluid condenses while flowing through the FOV, thus acting as a lubricant. Alternatively, the fluid might even lubricate by being in the vapour phase, due to its close-to-liquid density [51]. The valve is contained in the LPP and can be operated remotely, keeping the entire facility hermetically sealed for multiple experiments. In the opened position, the working fluid can flow through venting holes present in the inner and outer body in the radial direction. In the closed position, a sliding cylinder is pushed between these bodies, obstructing the flow through the venting holes. The sliding cylinder presses into a Kalrez compound sealing pad on the flange to ensure sealing. On the other side, the sealing is performed by a Kalrez O-ring with a diameter of 47.22 mm and a thickness of 3.53 mm between the sliding cylinder and the inner body. The groove that hosts the O-ring has been carefully designed in order to allow for the thermal expansion of the perfluoroelastomer. The surface of the sliding cylinder has been coated with a Diconite solid lubricant coating to reduce friction with the O-ring. Since the thermal swelling of the O-ring has a strong effect on the friction of the sliding cylinder during the fast opening, a 3-mm thermocouple (K-type) inserted in a hole in the mounting flange of the FOV monitors the temperature of the steel. An Inconel steel spring is compressed and three radial clamps engage the pre-slider to prevent the spring from being released. To open the valve, the actuation system moves the clamps in outward direction, allowing the spring to push the sliding cylinder and the pre-slider away, thus leaving the venting holes open. A nozzle insert creates a throat area in order to choke the flow, thus preventing flow disturbances from travelling upstream. For this reason the throat is located downstream of the sealing, as opposite to solutions that are typical in Ludwig tubes [52, 53]. It can be moved remotely in the longitudinal direction to change the throat area section, between approximately 420 mm<sup>2</sup> and 600 mm<sup>2</sup> to modulate the strength of the rarefaction waves.

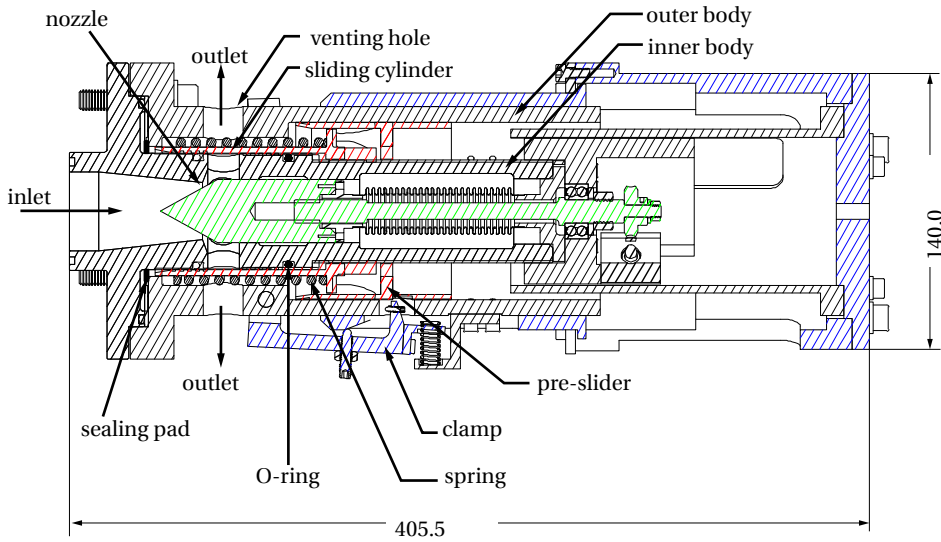


Figure 2.5: Drawing of the cross-section of the Fast Opening Valve. The actuation system (in blue) slides slowly to the right side, which pushes the clamps outward. Once the clamps release the pre-slider, the fast moving components (in red) come into motion because the compressed spring pushes the sliding cylinder and the pre-slider away. After the sliding cylinder is pushed across the venting holes, the fluid is free to flow from the inlet to the outlet. The nozzle insert (in green) can be moved in the longitudinal direction in order to control the throat area.

The FOV is contained in the Low Pressure Plenum (LPP), a 113-l cylindrically shaped vessel, see figure 2.2. The LPP has an outer diameter of 406.4 mm and 9.53-mm-thick stainless steel walls. The electric motor triggering the FOV and the manual nozzle positioning gear are mounted on the LPP with feedthrough shaft connections sealed with copper gaskets. An Eriks rupture disc with an overpressure valve ensures safety in case of an uncontrolled pressure increase above 27 bar. A lid with a 648 mm diameter flange gives access to the vessel interior for installation of the FOV, and it is sealed by a graphite gasket compressed by 20 bolts. The thermal input to the vessel is supplied by 4 custom built Tyco heating jackets with a nominal power of 1450 W, 425 W, 960 W and 490 W respectively, each featuring also a 25-mm glass silk insulation layer.

A pneumatic Tyco 19.05-mm globe valve (type Megastar) PV-1, see figure 2.2, connects the LPP to a cylindrically shaped stainless steel air-cooled condenser with an outer diameter of 168.28 mm and 7.11-mm-thick walls. A 98-mm diameter Itho tube fan (type BUTP 100) blows air over 20 cooling fins with a length of 120 mm and width of 30 mm, which are welded to the vessel to enhance cooling. The condensed liquid flows from the bottom of the condenser into the 24.8-mm inner diameter inclined flow return pipe that has 1-mm-thick walls, where the liquid is collected. This pipe is connected through another Tyco pneumatic 19.05-mm globe valve (type Megastar) PV-2, see figure 2.2, at flange F3, see figure 2.4, such that the fluid can flow into the vapour generator.



### 2.2.2. INSTRUMENTS, DATA ACQUISITION & CONTROL

Two separate subsystems are implemented and connected to a personal computer for data visualization, monitoring and post-processing: one is specifically for the acquisition of data related to experiments, while the other operates to monitor and control the fluid conditions in the facility. A schematic overview of the data acquisition system is given in figure 2.6

Most signal conditioning and control hardware and software of the FAST setup is made by National Instruments (NI). The pressure and temperature signals that fully characterize experiments are conditioned by boards located inside a data acquisition chassis (NI PXI 1033). The monitoring and control is performed by two programmable automation controllers (PAC, NI Compact FieldPoint cFP-2100). The PXI and the Compact FieldPoint systems are located both in a suitable rack. The code related to the data acquisition functionality and the code related to the control algorithms is implemented into the *FAST Manager* program, an in-house NI LabView program partly running on the PACs (for the critical control functions) and partly on the personal computer.

The thermal energy supply to the various sections of the facility is regulated by digital PID controllers running on the cFP-2100 units, and the voltage supply to the heating elements is modulated via RKC 1-phase thyristors (model: THV-1PZ-020-5\*NN-6).

In the vapour generator, the static pressure had initially been used as process variable for the main heater at the bottom section, measured by a Klay pressure transmitter (type 2000-SAN-4-F(w)-I-HT-G43) connected at flange F5 in figure 2.4 with a specified accuracy of 0.1 % of the full range of 10 bar. Because the operating pressure range of the vapour generator spans from very far from the critical point to close-to-critical conditions, the response in pressure to the supplied thermal power changes dramatically, because of the variation in the pressure derivative with respect to temperature at constant specific volume  $(\partial P/\partial T)_v$ . Consequently, the PID parameters should also be adapted depending on the operated pressure. This is avoided by converting the pressure into a saturation temperature with the help of in-house software [54] implementing suitable fluid thermodynamic property models, (see e.g. Nannan and Colonna [50]). Now the same PID parameters can be used throughout the entire operating range, because the change in specific heat capacity is sufficiently moderate. At the same time, the fast response of the pressure transmitter is still exploited for the control. The fluid saturation temperature is compared by a direct measurement of the liquid temperature as sensed by a Klay 4-wire Pt-100 sensor with insertion length of 180 mm and 6 mm diameter (type TT-E-D-F-L180xD6-S-P2-P13) mounted on flange F2, see Fig 2.4, which is calibrated using a Presys calibration oven (type T-350P) to within a tolerance of 0.12 °C.

The other heaters on the vapour generator are regulated each based on the temperature difference as measured by a 1-mm-thick thermocouple (K-type) and the fluid temperature. Additionally, 5 thermocouples are placed for monitoring purposes to detect hot spots and to monitor whether an even temperature distribution is obtained. All thermocouples are placed underneath the heater between the wall and the graphite layer. The liquid level in the vessel is monitored by a Endress Hauser guided radar liquid level meter (type Levelflex M FMP45-ABKARJB21C2B), mounted at flange F6 (figure 2.4).

The heat supply to the RT is regulated by a PID controller using as process variable the difference in temperature between the liquid in the vapour generator and the vapour in the RT. The temperature in the RT is measured with a Klay 3-wire Pt-100 sensor with an insertion length of 250 mm and 6 mm protrusion diameter (type TT-E-D-F-L250xD6-S-P2-P13), which is calibrated in the same manner as the one in the vapour generator. An identical resistance temperature detector (RTD) is used to monitor the temperature in the CT.

The fluid temperature inside the CT is controlled by imposing the same wall temperature on the CT as on the RT, which have the same dimensions, except for the length. The process variables are the differences in wall temperature between the RT and the individual CT pipe segments and couplings. Instead of measuring the temperature of the two thermocouples and calculating the difference in temperature, here the two thermocouples are connected to each other and the voltage difference is directly measured to reduce the measurement error. The wall temperature is measured in a groove in the RT and in each CT element or CT coupling using 0.5-mm-diameter thermocouple (type K) of 1 m length, which is bonded to the tube with Aremco silver-filled conductive ceramic adhesive (type 597A) to ensure the correct measurement of the wall temperature.

Less accuracy is required for the thermal control of the LPP, because its only purpose is to limit temperature gradients in the charge tube by reducing heat conduction. Therefore, only a single digital PID controller is implemented in order to regulate the power supply to all the heaters on the LPP. The process variable is the temperature as it is measured with a Klay 4-wire Pt-100 sensor with an insertion length of 180 mm and diameter of 6 mm (type TT-E-D-F-L180xD6-S-P2-P13), which is calibrated in the same manner as the other RTDs.

The signals from Pt-100s TE1.0, TE2.0 and TE4.0 (figure 2.2) go through a PR 2-wire transmitter (type 6333) to convert the signal into a linear 4-20 mA one. Consequently, these signals, together with the other 4-20 mA signals from liquid level meter LIT1 and from the static pressure transducers PIT5-PIT7, are converted to a voltage signal using a 249  $\Omega$  resistance and connected to the cFP-2100 PAC through a 16-bit analog input module (type cFP-AI-110). The thermocouple signals are connected using a 16-bit input module specific for these sensors (type cFP-TC-120).

Four dynamic pressure measurement stations PT1-PT4 are created by flush mounting a high-temperature Kulite fully active four arm wheatstone bridge pressure transducer (type XTEH-10LAC-190M-21bar-A) that measures the pressure with an accuracy of 0.5 % of the full scale of 21 bar along the CT at a distance of 4, 4.3, 8.4 and 8.7 m from the FOV, respectively, see figure 2.2. The signals are scaled after each experiment with the more accurate value of the pressure before and after the experiment, measured by the static pressure transducers. The sensors are placed in pairs to give the possibility to have a time of flight measurement at two different locations in the tube. The 0-100 mV signals of the dynamic pressure transducers are amplified with a custom-built amplifier with a gain of 100 and connected to a 16-bit data acquisition card (NI PXI 6143) that digitizes the signal in a simultaneous manner at a frequency of 250 kHz. A rise time of the pressure signals of 30  $\mu$ s has been measured

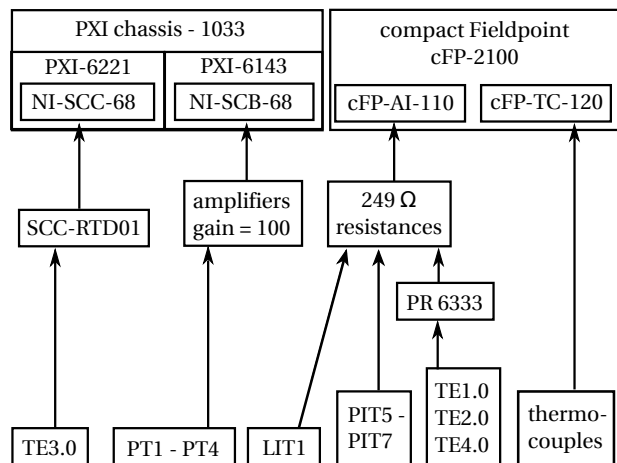


Figure 2.6: Schematic overview of the data acquisition and control system. The data acquisition system (NI PXI) conditions all the measurement signals relevant to the rarefaction wave experiments, while the control and monitoring system (NI Compact FieldPoint) is dedicated to the regulation and management of the FAST. The nomenclature of the signals corresponds to that shown in figure 2.2.

using a shock test. The RTD in the CT (TE3.0) is connected via a RTD input module (type SCC-RTD01) to a separate 16-bit data acquisition card (NI PXI-6221).

## 2.3. FACILITY CHARACTERIZATION

### 2.3.1. VACUUM AND PRESSURE SEALING

Avoiding the contamination of the working fluid with air and/or moisture is of utmost importance, since organic fluids thermally decompose at high temperature, and water and oxygen are known catalysts for these reactions, (see, e.g. Calderazzi and Colonna di Paliano [18], Dvornic [19], Colonna [55]). Moreover, also the contamination by an inert gas has to be avoided, because those gases typically feature much higher speed of sound values than the organic compounds under scrutiny, thus even a small amount of light gas mixed with the organic fluid can have a strong influence on wave propagation. To prevent air from leaking in during the idle times of the facility, the entire setup is usually pressurized with nitrogen, which, being inert, helps limiting the absorption of air or moisture into the working fluid and their adsorption on the internal metallic surfaces. The facility needs therefore to be evacuated before use. On the other hand, also leakage of (possibly hot) working fluid to the ambient must be avoided in order to prevent hazard and environment contamination and to ease the control of the pressure. Notably, these requirements must be satisfied within the whole operating temperature range.

A comprehensive series of tests have been conducted up to temperatures of 300°C, for a duration of 72 hours each, to evaluate the leak rate of the facility. The test results allowed to assess that the temperature has a negligible influence on the sealing properties of the equipment. The tightness of the FAST setup has been characterized in terms of the average leak

rate  $LR = \Delta P V \Delta t^{-1}$  [56], where  $V$  is the volume of the whole setup (i.e.  $0.143 \text{ m}^3$ ), and  $\Delta P$  is the pressure drop/rise measured after a time interval  $\Delta t$  (i.e. 3 days for all the tests) and resulted in the following leak rates:

- Low P ( $\lesssim 3 \text{ mbar abs.}$ ):  $LR < 5 \cdot 10^{-4} \text{ mbar l s}^{-1}$  (air into the system)
- High P ( $\gtrsim 6000 \text{ mbar abs.}$ ):  $LR < 5 \cdot 10^{-2} \text{ mbar l s}^{-1}$  (helium to the ambient)

The most critical aspect of air leaking into the facility, which can happen during the approximately 2 hours it requires to raise the pressure in the vapour generator up to atmospheric conditions, is calculated to be less than 0.01 % of the total mass of fluid. In terms of deviation in speed of sound the effect becomes more important close to the fluid critical point, but is always less than 0.5 %. It is known that thermal decomposition is not linear with temperature, and that is dependent on an impurity threshold, which decreases at higher temperatures [18]. In case of siloxane  $D_6$ , up to  $300 \text{ }^\circ\text{C}$ , no appreciable change in composition has been detected by inspecting the periodical gas-chromatographic analyses on working fluid samples.

### 2.3.2. COMPRESSION SHOCK EXPERIMENT IN NITROGEN

To verify the correct functioning of the measurement system, a shock experiment in nitrogen is performed, see figure 2.7. The pressure in the CT is set to 0.57 bar, while the LPP is at 1.99 bar. Both sides are at atmospheric temperature of  $23.8 \text{ }^\circ\text{C}$ . Upon opening the FOV, a compression propagates through the nozzle into the stagnant fluid in the charge tube, eventually forming a classical compression shock in the CT with subsonic post-shock conditions at state B. In the nozzle, a steady choked flow is formed, which accelerates the fluid up to supersonic speeds. A stationary normal shock is formed in the nozzle that decelerates the supersonic flow in the nozzle to the subsonic flow at state B in the CT.

Figure 2.8 shows the pressure recordings from the experiment. The shock has not formed yet at the location of sensor PT1 and PT2, which can be seen by the relatively low value of the measured pressure gradient, if compared to signals recorded by PT3 and PT4. This is due to the finite opening time of the FOV, which causes the initial pressure profile to span a finite time interval. During propagation, the compression steepens and forms a shock wave. A portion of the pressure rise at PT1 and PT2 displays a lower pressure gradient. Such trend in the pressure signal can be attributed either to the complexity of the FOV opening process, or to the propagation of the compression through the nozzle [57], or to the partial formation of the shock. At the location of sensor PT3 and PT4, a single shock wave has formed, which is reflected at the end wall of the CT.

The wave propagation speed equals  $u + c$  for right-running waves, in which  $c$  is the local speed of sound and  $u$  is the local flow velocity in the laboratory frame. An experimental value is obtained with the time-of-flight method. First, the relevant part of the pressure signal is selected as follows: the beginning of the wave at  $t = t_{\text{start}}$  is formally identified as the time when the pressure departs from the initial value  $P_{\text{CT}}$  more than 15 mbar. The threshold is chosen such that it exceeds the noise level. The end of the unperturbed portion of the signal is chosen when the head of the wave is expected to reach the end of the CT at  $t = t_{\text{end}}$ .

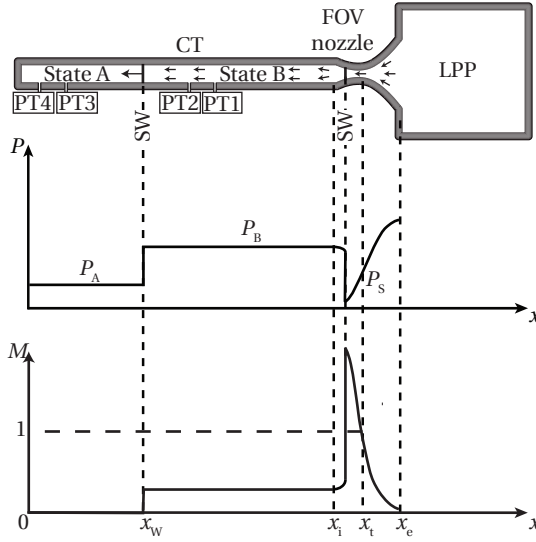


Figure 2.7: Schematic overview of the compression shock wave experiment in nitrogen and the qualitative pressure and Mach profiles resulting from the opening of the FOV. A compression forms and propagates into the charge tube, where eventually it coalesces into a shock. In the nozzle, a steady choked flows forms in which the gas from the LPP is accelerated to supersonic speeds, after which the flow is brought back to subsonic speed, e.g. with a standing normal shock, to comply with state B in the CT.

The estimate is performed by using the speed of sound from the accurate nitrogen thermodynamic model, namely the ideal gas model in this regime; therefore  $t_{\text{end}} = t_{\text{start}} + \Delta x / c_{\text{model}}$ , where  $\Delta x$  is the distance between the sensor location and the end of the CT. The relevant portion of the signal  $\Delta P_{\text{rel}}$  spans from  $P_{\text{start}}$  to  $P_{\text{end}}$ . This span is divided into intervals of 0.64 mbar, equal to two times the resolution of the pressure signal. The time-of-flight method is applied to corresponding subintervals from different sensors to compute the local wave propagation speed.

A theoretical isentropic curve is obtained by evaluating the speed of sound and flow velocity as a function of the pressure drop. The speed of sound is determined from the value of the pressure using the thermodynamic model, and assuming an isentropic expansion. The constant value of the entropy is computed using the thermodynamic model from the initial conditions. The local flow velocity is obtained by evaluating the Riemann invariant in the undisturbed state, which is constant within this simple wave [6]. The propagation speed of a shock does not vary within the compression profile. The shock speed is computed using the Rankine-Hugoniot relation with the measured pressure jump. Figure 2.9 shows the chart that can be obtained to this end.

The experimental value of the wave propagation speed determined using sensor PT1 / PT2 and PT3 / PT4 is reported in figure 2.9 as a function of  $\Delta P = P - P_{\text{CT}}$ . The experimental value obtained from the PT1 / PT2 signals follows the theoretical isentropic value to within 2.5 %, except for  $\Delta P$  values between 0.2 to 0.26 bar. This pressure level corresponds to the section

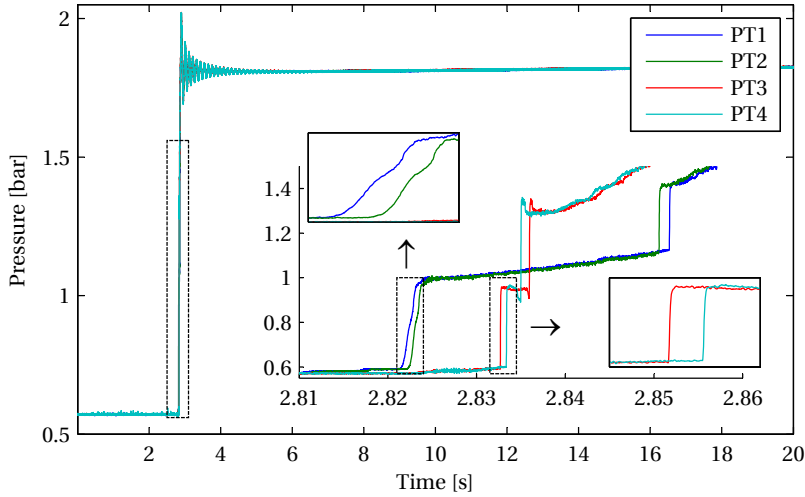


Figure 2.8: Pressure recordings from an experiment resulting in shock formation in nitrogen. The moderate gradient of the pressure when the compression passes PT1 and PT2 for the first time indicates that the shocks have not formed yet. Once it passes PT3 and PT4 and is reflected by the tube end wall, the gradient is much higher.

of the compression with a lower pressure gradient as discussed above. As the compression wave propagates, the pressure level of the low gradient section of the wave changes to a pressure level that is a few millibars higher. By using the time-of-flight method on this section, a higher value of the calculated propagation speed is found.

At the location of sensor PT3 and PT4, a fully formed single shock is measured, providing an experimental value of the shock velocity of 438.6 m/s. This is 0.5 % off with respect to the theoretical value of 440.6 m/s, determined by using the Rankine-Hugoniot equations for a pressure jump from the initial pressure of 0.57 bar to the post-shock pressure of 0.95 bar in nitrogen at that temperature.

### 2.3.3. RAREFACTION WAVE EXPERIMENTS USING INCONDENSIBLE GASES

A series of rarefaction wave experiments are performed in order to characterize the opening time of the FOV. The expansion is obtained by pressurizing the CT and by keeping the LPP at a lower pressure. After the FOV opens, a rarefaction travels into the CT, decreasing the pressure from stagnant state A to state B, and starting a flow through the nozzle into the LPP, see figure 2.10. In the throat of the nozzle, sonic conditions are attained.

The experiment is illustrated in an position-time diagram in figure 2.13, in which exemplary characteristic curves are displayed. If the opening of the valve were instantaneous, all characteristics would emerge from the origin of the chart. In a straight pipe without any area changes, the characteristics are straight lines as shown in figure 2.13(a). In the case of the actual valve opening, featuring a finite opening time, the limiting characteristic emerges from the valve position at a later time instance, see figure 2.13(b). Moreover, since the seal of the

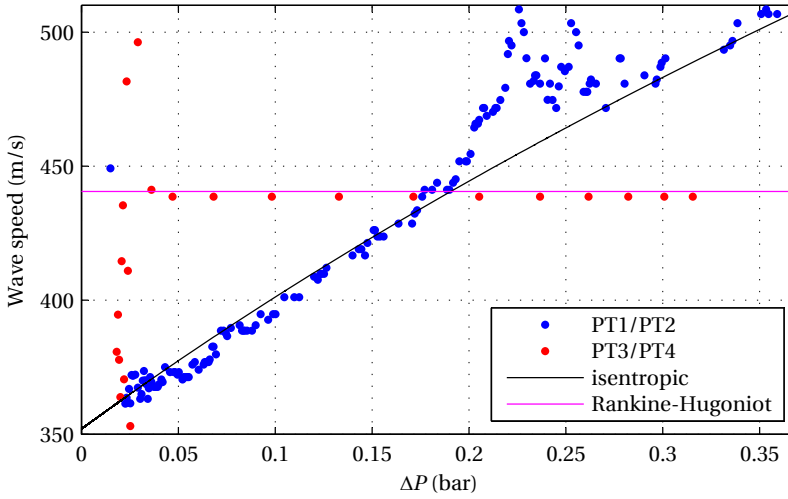


Figure 2.9: Measurement of the wave speed in nitrogen, determined with the time-of-flight method. The blue dots are obtained by comparing PT1 with PT2, when the shock has not formed yet. The red ones are obtained by comparing PT3 with PT4 when the shock has formed. The black line shows the theoretical value of the wave propagation speed for an isentropic expansion. The magenta line shows the wave speed for a shock having the measured pressure ratio and calculated using the Rankine-Hugoniot equations.

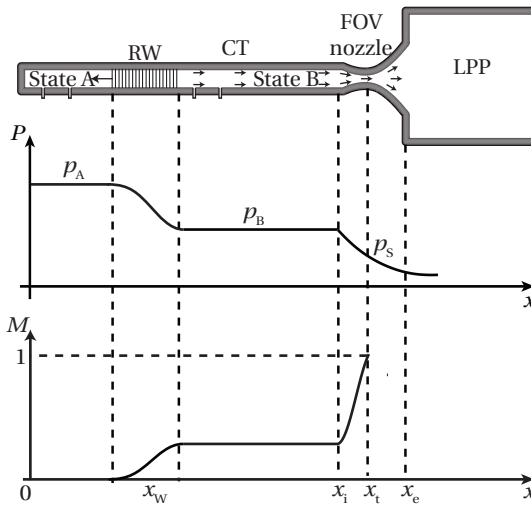


Figure 2.10: Schematic overview of a rarefaction wave experiment. The charts refer to qualitative pressure and Mach number profiles along the tube, after the opening of the FOV. A rarefaction fan propagates into the charge tube at sonic speed  $W$ . The fluid is accelerated from rest condition A to condition B and flows into the reservoir through the nozzle. At the nozzle throat, sonic conditions S are attained.

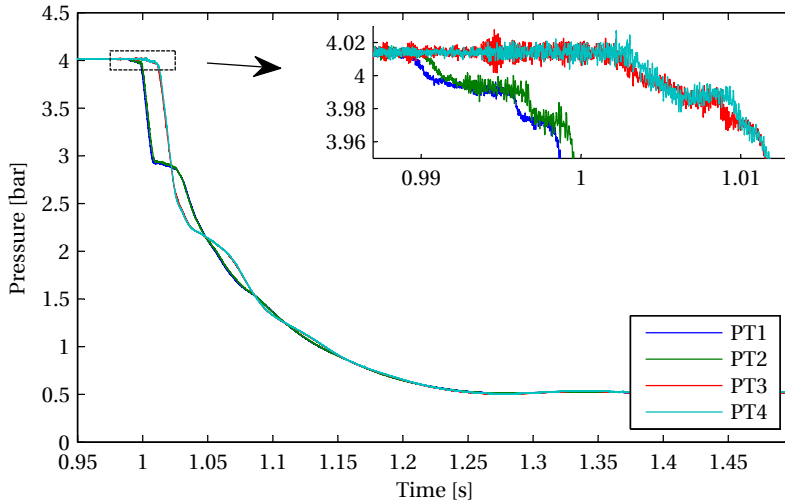


Figure 2.11: Pressure signals of experiment 25 measured by transducers PT1 to PT4. The valve opening results in a pressure drop from 3.97 bar to 2.88 bar, which is preceded by two other small pressure drops. These are attributed to an initial leakage flow that starts as soon as the FOV sliding cylinder detaches from the seal.

FOV is located downstream of the nozzle, the rarefaction propagates through the nozzle before entering the CT. The flow is accelerated in the nozzle, due to the varying cross-sectional area. This results in a higher local flow velocity than expected by a pure 1D assumption, and consequently the wave propagation speed is lower than in the rest of the tube. When the characteristics are plotted in a time-space diagram, they show up as curved lines in this section [58].

Figure 2.11 shows the pressure measurements of a rarefaction experiment (nr. 25 from Table 2.1) in nitrogen with an initial pressure of 4.01 bar in the CT and vacuum in the LPP. From these data, the FOV opening sequence can be inferred: as soon as the clamps are released, see figure 2.5, the spring pushes the slider away, and a small opening is created as the slider leaves the seal, choking the flow close to this position. This is believed to cause a small pressure drop of approximately 20 mbar in the signal. As the slider moves further, the position of minimum cross-section changes to a location between the slider and the inner body, which is slightly larger than the initial choked section. This is revealed by a second small drop in the pressure of approximately 20 mbar. Only when the slider finally passes over the venting hole of the inner body, the designated nozzle gets choked. This corresponds to the large pressure drop in the pressure signal down to 2.88 bar.

Using the time-of-flight method reported in section 2.3.2, the local wave propagation speed during a rarefaction experiment can be determined. Figure 2.12 shows the charts that can be obtained to this end, using experiment 25 as an example. Wave speed values as a function of the measured pressure drop are shown together with the theoretical curve and two fitting curves: a linear fit and a shift of the theoretical curve with the average deviation from



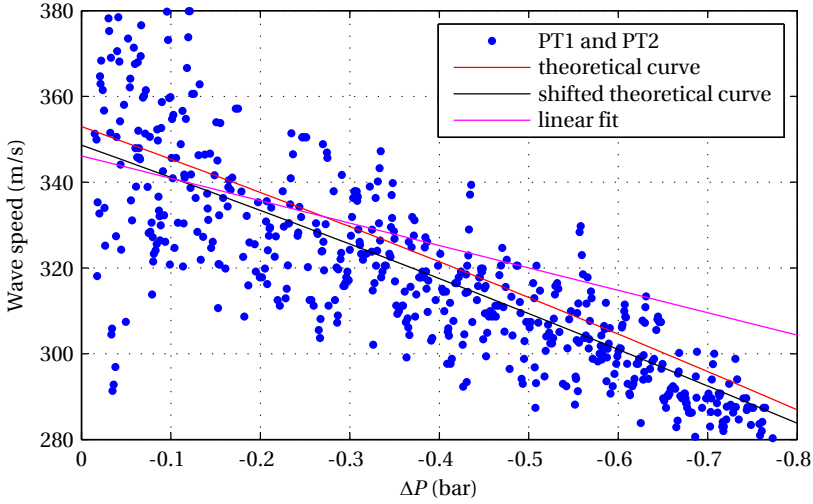
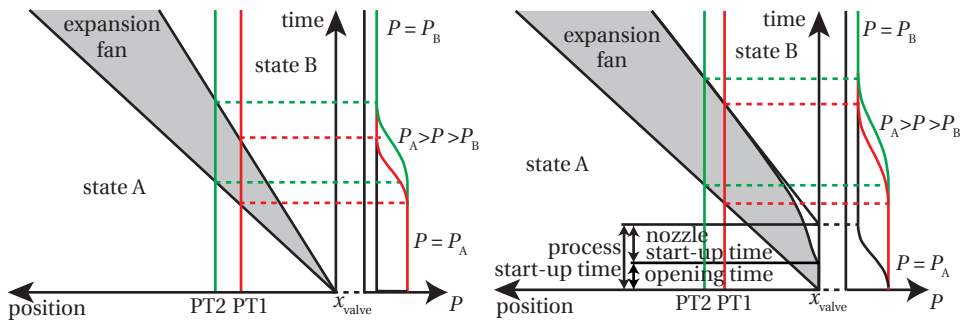


Figure 2.12: Wave Speed in  $N_2$  as a function of the pressure drop. The blue dots are the values obtained from pressure signals by applying the time-of-flight method. The red line is the theoretical curve as obtained with a reference thermodynamic model. The black line is a fit of the values obtained with the experiments using an offset of the theoretical curve. The magenta line is a linear fit of the data. The shifted theoretical curve and the linear fit are made based on 25 % of  $\Delta P_{rel} = -0.2$  bar

the experimental curve. The fitting curves give an estimate of the speed of sound in the undisturbed state, as the wave propagation speed tends to the speed of sound as  $\Delta P \rightarrow 0$ . To eliminate inaccuracies introduced by the FOV in the determination of the speed of sound, only the first 25 % of the relevant pressure span is taken, while keeping a minimum of 40 mbar, such that  $\Delta P_{max} = \max(0.25P_{rel}, 0.04 \text{ bar})$ . The resulting speed of sound  $c_{fit}$  and  $c_{offset}$  are reported in table 2.1. For air,  $CO_2$  and  $N_2$ , both methods deliver an accurate estimate of the speed of sound, compared to the value obtained from the reference thermodynamic model [59]. The only exception is the linear fit for experiment 23. The average error and standard deviation with respect to the model are  $2.1 \% \pm 1.6 \%$  and  $1.1 \% \pm 1.1 \%$  for the linear fit and the theoretical offset, respectively. For helium, the average error and standard deviation with respect to the model are  $5.1 \% \pm 4.6 \%$  and  $4.0 \% \pm 3.1 \%$  for the linear fit and the shifted theoretical curve, respectively. The reason for the larger error is possibly due to the finite process start-up time of the FOV in combination with the higher speed of sound of helium resulting in a very small usable portion of the signal.

The process start-up time of the FOV is determined by reconstructing the pressure signal at the valve location from the original pressure signals, by subtracting for each data point, the propagation time of a wave from the valve location to the sensor location at the local wave speed  $t_{rec} = t - w\Delta x$ , see figure 2.13(b). The value of  $w$  is estimated by assuming a homentropic flow and using the thermodynamic model for the measured pressure level, as described in section 2.3.2. In the reconstructed signal, the time duration of the pressure drop corresponds to the process start-up time.



(a) ideal case with instantaneous valve opening and (b) real case with non-instantaneous valve opening and nozzle

Figure 2.13: Qualitative position-time diagrams referred to classical expansion fans, with corresponding pressure diagrams at measurement stations PT1 and PT2. In the ideal case (instantaneous valve opening) and in the absence of a nozzle, all characteristics emerge from a single point and the pressure drop is instantaneous. In the actual case, due to the finite FOV opening time, the pressure drop is not instantaneous and consequently the limiting characteristic starts at a later time instance, as the first characteristic. All characteristics except the first are curved in the nozzle area, because of the flow acceleration in this section, which decreases the wave propagation speed.

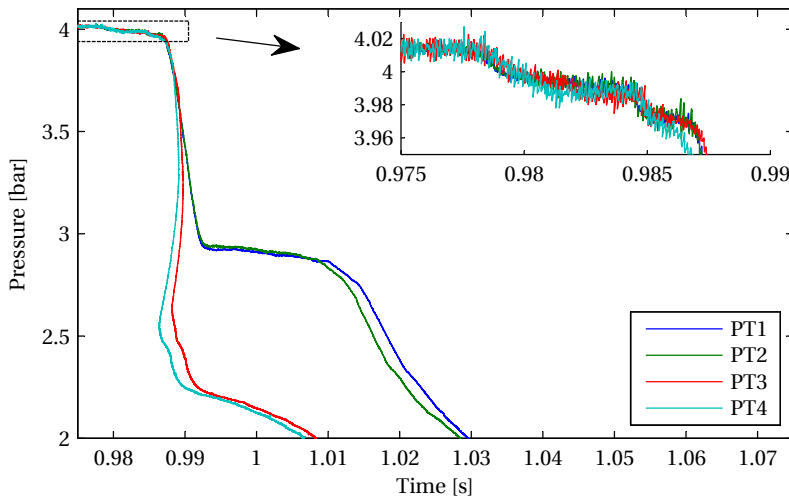


Figure 2.14: Section of the signals recorded by pressure sensor PT1 to PT4 during an expansion in nitrogen mapped to the valve position. All signals initially overlap, demonstrating that the mapping procedure is correct. The PT3 and PT4 signals start to deviate from the other two signals once the rarefaction is reflected at the end of the tube, thus creating a non-simple region.

Figure 2.14 shows the resulting signals at the valve location of all four sensors for experiment 25, see table 2.1. Since the signals are mapped to the same location, i.e. the valve location, the initial portion of all signals coincides. Below a pressure level of 3.7 bar, signals from sensor PT3 and PT4 deviate from the other two signals. Such deviation can be explained by the reflection of the rarefaction waves once they reach the end of the tube, which creates a non-simple region [6]. The local flow velocity is then incorrectly evaluated and it makes PT3 and PT4 unsuited for the determination of the process start-up time.

The process start-up time has been evaluated for several experiments using He, air, CO<sub>2</sub> and N<sub>2</sub> as working fluids, different pressure levels and nozzle areas, see table 2.1, experiments 1 to 25. Given the need of comparing opening times at various pressure levels, temperature and fluids, we define the process start-up time as the time duration between when 5 % of the pressure drop and when 95 % of the pressure drop of the reconstructed signal has occurred. The boundaries have been chosen such that the signal maximum noise level does not exceed these values in all considered experiments. As expected, the value of the throat area in the nozzle affects the measured process start-up time.

The effective nozzle area, which also depends on multi-dimensional and viscous effects, is not easily recovered from the FOV geometry and therefore it is inferred from the measurements by assuming a steady quasi one-dimensional isentropic flow from state B through the choked nozzle. The mass flow is evaluated using the known cross-sectional area of the CT, the evaluated flow velocity using the Riemann invariant from state A and the density of state B, which is calculated by using the isentropic relations from state A. With a very small calculated throat area of 61-79 mm<sup>2</sup>, performed with a special nozzle insert, the measured process start-up time is between 2.1 and 3.2 ms, see table 2.1, which is well within the design requirement of 4 ms. Without the nozzle insert, the calculated throat area is between 418 and 576 mm<sup>2</sup>, and the process start-up time is between 3.5 and 4.9 ms for all experiments with incondensable gases.

## 2.4. RAREFACTION WAVES IN SILOXANE D<sub>6</sub>

In order to demonstrate the correct operation of the setup for the functionality it was designed for, i.e., wave measurements in dense vapors of organic fluids, preliminary experiments to measure the expansion wave speed in D<sub>6</sub> (dodecamethylcyclohexasiloxane, C<sub>12</sub>H<sub>36</sub>O<sub>6</sub>Si<sub>6</sub>) were performed. Gaschromatographic analysis confirmed the specification of the supplier that the fluid has a 96 % purity. The experiments presented here are in the classical gasdynamic domain, namely all the thermodynamic states experienced by the fluid are outside the BZT region. Experiments at two different saturation levels were conducted with the aim of evaluating how the control system is able to keep the temperature constant and uniform at different temperature levels. At a saturation temperature of approximately 255 °C, experiments were done in which the fluid in the CT was superheated with 5 °C and 45 °C. At a saturation temperature of approximately 295 °C, experiments with 5 °C superheating were performed. Figure 2.15 shows the temperature of the fluid in the vapour generator and in the reference tube during the entire test campaign. Part of the liquid in the vapour generator is flashed once valve MV-4 is opened. The measured temperature fluctuations in the reference

| no | fluid           | $P_{CT}$<br>[bar] | $T_{CT}$<br>[°C] | $\Gamma$<br>[-] | $\Delta P_{wave}$<br>[bar] | $A_{geom}$<br>[mm <sup>2</sup> ] | $A_{eff}$<br>[mm <sup>2</sup> ] | $\Delta t$<br>[ms] | $c_{model}$<br>[m/s] | $c_{fit}$<br>[m/s] | $c_{offset}$<br>[m/s] |
|----|-----------------|-------------------|------------------|-----------------|----------------------------|----------------------------------|---------------------------------|--------------------|----------------------|--------------------|-----------------------|
| 1  | He              | 6.01              | 17.3             | 1.34            | 1.74                       | 460                              | 459                             | 3.9                | 1006                 | 998                | 964                   |
| 2  | He              | 4.90              | 22.7             | 1.34            | 0.28                       | 70                               | 79                              | 2.7                | 1014                 | 1014               | 1028                  |
| 3  | He              | 6.09              | 48.9             | 1.34            | 1.69                       | 460                              | 438                             | 3.7                | 1059                 | 1005               | 1072                  |
| 4  | He              | 6.50              | 50.0             | 1.34            | 0.32                       | 70                               | 67                              | 2.5                | 1060                 | 1121               | 955                   |
| 5  | He              | 6.66              | 99.2             | 1.34            | 2.01                       | 460                              | 483                             | 3.6                | 1138                 | 1274               | 1169                  |
| 6  | He              | 6.02              | 149.4            | 1.34            | 1.84                       | 460                              | 489                             | 4.1                | 1212                 | 1225               | 1182                  |
| 7  | He              | 7.29              | 269.4            | 1.34            | 0.33                       | 70                               | 62                              | 2.1                | 1373                 | 1547               | 1348                  |
| 8  | He              | 8.47              | 269.9            | 1.34            | 0.44                       | 70                               | 72                              | 3.2                | 1374                 | 1424               | 1483                  |
| 9  | air             | 6.31              | 17.6             | 1.21            | 1.62                       | 460                              | 456                             | 4.2                | 343                  | 341                | 341                   |
| 10 | air             | 4.08              | 18.0             | 1.20            | 0.97                       | 460                              | 418                             | 4.2                | 343                  | 338                | 339                   |
| 11 | air             | 7.01              | 19.1             | 1.21            | 1.81                       | 460                              | 459                             | 4.2                | 344                  | 338                | 339                   |
| 12 | air             | 4.86              | 20.0             | 1.21            | 0.21                       | 70                               | 67                              | 2.3                | 344                  | 359                | 350                   |
| 13 | air             | 5.39              | 20.0             | 1.21            | 0.23                       | 70                               | 68                              | 2.3                | 344                  | 344                | 353                   |
| 14 | air             | 7.13              | 22.0             | 1.21            | 0.30                       | 70                               | 67                              | 2.2                | 345                  | 338                | 347                   |
| 15 | air             | 6.15              | 49.1             | 1.21            | 1.62                       | 460                              | 468                             | 4.2                | 361                  | 353                | 356                   |
| 16 | air             | 6.98              | 95.0             | 1.20            | 0.27                       | 70                               | 61                              | 2.2                | 386                  | 375                | 388                   |
| 17 | air             | 6.80              | 99.5             | 1.20            | 1.76                       | 460                              | 461                             | 4.0                | 388                  | 390                | 384                   |
| 18 | CO <sub>2</sub> | 5.99              | 18.0             | 1.13            | 1.50                       | 460                              | 471                             | 4.9                | 262                  | 257                | 259                   |
| 19 | CO <sub>2</sub> | 6.42              | 50.0             | 1.12            | 1.59                       | 460                              | 465                             | 4.6                | 275                  | 274                | 273                   |
| 20 | CO <sub>2</sub> | 6.64              | 100.3            | 1.12            | 1.64                       | 460                              | 464                             | 4.1                | 296                  | 294                | 293                   |
| 21 | CO <sub>2</sub> | 6.13              | 149.7            | 1.11            | 1.50                       | 460                              | 459                             | 4.4                | 314                  | 321                | 315                   |
| 22 | N <sub>2</sub>  | 1.09              | 25.3             | 1.20            | 0.35                       | 600                              | 576                             | 4.3                | 352                  | 337                | 338                   |
| 23 | N <sub>2</sub>  | 1.12              | 25.4             | 1.20            | 0.33                       | 600                              | 531                             | 4.4                | 352                  | 379                | 349                   |
| 24 | N <sub>2</sub>  | 4.00              | 25.7             | 1.20            | 1.00                       | 460                              | 443                             | 4.1                | 353                  | 360                | 353                   |
| 25 | N <sub>2</sub>  | 4.01              | 25.8             | 1.20            | 1.08                       | 460                              | 481                             | 4.2                | 353                  | 346                | 349                   |
| 26 | D <sub>6</sub>  | 1.26              | 264.2            | 0.86            | 0.09                       | 600                              | 169                             | 7.7                | 89.8                 | 89.5               | 88.4                  |
| 27 | D <sub>6</sub>  | 1.26              | 293.7            | 0.91            | 0.15                       | 600                              | 278                             | 6.6                | 94.3                 | 94.0               | 94.1                  |
| 28 | D <sub>6</sub>  | 1.27              | 298.0            | 0.91            | 0.18                       | 460                              | 328                             | 7.5                | 94.8                 | 96.9               | 93.9                  |
| 29 | D <sub>6</sub>  | 1.27              | 300.1            | 0.92            | 0.14                       | 600                              | 254                             | 5.6                | 95.1                 | 98.3               | 94.0                  |
| 30 | D <sub>6</sub>  | 2.52              | 301.1            | 0.79            | 0.26                       | 460                              | 254                             | 9.0                | 84.6                 | 84.9               | 83.5                  |
| 31 | D <sub>6</sub>  | 2.38              | 302.3            | 0.81            | 0.21                       | 600                              | 220                             | 8.3                | 86.2                 | 83.5               | 82.7                  |
| 32 | D <sub>6</sub>  | 2.53              | 305.1            | 0.79            | 0.29                       | 460                              | 286                             | 8.9                | 85.4                 | 84.3               | 83.5                  |

Table 2.1: Results from rarefaction measurements.  $P_{CT}$  and  $T_{CT}$  are the measured initial pressure and temperature in the charge tube.  $\Gamma$  is the fundamental derivative of gasdynamics as predicted by the reference equation of state for the measured thermodynamic conditions. The  $\Delta P_{wave}$  is the pressure difference measured across the rarefaction.  $A_{geom}$  is the nozzle area as derived from the geometry.  $A_{eff}$  is the effective nozzle area calculated using the measured pressure drop across the expansion.  $\Delta t$  is the process start-up time inferred from the mapped signal.  $c_{model}$  is the speed of sound estimated using the most accurate thermodynamic model for the measured conditions (uncertainty unknown).  $c_{fit}$  is the speed of sound as measured by fitting the experimental time-of-flight results using a linear function.  $c_{offset}$  is the speed of sound obtained by shifting the theoretical curve with the average deviation from the experimental results.

tube and charge tube had a period of approximately 2 hours with an amplitude of up to 3 °C for both temperature levels.

Pressure recordings of experiment 28 are displayed in figure 2.16. The process start-up time is determined by applying the same mapping procedure as illustrated in section 2.3.3, and is found to be between 5.6 and 9.0 ms in all experimental runs. The nozzle area was varied between 460 and 600 mm<sup>2</sup> based on the geometry. Calculations using the resulting pressure drop from the experiments result in a significantly lower nozzle area, see figure 2.1, which may indicate that there is accumulation of condensed fluid in the unheated FOV.

In order to verify that the measurements are coherent with the measured operating conditions, the speed of sound has been computed from the experimental data and compared with estimations obtained with the best available, though possibly still inaccurate, thermodynamic model for pure D<sub>6</sub> [50]. Using the estimated sound speed, the theoretical curve can be constructed in the same manner as for the other gases, except that the ideal gas model can not be used in this case, and consequently the Riemann invariant can not be integrated analytically. The local flow velocity is instead evaluated by integrating the Riemann invariant numerically. Results obtained from experiment 28 are displayed in figure 2.17. The experimental local wave propagation speed is evaluated using the time of flight method as described in section 2.3.2 for sensors PT1 / PT2. The measurements of sensors PT3 / PT4 are influenced by the reflection of the rarefaction from the CT end wall. The wave speed calculated from experimental data for this experiment is within 8 % of the value predicted by the thermodynamic model, except for a pressure drop lower than 12 mbar. This is possibly because the pressure gradient is still very low for that portion of the signal, making the influence of noise more significant. By fitting the experimental data in the same manner as illustrated for the case of incondensable gases, i.e. using a linear fit, and by adopting an offset of the theoretical curve, the speed of sound  $c_{\text{fit}}$  and  $c_{\text{offset}}$  respectively is obtained. The average error and standard deviation with respect to the value predicted by the thermodynamic model are 1.6 % ± 1.2 % for the linear fit and 1.6 % ± 1.1 % for the theoretical offset. The experimental results are surprisingly close to model predictions, given the fact that, differently from the case of incondensable gas, the D<sub>6</sub> thermodynamic model is expected to be rather inaccurate for states in the close proximity of the saturation curve.

With reference to the pressure recordings, the time difference between the small pressure drop that precedes the main pressure drop correlates with the duration from the instant the sliding cylinder moves away from the seal until full opening of the valve. Over time, several experiments had been performed in N<sub>2</sub>, CO<sub>2</sub>, He and air, bringing the total counting of experiments in incondensable gases to a large value. Suddenly, the aforementioned time difference increased dramatically from approximately 12 ms initially, to values above 100 ms. Lack of lubrication might be the cause of increased friction of the slider and determine this effect. As soon as the first shot in D<sub>6</sub> was performed, this time interval reduced immediately, confirming the hypothesis that either D<sub>6</sub> condenses in the FOV and lubricates the mechanical motion, or even that the dense vapour of D<sub>6</sub> acts as a lubricant.

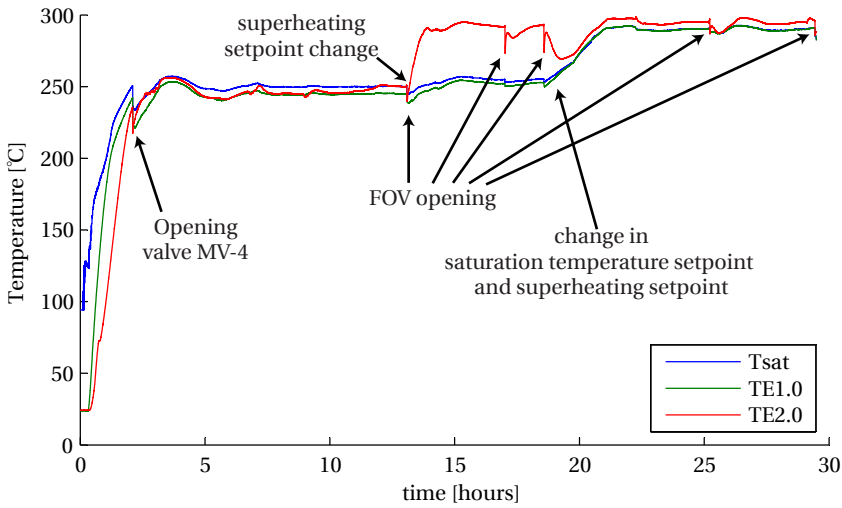


Figure 2.15: Temperature recordings during the experimental campaign on siloxane D<sub>6</sub>. Tsat is obtained from the measured pressure in the vapour generator by means of the suitable thermodynamic model from Nannan and Colonna [50]. TE1.0 is the temperature measured by the PT-100 sensor in the vapour generator. TE2.0 is the temperature measured by the PT-100 sensor in the reference tube.

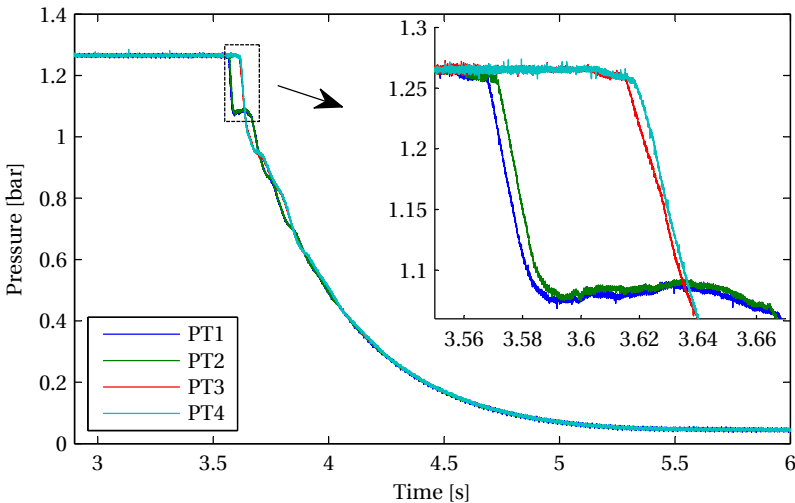


Figure 2.16: Pressure recordings during a D<sub>6</sub> experiment. The conditions in the CT are 1.27 bar and 298 °C. PT1 to PT4 are the pressure recordings of the sensor closest to the FOV to furthest away from the FOV, respectively.

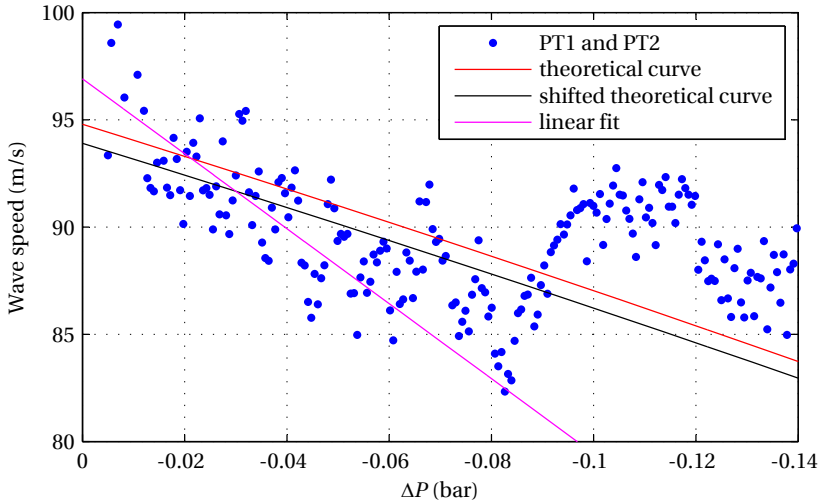


Figure 2.17: Wave speed in  $D_6$  siloxane as a function of the pressure drop. The blue dots are the experimental results obtained with the time-of-flight measurements. The red line is the theoretical curve as calculated by the thermodynamic model from Nannan and Colonna [50]. The black line is a fit of the experimental data using an offset of the theoretical curve. The magenta line is a linear fit of the data.

## 2.5. CONCLUSION & FUTURE WORK

A novel Ludwig-tube-type facility has been commissioned at Delft University of Technology. The purpose of the setup is to perform measurements on waves propagating in NICFD flows. The pressure and temperature of the working fluid can be regulated independently from each other, such that any thermodynamic state can be achieved within the limits of the measurement system of 21 bar and 400 °C. The leak rate of the facility has been characterised and it is predicted to have a maximum impact of 0.5 % on the speed of sound in the experiments, due to contamination by air. Tests of shock formation in air are performed in order to validate the functioning of the pressure measurement equipment. A procedure to estimate the system start-up time of the FOV has been devised and estimated values range from 2.5 ms to 9.0 ms. Preliminary experiments in the non-ideal regime of siloxane  $D_6$  have been successfully performed, providing values of the wave propagation speed that are within 8 % and speed of sound within 1.6 % of the predictions of a state-of-the-art thermodynamic model. Note however that estimates of the speed of sound calculated with this thermodynamic model are affected by a very large uncertainty, as the only direct comparison of the speed of sound were performed in the liquid phase and deviated approximately 30 % [49].

The objective of the next phase of the project is to perform experiments in the nonclassical BZT region. The process start-up time, dependent on the opening time of the FOV, is of crucial importance, since it determines the location within the tube where characteristics would coalesce and a shock would be formed. The estimation of the distance of the location where the shock is formed from the FOV has been reported by Colonna *et al.* [49] for  $D_6$ , whereby a process start-up time of 3.31 ms corresponds to a fully formed shock at 5 m from

the FOV (approximately half of the length of the CT). In order for the shock to be formed at the location of PT3, the requirement on the FOV opening time becomes 5.54 ms. Although this value is met in the experiments in incondensable gases, it is not met in the experiments in  $D_6$ , see Table 2.1. On the other hand, wave steepening should be visible in all nonclassical experiments. A sufficient proof of the existence of nonclassical gasdynamics would arguably be that the wave propagation speed increases at lower pressures in a rarefaction.





# 3

## GASDYNAMIC EXPERIMENTS IN THE PREDICTED BZT REGION OF SILOXANE D<sub>6</sub>

### 3.1. INTRODUCTION

Chapter 2 describes the FAST facility and its characterization. Also experiments in the ideal gas regime using a variety of gases are presented in that chapter together with some preliminary experiments in the non-ideal gas regime using siloxane D<sub>6</sub>. In these experiments, the value of  $\Gamma$ , as computed with the adopted thermodynamic model, reaches a minimum value of 0.8. The uncertainty in the thermodynamic model is rather large in the thermodynamic region of interest. For example, the uncertainty estimated for the speed of sound is at least 30 %. Since  $\Gamma$  is a derived thermodynamic quantity, which can not be measured directly, its prediction suffers from even larger uncertainties. This means that the BZT zone predicted by the model might not exist at all, might be much larger or smaller than predicted. The aim of the study presented in this chapter is to experimentally investigate flows featuring the fluid in a  $\Gamma < 0$  region, and possibly confirm the existence of nonclassical gasdynamic phenomena, such as rarefaction wave steepening and RSW.

The chapter is structured as follows: section 3.2 elaborates on the thermodynamic conditions during the heating, stabilisation and cooling phase of the experiment preparation procedure. Once the FOV opens, the gasdynamic experiment starts and the pressure is recorded at high frequency. These results are described in section 3.3. From the pressure signal in time, the wave speed is computed, which is also shown in this section. The hypothesis of the formation of rarefaction shocks in the flow is described in section 3.4. An estimation of the value of  $\Gamma$  from the wave speed measurements is described in section 3.5. Finally, conclusions and recommendations for further work are given in section 3.6.

### 3.2. THERMODYNAMIC CONDITIONS

The optimal thermodynamic conditions allowing to conclude that an RSW is generated in the FAST would be such that the shock propagates with its maximum achievable Mach number. Estimates of the wave propagation Mach number vary between 1.023 and 1.072, as determined by Guardone *et al.* [28] using three different equations of state, including the arguably most accurate multiparameter Span-Wagner equation of state, which is fitted to experimental data [49]. Even this complex thermodynamic model suffers from large uncertainties, specifically in the thermodynamic region of interest. In addition, the model is rigorously applicable to pure fluids, while the fluid utilized in the experiments is 96 % pure, and the influence of residual compounds on the value of thermodynamic properties is difficult to estimate. The average absolute deviation is found to be 0.25 % between experimental values of the vapour pressure and values estimated using the Span-Wagner model, limited to temperatures below 260°C [49]. Above that temperature, no experimental data is found in literature, and it is likely that the deviation is larger than the specified value. Values of the speed of sound calculated with the thermodynamic model suffer from larger uncertainties, as the only experimental value the model has been compared to is in the liquid state due to unavailability of reported experiments in the gas phase. This liquid-phase speed of sound features a deviation of 30 %.  $\Gamma$  is a derived quantity of the speed of sound, and the uncertainty on its prediction is thus very high. Therefore, the possibility exists that the calculated BZT region is much larger, much smaller, or does not exist at all in this fluid. Because the size of the BZT zone is predicted to be rather small in terms of temperature and pressure, and  $\Gamma$  to be highly variable in that region, a very fine control of the thermodynamic conditions of the fluid prior to opening the valve is required. The method to regulate the pressure and temperature in the CT independently of each other is explained in detail in section 2.2.2, together with the control strategy. Because of the large uncertainties of the thermodynamic model, the saturation temperature is measured in situ by a Pt-100 in the vapour generator. Instead of regulating the temperature in the RT, the amount of superheating is regulated. This has the advantage of being independent of the thermodynamic model. A total of five experiments are conducted inside, or close to the predicted BZT region. The thermodynamic conditions of the performed experiments are chosen to be at several pressure levels in or close to the predicted BZT zone, and as close to the coexistence curve as technically possible, where the lowest values of  $\Gamma$  are predicted. The measured values of pressure and temperature are shown in table 3.1. Experiments 1 and 4 have been reiterated in order to assess the repeatability of the experiment. The reported values of  $\Gamma$  and speed of sound are predicted using the thermodynamic model with the recorded pressure and charge tube temperature. The heating process is displayed for each experiment in figure 3.1 to 3.5 respectively.  $T_{\text{sat}}$  refers to the saturation temperature, as calculated using the thermodynamic model from the measured pressure. TE1.0 refers to the temperature measured in the vapour generator, and TE2.0 to the temperature measured in the reference tube. At a saturation temperature of approximately 250 °C, valve MV-4 (see figure 2.2) to the CT is opened, which causes flashing of part of the liquid in the vapour generator. The CT is kept at a higher temperature than the vapour generator at all times to avoid condensation after the flashing of the liquid, see figures 3.1 to 3.5.

Since both the temperature and pressure in the vapour generator are measured indepen-

| no | $P_{\text{HFT}}$<br>[bar] | $T_{\text{HFT}}$<br>[bar] | $T_{\text{CT}}$<br>[°C] | $\Delta T_{\text{sup}}$<br>[°C] | $\Gamma$<br>[-] | $c$<br>[m/s] |
|----|---------------------------|---------------------------|-------------------------|---------------------------------|-----------------|--------------|
| 1  | 8.40                      | 365.6                     | 367.6                   | 2.00                            | 0.132           | 51.2         |
| 2  | 8.47                      | 365.4                     | 367.5                   | 1.95                            | 0.086           | 49.7         |
| 3  | 8.56                      | 367.3                     | 367.8                   | 0.51                            | 0.057           | 48.6         |
| 4  | 8.79                      | 368.0                     | 368.8                   | 0.84                            | -0.019          | 45.5         |
| 5  | 8.80                      | 368.3                     | 369.0                   | 0.66                            | -0.012          | 45.7         |

Table 3.1: Thermodynamic conditions of the initial states.  $P_{\text{HFT}}$  and  $T_{\text{HFT}}$  correspond to the measured pressure and temperature respectively in the vapour generator.  $T_{\text{CT}}$  is the measured temperature in the end of the charge tube. The difference between the temperature in the charge tube and vapour generator is the superheating defined as  $\Delta T_{\text{sup}}$ . The fundamental derivative  $\Gamma$  and speed of sound  $c$  are calculated using the thermodynamic model evaluated at  $P_{\text{HFT}}$  and  $T_{\text{CT}}$ .

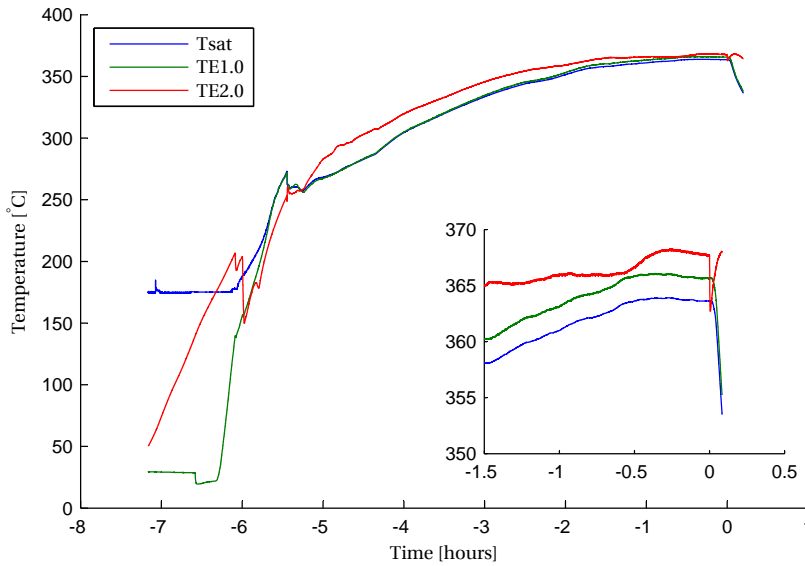


Figure 3.1: Temperature recordings from experiment 1.  $T_{\text{sat}}$  is the saturation temperature, which is calculated using the thermodynamic model from the pressure in the vapour generator. TE1.0 is the measured temperature in the vapour generator. TE2.0 is the measured temperature in the reference tube.

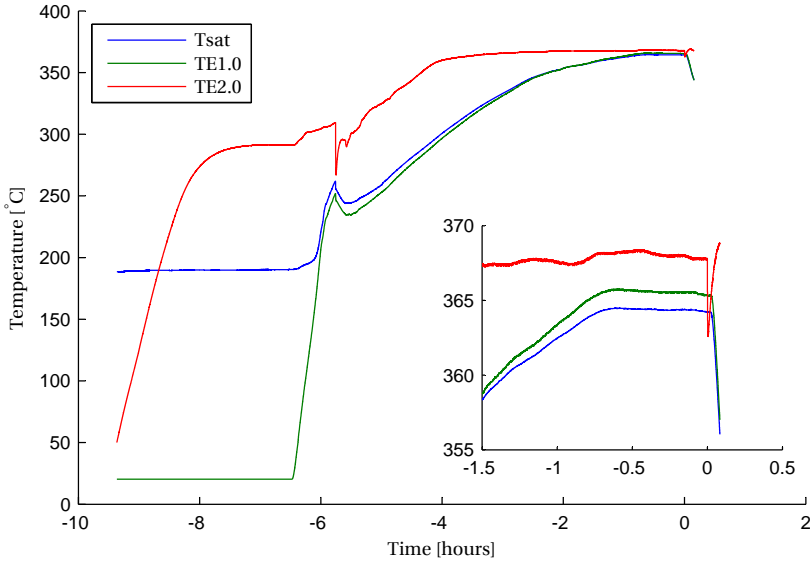


Figure 3.2: Temperature recordings from experiment 2.  $T_{\text{sat}}$  is the saturation temperature, which is calculated using the thermodynamic model from the pressure in the vapour generator. TE1.0 is the measured temperature in the vapour generator. TE2.0 is the measured temperature in the reference tube.

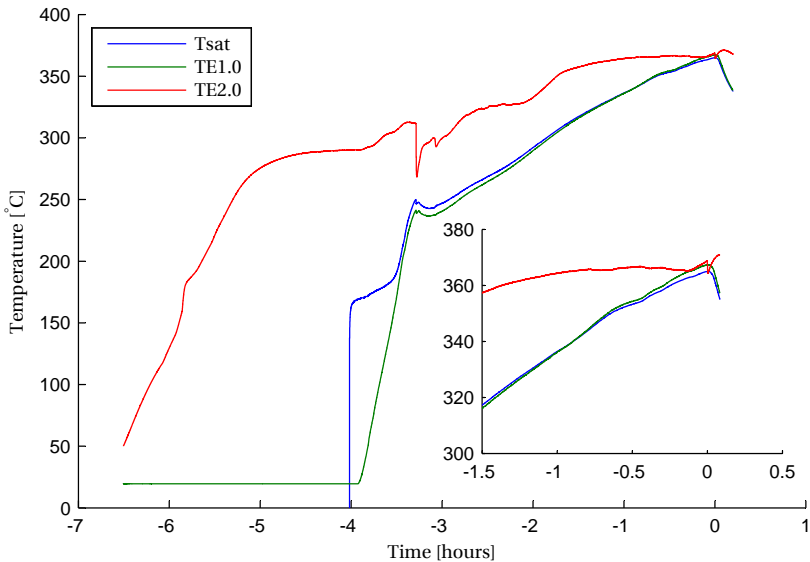


Figure 3.3: Temperature recordings from experiment 3.  $T_{\text{sat}}$  is the saturation temperature, which is calculated using the thermodynamic model from the pressure in the vapour generator. TE1.0 is the measured temperature in the vapour generator. TE2.0 is the measured temperature in the reference tube.

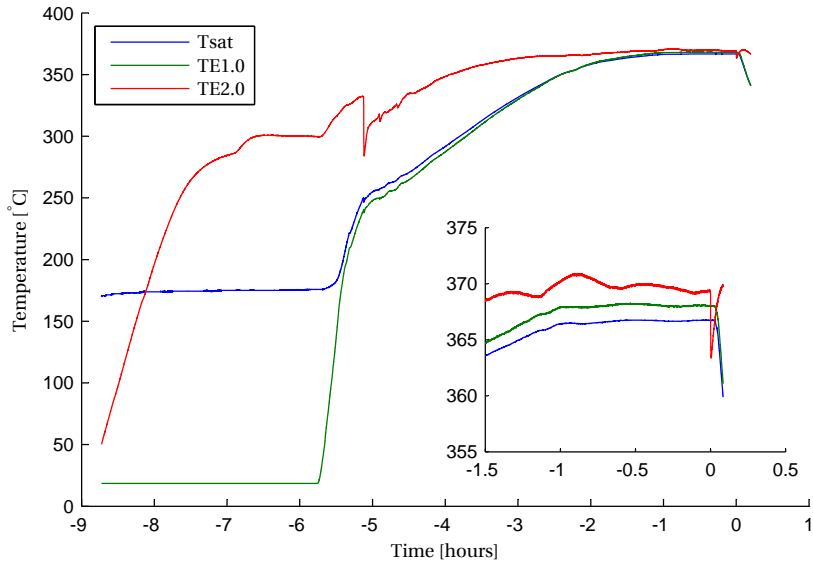


Figure 3.4: Temperature recordings from experiment 4.  $T_{sat}$  is the saturation temperature, which is calculated using the thermodynamic model from the pressure in the vapour generator. TE1.0 is the measured temperature in the vapour generator. TE2.0 is the measured temperature in the reference tube.

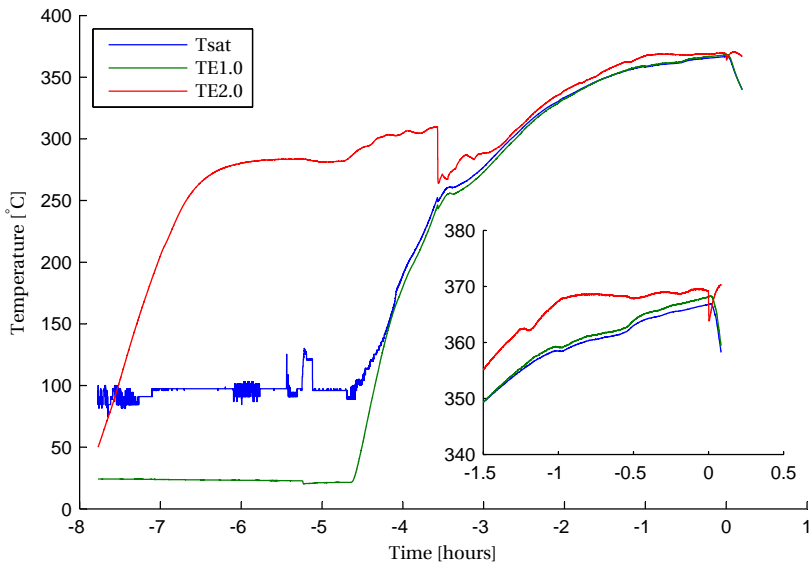


Figure 3.5: Temperature recordings from experiment 5.  $T_{sat}$  is the saturation temperature, which is calculated using the thermodynamic model from the pressure in the vapour generator. TE1.0 is the measured temperature in the vapour generator. TE2.0 is the measured temperature in the reference tube.

3

dently during the entire heating phase, it is possible to obtain the saturation curve from the recording of their values, see figure 3.6. A detail of the saturation curve above 250 °C is given in figure 3.7. At subatmospheric pressures, the pressure transducer cannot provide an accurate value of pressure and consequently the calculated saturation temperature is only accurate above a temperature of approximately 250 °C. The sufficient vacuum level of the facility has been confirmed with a temporarily installed Pirani vacuum gauge. Furthermore, during heating at low pressure, the heat transfer coefficient from the wall to the fluid is much lower than at higher pressure. This gives rise to large temperature gradients in the vapour generator. For example, the temperature difference between the fluid and the wall of the lower section of the vapour generator, where most of the thermal energy is supplied, could become as large as 150 °C, depending on the amount of supplied power. Moreover, it is observed that the fluid mixing is still limited at this temperature. This is displayed during heating of the vapour generator in the following way. The measured pressure increase is higher than expected based on the measured temperature increase. When heating stopped during this phase, the measured pressure rapidly dropped to match the expected increase of saturation pressure. Thus the fluid temperature close to the wall is likely to be higher than the value measured with the Pt-100. However, the risk of thermal decomposition is limited because the temperature is still low. Above a fluid temperature of 250 °C, the temperature difference between the fluid and the wall of the bottom section of the vapour generator, where the main heater is located, is below 40 °C, indicating a higher heat transfer coefficient. The other wall sections of the vapour generator are kept at a temperature within 8 °C from the fluid temperature.

The difference of the predicted saturation temperature with the measured one is displayed in figure 3.9 for the heating phase up to the opening of the FOV and in figure 3.10 for the cooling phase after the FOV had been opened. The spike during the heating phase of experiment 1 at 270°C is caused by the opening of valve MV-4. Part of the liquid in the vapour generator is flashed and an almost instantaneous change in thermodynamic state is presented. For a few seconds, the value does not comply with the predicted saturation curve, due to the finite response time of the instruments. During the other experiments, the opening of valve MV-4 is performed at a lower saturation temperature level of approximately 250°C, thus not visible in these figures.

The maximum difference with respect to model predictions is 8 °C for the heating phase, and up to 3 °C during the cooling phase. At low pressures, a possible cause for the deviation is the inaccuracy of the pressure sensor, leading to a relatively high deviation in saturation temperature. Above 7.5 bar, the measured temperature is always above the model-predicted saturation temperature. At high pressures, a possible cause for the difference is the occurrence of stratification during the cooling phase. The convective motion induced by the boiling prevents stratification in the fluid during the heating phase to occur. Another explanation is that the temperature measurements of the Pt-100s may be affected by radiative heat transfer from the wall to the sensor. The temperature of the sensor is determined by the convective, conductive and radiative heat transfer. The conductive heat transfer is negligible due to the long insertion length of the Pt-100. The temperature of the wall in the heating phase differs from the cooling phase. Also the recorded fluid temperature in the heating phase is higher

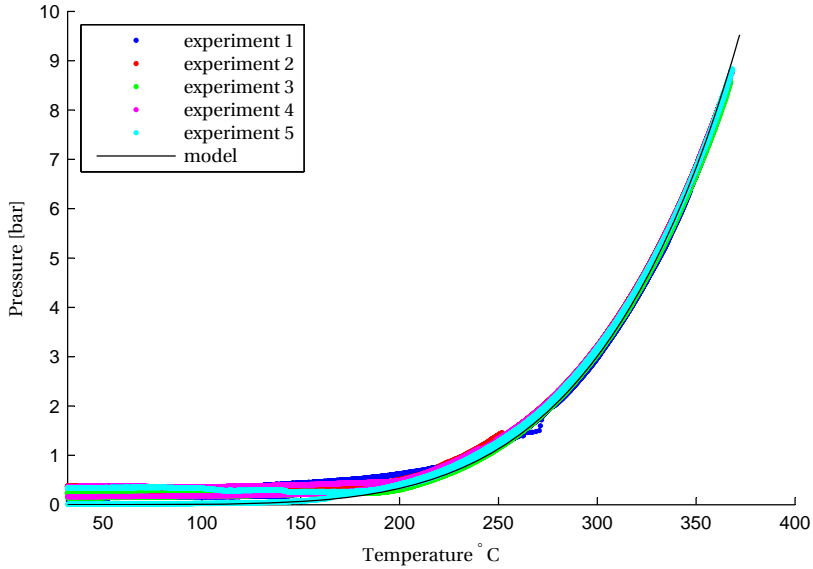


Figure 3.6: Pressure - temperature diagram of the recorded thermodynamic conditions in the vapour generator.

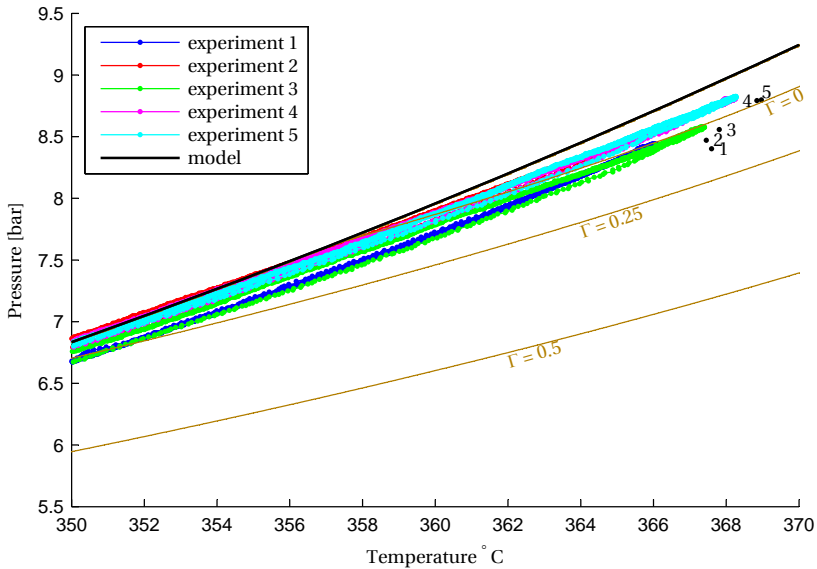


Figure 3.7: Close-up of the pressure-temperature diagram of the recorded thermodynamic conditions in the vapour generator. The thermodynamic quantities of the experiments are also displayed.



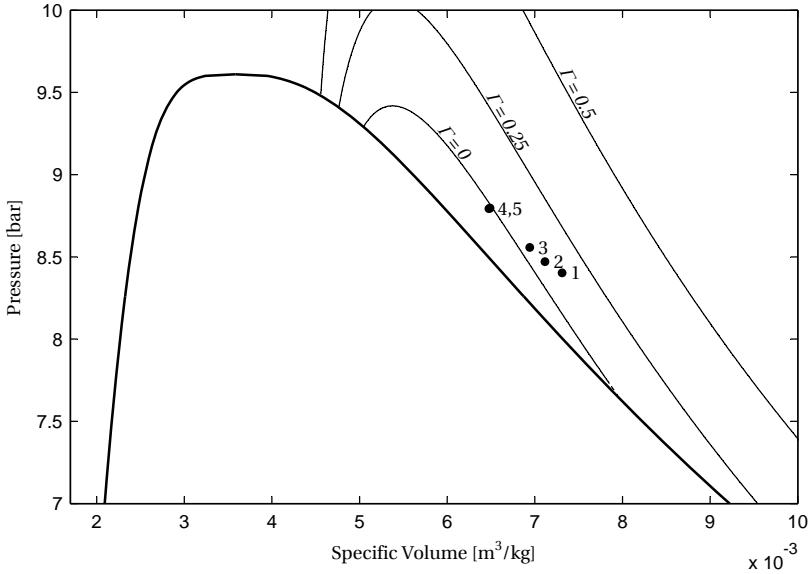


Figure 3.8: Pressure - specific volume diagram of the BZT zone. Iso- $\Gamma$  lines are indicated to show the predicted BZT zone. Numbers 1 to 5 correspond to the experimental thermodynamic conditions of experiment 1 to 5 in table 3.1 as measured with the pressure transducer and the Pt-100 in the CT.

than in the cooling phase at the same pressure. This indicates that radiative heat transfer from the wall to the Pt-100 is not negligible, despite it being immersed in boiling liquid.

The wall temperature of the vapour generator is regulated to keep its temperature close to the fluid temperature, see figure 3.11 and 3.12. This limits the measurement error due to the radiative heat transfer. The temperature of the mid-section of the vapour generator has the largest influence on the measured Pt-100 temperature, because of its proximity. However, in order to keep pressure and temperature constant at the desired thermodynamic state, sufficient thermal energy need to be supplied to the fluid to compensate for the heat losses. It was necessary to set the wall temperature of the mid-section of the vapour generator approximately 5 °C above the fluid temperature in all experiments at the desired thermodynamic state. Consequently, it can occur that the Pt-100 overestimates the temperature of the fluid, which could be as high as several degrees.

The thermodynamic conditions of the initial state of the measurements are displayed in a pressure-temperature diagram in figure 3.7, in a pressure - specific volume plane in figure 3.8 and in a temperature - entropy plane in figure 3.13. In these diagrams also contours of the predicted values of  $\Gamma$  are shown. The specific volume and entropy are calculated using the thermodynamic model with the measured pressure in the vapour generator and the measured temperature in the charge tube as input variables. It is apparent that the measurement conditions are at most only marginally within the model-predicted BZT zone. On

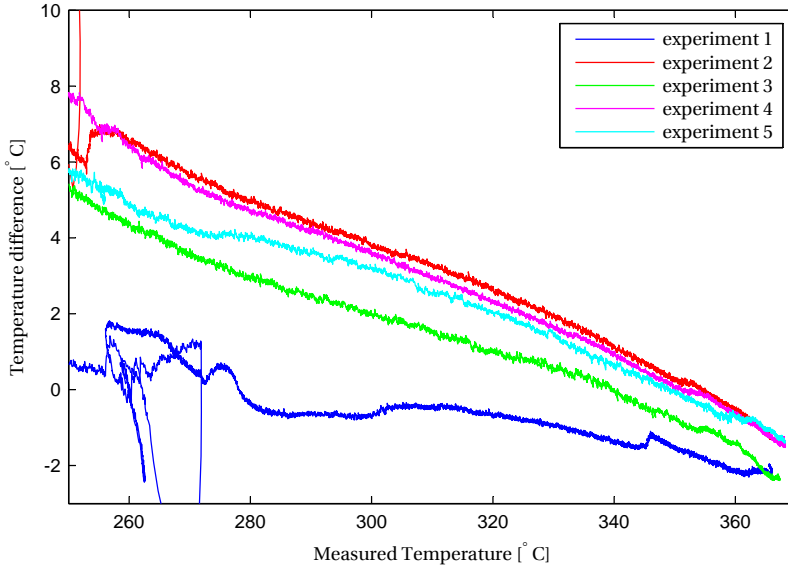


Figure 3.9: Temperature difference of the predicted saturation temperature and the measured saturation temperature during the heating phase up to the opening of the FOV. The large offset in experiment 1 is due to opening of valve MV-4. Part of the liquid is flashed and transported to the CT. This has a for a short time, a non-equilibrium effect, after which the temperature quickly corresponds to the saturation temperature again.

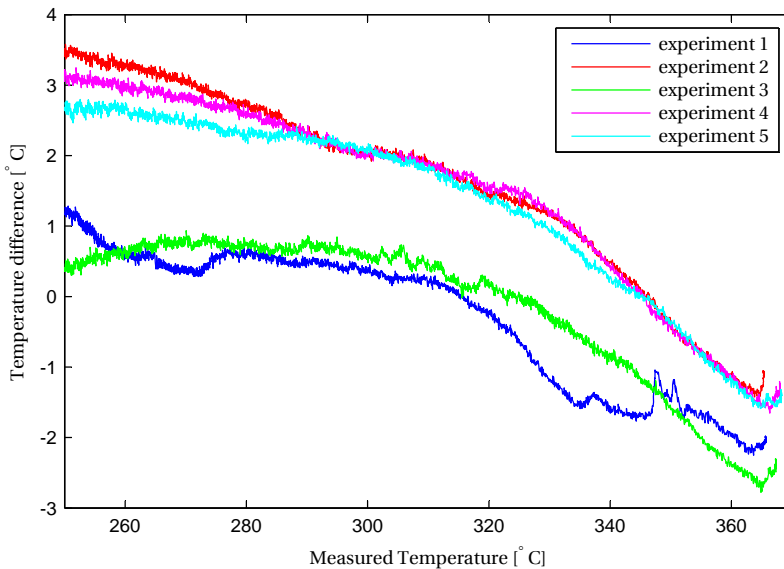


Figure 3.10: Temperature difference of the predicted saturation temperature and the measured saturation temperature during the cooling phase up after opening of the FOV.

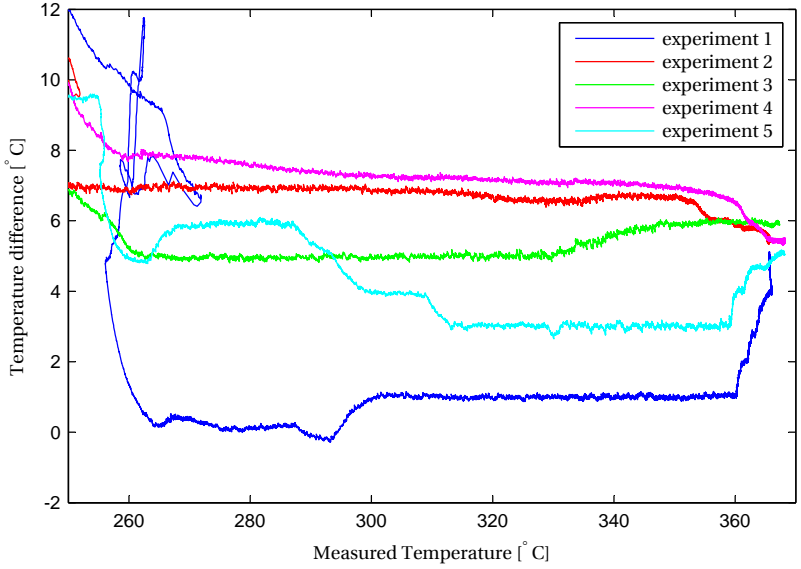


Figure 3.11: Temperature offset between the thermocouple at the mid-section of the vapour generator and the Pt-100 immersed in the fluid during the heating phase.

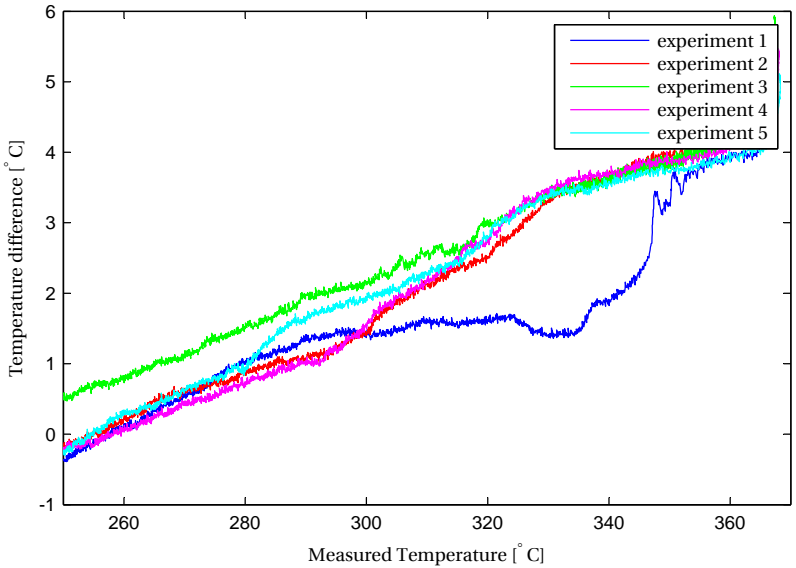


Figure 3.12: Temperature offset between the thermocouple at the mid-section of the vapour generator and the Pt-100 immersed in the fluid during the cooling phase.

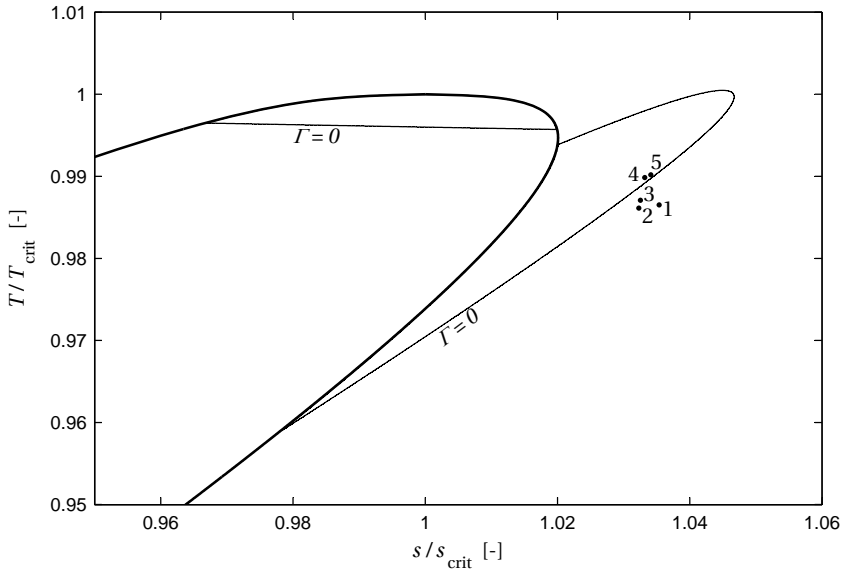


Figure 3.13: Close-up of the temperature - entropy diagram of the predicted BZT zone and critical region of  $D_6$ . The measurement point of each experiment is indicated in the diagram. The entropy of these points is calculated using the thermodynamic model with the pressure in the vapour generator and temperature in the charge tube as input variables.

the other hand, the measured saturation line deviates from the model prediction, featuring lower saturation pressures above approximately 355 °C. This can have many causes, e.g. the thermal equilibrium in the vapour generator, the composition of the fluid, or model inaccuracy at these temperatures. The measured superheating is limited, down to 0.5 °C. A lower superheating could indicate a lower value of  $\Gamma$ . Moreover, given that  $\Gamma$  is a quantity derived from the speed of sound, the value of  $\Gamma$  can be very different from that predicted by the thermodynamic model, since the prediction of the speed of sound already features a high uncertainty. The fluid is not expected to condense during an experiment, because  $D_6$  is a highly retrograde fluid, see figure 3.13 and figure 3.14.

### 3.3. WAVE SPEED MEASUREMENTS

The pressure recordings from the experiments are displayed in figures 3.16, 3.18, 3.20, 3.22 and 3.24. The rarefaction wave is reflected at the end of the pipe, and creates a non-simple region, see figure 3.15. Measurements of waves in the non-simple region are not useful, because of inherent limitations in the adopted wave speed measurement procedure. The time instant  $t^*$  at which the first disturbance reaches the end of the tube is taken as an estimate of the start of the non-simple region. Time instant  $t^*$  is predicted using the experimental value of the speed of sound, and indicated in the figures by the dashed line. The first disturbance is defined as a deviation of 15 mbar from the initial pressure. Because pressure sensor PT4 is very close to the end of the tube, only a very small portion of that signal is useful.

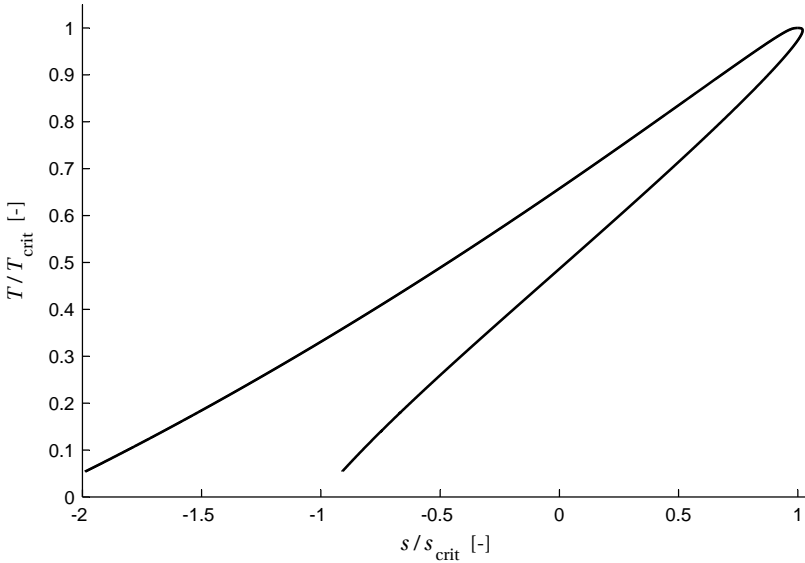


Figure 3.14: Temperature - entropy diagram of  $D_6$  showing the saturation line. Due to the high molecular complexity of the fluid, the fluid is highly retrograde. Condensation during the experiments is not expected to occur, because an isentropic expansion in the vapour phase will lead to a dryer state of the fluid.

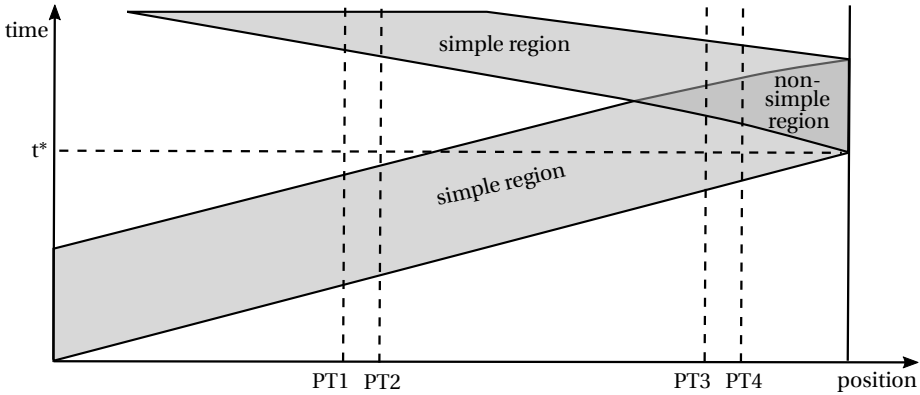


Figure 3.15: Schematic position - time diagram of an experiment in which no RSW occurs. In regions coloured in white, the flow variables are constant. Within simple regions, one Riemann invariant is constant.

It is noted that in each of the pressure recordings, a kink in the signal is visible at values of the pressure that are approximately 0.4 bar lower than the pressure at the start of the experiment. This is a remarkable difference if compared to the experiments described in Sec. 2.4, which took place with the fluid at thermodynamic conditions that were far from those of the predicted BZT region. A similar feature has only been observed in the compression shock-wave experiments in  $N_2$ , see figure 2.8. The presence of this kink in rarefaction experiments could possibly indicate the formation of a shock wave, thus the presence of nonclassical gas-dynamic features in the flow. This is described in a more detail in section 3.4.

Using the time-of-flight method as described in section 2.3.2, the wave propagation speed is determined for all the experiments as a function of the pressure decrease, and is displayed in figures 3.17, 3.19, 3.21, 3.23 and 3.25. The 50 mm elongation of the facility due to thermal expansion results in a larger distance between the sensors, which has been taken into account in the evaluation of the wave speed. The time-of-flight technique is applied to the signals of sensor pair PT1 and PT2, sensor pair PT3 and PT4, and using the signals of sensor PT1 and PT3. The latter two sensors span a much larger section of the tube. Because the estimation gives the average wave speed between the two sensors, the result is an average wave speed through approximately half of the tube. In case the thermodynamic conditions are uniform, the flow field is homentropic and the local wave speed is solely depending on the local pressure. In the wave speed diagrams, also the theoretical curve for an isentropic shock-free flow is reported. For the region in which the fluid thermodynamic states are within the BZT zone, the local wave speed is expected to increase across the rarefaction.  $\Gamma$  is predicted to be negative in experiment 4 and 5, so the observation of an increase of the average wave propagation speed is expected in these experiments, according to the thermodynamic model. This is limited to a velocity increase of only 0.2 m/s. Such small wave speed increase is very difficult to detect given the noise affecting the signals of the measurements. However, the thermodynamic model is known to suffer from inaccuracies, such that a lower value of  $\Gamma$  than predicted may occur.

The kink or plateau in the pressure diagram, displayed in figures 3.16, 3.18, 3.20, 3.22 and 3.24, typically occurs at a slightly different pressure level in the considered signals of each respective experiment. As the wave propagates through the tube, the kink is present at an increasing pressure level, except for experiment 3, resulting in a non-physical jump in wave propagation speed around that pressure. Consequently the wave speed displays a much lower value around this pressure for all experiments except for that experiment. In experiment 3, a clear plateau is visible in the signal from sensor PT1, but the signal from sensor PT2 shows a much smoother signal. A possible explanation is that in that experiment, there were temperature gradients present in the shock tube, due to the fact that the experiment was performed immediately after the desired thermodynamic state in the tube was reached, see figure 3.3. Allowing for a settling time would have been better, but uncertainty with respect to the integrity of the sealing of the FOV determined this decision.

The speed of sound is obtained for all experiments by using a linear extrapolation to  $\Delta P \rightarrow 0$ , using the same algorithm as described in section 2.3.3. The resulting values are given in table

| no | $P_{\text{HFT}}$<br>[bar] | $T_{\text{CT}}$<br>[°C] | $c_{\text{model}}$<br>[m/s] | $c_{\text{exp12}}$<br>[m/s] | $c_{\text{exp34}}$<br>[m/s] | $c_{\text{exp13}}$<br>[m/s] |
|----|---------------------------|-------------------------|-----------------------------|-----------------------------|-----------------------------|-----------------------------|
| 1  | 8.40                      | 367.6                   | 51.2                        | 55.9                        | 54.5                        | 56.0                        |
| 2  | 8.47                      | 367.5                   | 49.7                        | 57.2                        | 56.6                        | 55.4                        |
| 3  | 8.56                      | 367.8                   | 48.6                        | 52.0                        | 48.3                        | 49.7                        |
| 4  | 8.79                      | 368.8                   | 45.5                        | 52.6                        | 50.6                        | 51.8                        |
| 5  | 8.80                      | 369.0                   | 45.7                        | 54.3                        | 50.8                        | 52.2                        |

Table 3.2: Experimental values of the speed of sound for the BZT experiments. The speed of sound given by the thermodynamic model corresponds to  $c_{\text{model}}$ . The experimentally determined speed of sound is given by  $c_{\text{exp12}}$ ,  $c_{\text{exp34}}$  and  $c_{\text{exp13}}$  using sensor PT1 and PT2, PT3 and PT4 and PT1 and PT3 respectively.

3

3.2. Three observations can be made from these results in case experiment 3 is not considered. The first is that the measured speed of sound is approximately 5 m/s higher than the value predicted by the multiparameter equation of state model. Furthermore, the speed of sound measured at sensor pair PT3/PT4 is always lower than at sensor pair PT1/PT2. This may suggest that a temperature gradient has established in the shock tube, featuring lower temperatures at the end of the tube. The third observation is the large variation in the speed of sound with relatively small variations in pressure and temperature. This clearly shows that the measurements have been performed in the NICFD region. Given the lower value of the speed of sound at higher values of the pressure and temperature, it is likely that the value of  $\Gamma$ , associated with the thermodynamic states pertaining these measurements, is smaller than 1. From these measurements, no negative value of  $\Gamma$  can be directly inferred. If no RSW has formed, the value of the wave propagation speed would increase in such an expansion, and in case an RSW has formed, the wave speed would be constant over the pressure difference across the shock. All measurements show a decrease in wave speed, which is coherent with non-ideal classical compressible fluid dynamics theory. Experiment 4 and 5 also show certain sections of the flow exhibiting a constant wave propagation speed, which may indicate the formation of an RSW, as further discussed in Section 3.4. In experiment 3, the wave speed after the plateau rises to very high values due to the deviating signal of sensor PT2. Such an increase of wave propagation speed can not be explained by nonclassical gasdynamic effects. It may occur due to the likely non-uniform distribution of the temperature around the sensor, due to the fact that the metal parts of the tube were not allowed to reach thermal equilibrium after the thermodynamic state of the fluid was reached.

### 3.4. SHOCK FORMATION?

In experiment 4, for  $\Delta P$  between -0.5 and -0.7 bar, and between -0.8 and -1.0 bar, a near constant wave speed is observed, see figure 3.23. In experiment 5, a near constant wave speed is measured between -0.4 and -0.8 bar, see figure 3.25. Despite the possibility that such response is induced by the opening of the FOV, it would be consistent with the formation of a double-sonic RSW in these experiments. The flow field would feature a rarefaction starting in the positive- $\Gamma$  domain, through the negative- $\Gamma$  domain back into a positive- $\Gamma$  domain, which corresponds to the isentropic expansion from point 1 to point 6 displayed in a  $P$ - $v$ -diagram in figure 1.8. A schematic representation of the wave propagation speed

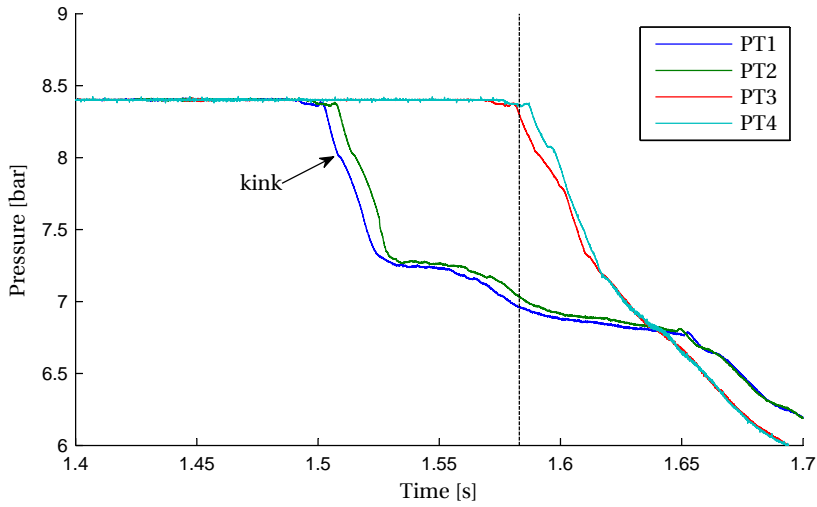


Figure 3.16: Pressure recordings from experiment 1. PT1 corresponds to the pressure transducer closest to the FOV and PT4 to the one furthest away. The time instance that the first disturbance reaches the end of the tube is indicated with the dashed line.

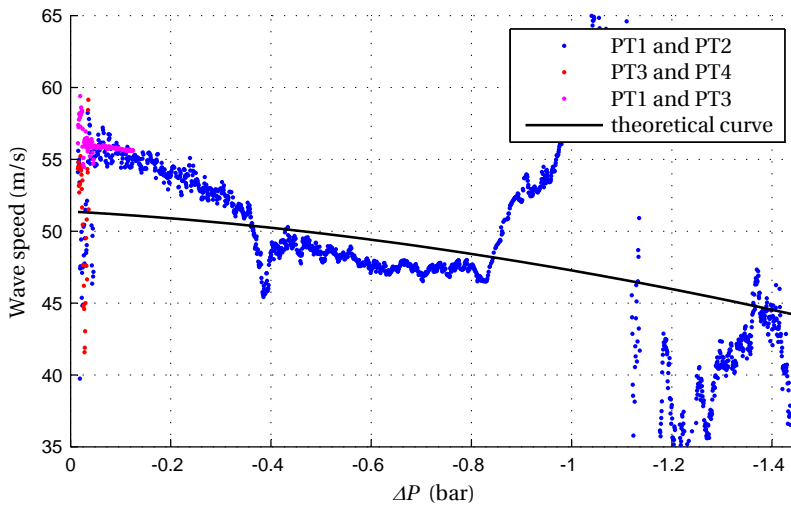


Figure 3.17: Wave speed measurements from experiment 1. Each dot corresponds to a pressure interval of approximately 0.64 mbar, or two times the resolution of the pressure transducer. For the blue dots, the time-of-flight technique is applied to sensor pair PT1 and PT2. For the red dots, sensor pair PT3 and PT4, and for the magenta dots, sensors PT1 and PT3. The black line represents the theoretical isentropic wave speed, as calculated with the thermodynamic model [49] in case of a shock-free flow.



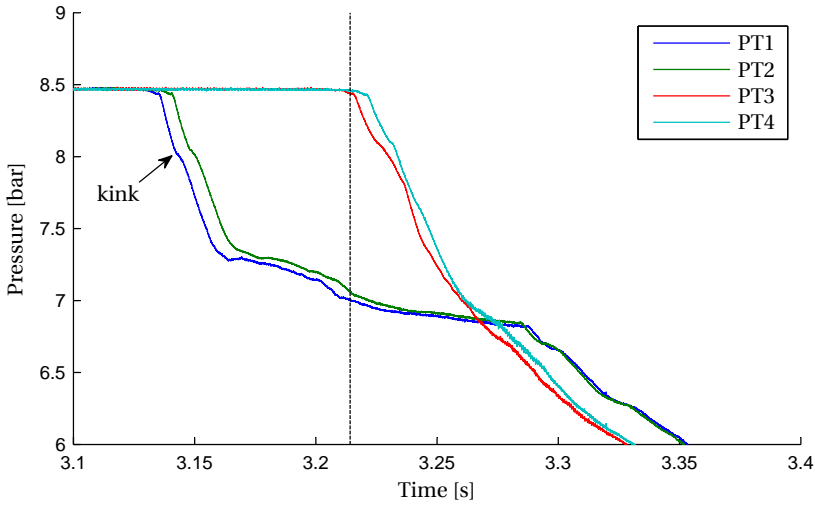


Figure 3.18: Pressure recordings from experiment 2. PT1 corresponds to the pressure transducer closest to the FOV and PT4 to the one furthest away. The time instance that the first disturbance reaches the end of the tube is indicated with the dashed line.

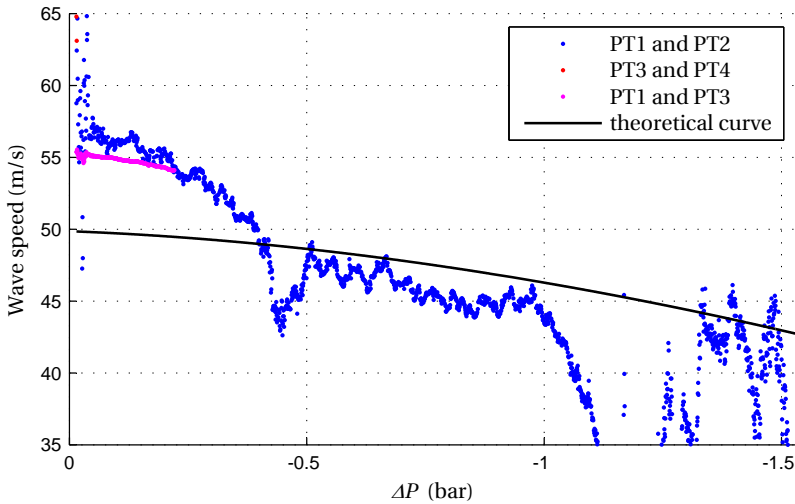


Figure 3.19: Wave speed measurements from experiment 2. Each dot corresponds to a pressure interval of approximately 0.64 mbar, or two times the resolution of the pressure transducer. For the blue dots, the time-of-flight technique is applied to sensor pair PT1 and PT2. For the red dots, sensor pair PT3 and PT4, and for the magenta dots, sensors PT1 and PT3. The black line represents the theoretical isentropic wave speed, as calculated with the thermodynamic model [49] in case of a shock-free flow.

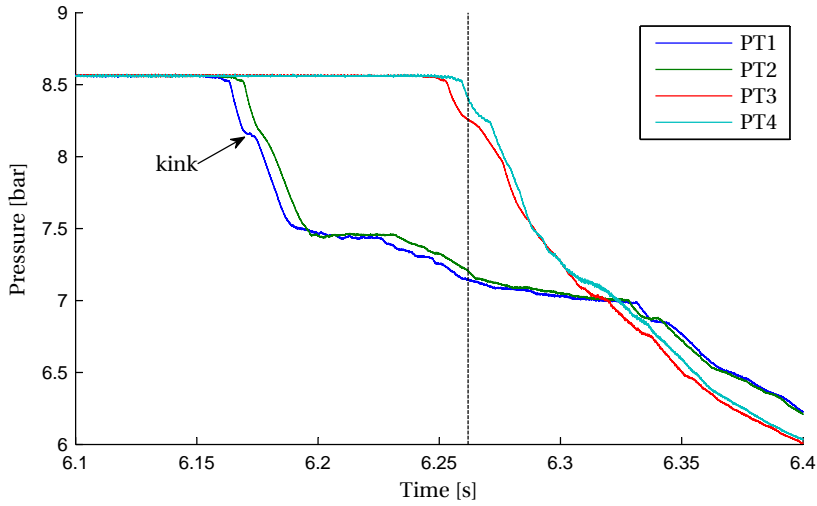


Figure 3.20: Pressure recordings from experiment 3. PT1 corresponds to the pressure transducer closest to the FOV and PT4 to the one furthest away. The time instance that the first disturbance reaches the end of the tube is indicated with the dashed line.

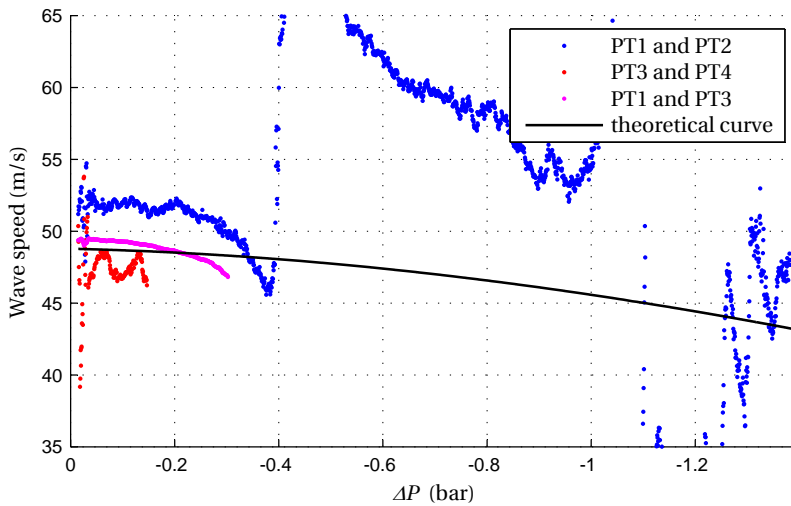


Figure 3.21: Wave speed measurements from experiment 3. Each dot corresponds to a pressure interval of approximately 0.64 mbar, or two times the resolution of the pressure transducer. For the blue dots, the time-of-flight technique is applied to sensor pair PT1 and PT2. For the red dots, sensor pair PT3 and PT4, and for the magenta dots, sensors PT1 and PT3. The black line represents the theoretical isentropic wave speed, as calculated with the thermodynamic model [49] in case of a shock-free flow.

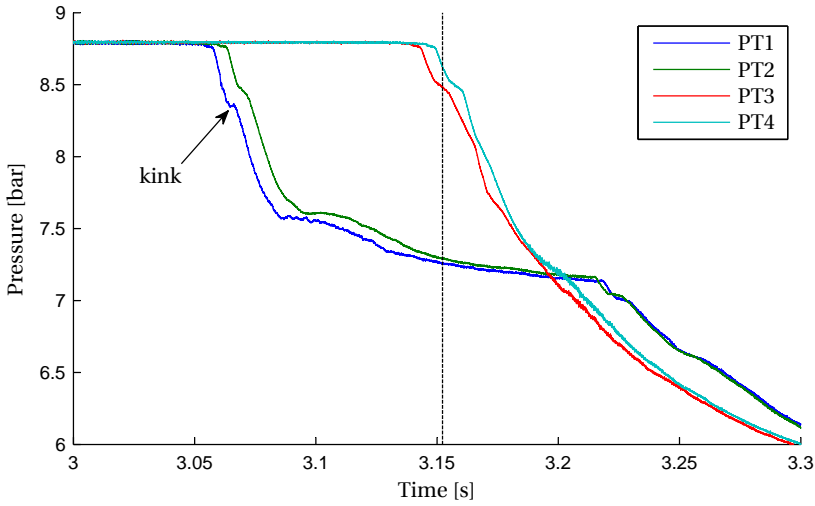


Figure 3.22: Pressure recordings from experiment 4. PT1 corresponds to the pressure transducer closest to the FOV and PT4 to the one furthest away. The time instance that the first disturbance reaches the end of the tube is indicated with the dashed line.

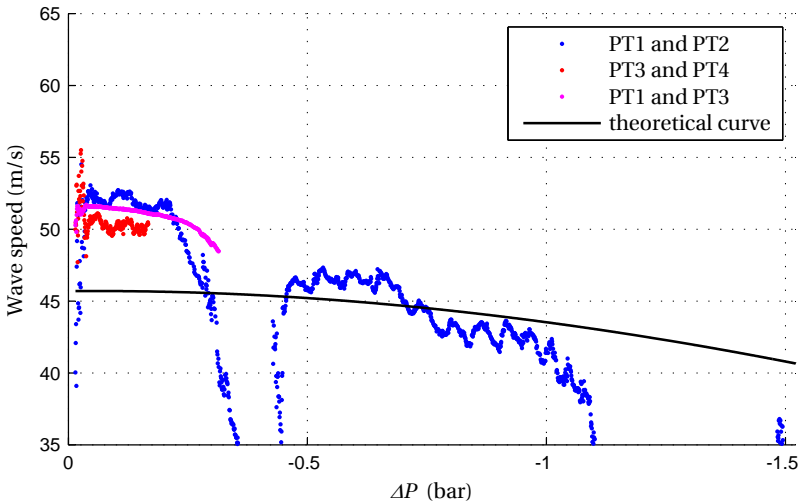


Figure 3.23: Wave speed measurements from experiment 4. Each dot corresponds to a pressure interval of approximately 0.64 mbar, or two times the resolution of the pressure transducer. For the blue dots, the time-of-flight technique is applied to sensor pair PT1 and PT2. For the red dots, sensor pair PT3 and PT4, and for the magenta dots, sensors PT1 and PT3. The black line represents the theoretical isentropic wave speed, as calculated with the thermodynamic model [49] in case of a shock-free flow.

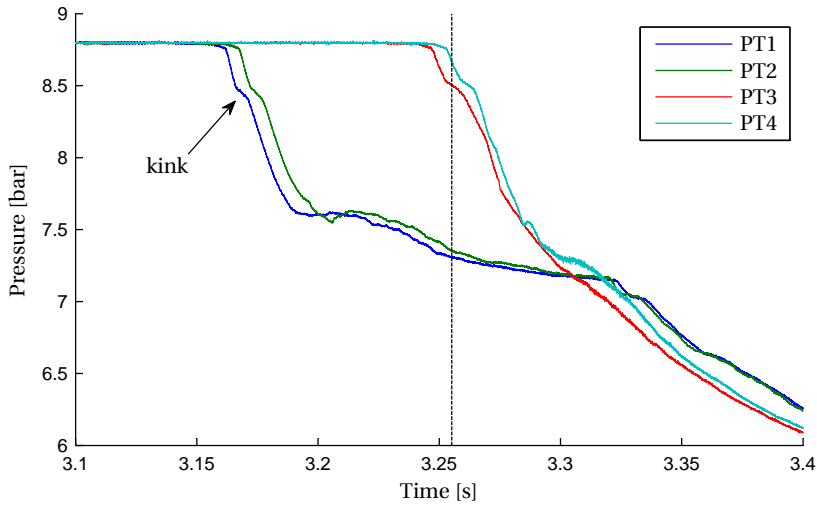


Figure 3.24: Pressure recordings from experiment 5. PT1 corresponds to the pressure transducer closest to the FOV and PT4 to the one furthest away. The time instance that the first disturbance reaches the end of the tube is indicated with the dashed line.

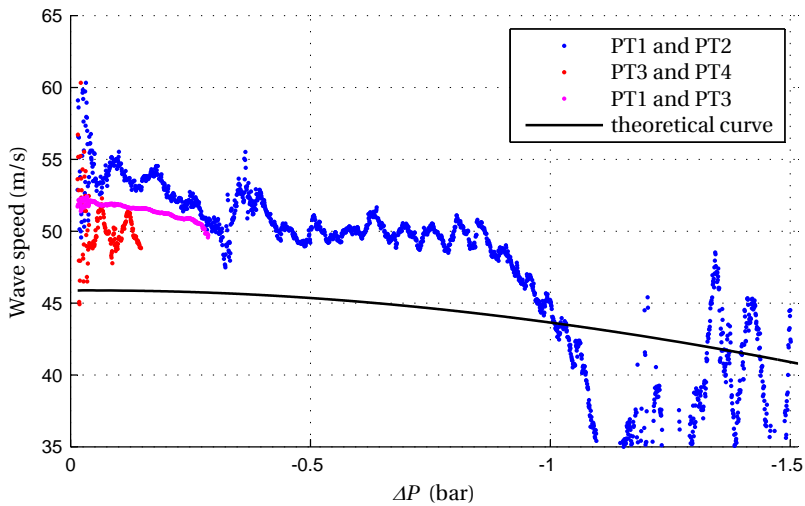


Figure 3.25: Wave speed measurements from experiment 5. Each dot corresponds to a pressure interval of approximately 0.64 mbar, or two times the resolution of the pressure transducer. For the blue dots, the time-of-flight technique is applied to sensor pair PT1 and PT2. For the red dots, sensor pair PT3 and PT4, and for the magenta dots, sensors PT1 and PT3. The black line represents the theoretical isentropic wave speed, as calculated with the thermodynamic model [49] in case of a shock-free flow.

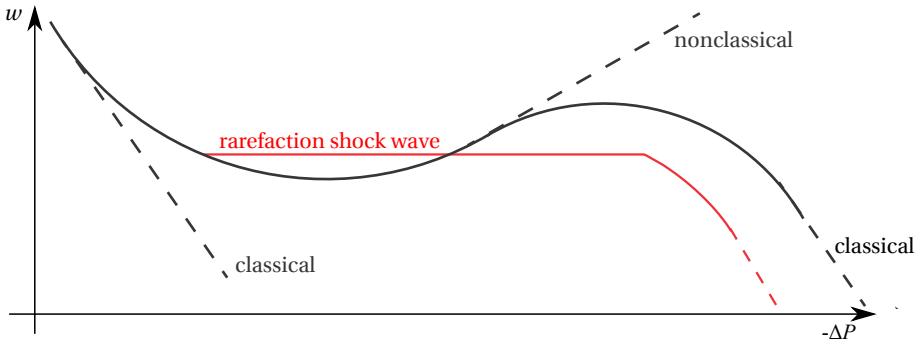


Figure 3.26: Schematic representation of an unsteady rarefaction through a region of negative  $\Gamma$ . Note that the x-axis displays the negative pressure difference, i.e. the pressure drop. The rarefaction initially takes place in the classical positive- $\Gamma$  regime, such that  $dw/dp$  is positive, i.e. the wave speed decreases in an expansion. As soon as the rarefaction enters the negative- $\Gamma$  region,  $dw/dp$  is negative, so the wave speed increases, in case the expansion is of the shock-free isentropic type. In case an RSW is formed, the wave speed is constant over the pressure drop of the RSW, since the shock moves at constant speed. In this example, a double-sonic rarefaction shock wave is displayed in red. The final part of the rarefaction takes place again in the positive- $\Gamma$  region, such that  $dw/dp$  is positive, and the wave speed decreases.

as a function of the pressure drop is given in figure 3.26. Two cases are displayed: a case with a fully isentropic, thus shockless, flow field, and a case in which a double-sonic shock is formed. For a fully isentropic expansion, i.e. without formation of shocks, the wave propagation speed decreases in the regions in which  $\Gamma$  is positive and increases in the region in which  $\Gamma$  is negative. For the case with a double sonic RSW, the shock is developed such that the shock propagation speed is equal to the sonic wave propagation speed of both the pre- and post-shock conditions, so no jump in wave speed is visible. The latter case would be consistent with observations in experiment 4 and 5.

It is difficult to prove the occurrence of a double-sonic RSW by a constant wave propagation speed only, since it could also occur in an isentropic flow. Shocks on the other hand show up as pressure discontinuities. Unfortunately, no clear pressure discontinuity is measured, and no steep pressure drop can be identified to be an RSW in any of the experiments. The rise time of the pressure sensors is measured to be only  $30 \mu\text{s}$ , using the fully developed shock in nitrogen, see section 2.3.2. This means that the rather low pressure slope can not be attributed to sensor lag, but is a feature of the flow. The thickness of RSWs is unknown, but is suggested to be of the order of centimeters for D<sub>6</sub> siloxane [16]. Borisov *et al.* [10] reports a wave thickness of 3.3 cm. On top of that, a double-sonic RSW would be preceded and followed by a classical rarefaction fan, which dilates in space.

Furthermore, a kink in the pressure drop is visible in the pressure diagrams from all experiments, see fig 3.16, 3.18, 3.20, 3.22 and 3.24. This kink or plateau becomes more pronounced in the experiments in which the predicted values of  $\Gamma$  are lower. This suggests that it is influenced by the value of  $\Gamma$  and could be related to the formation of a shock. The kink was not visible at all in the measurements on D<sub>6</sub> flows performed with the fluid in conditions

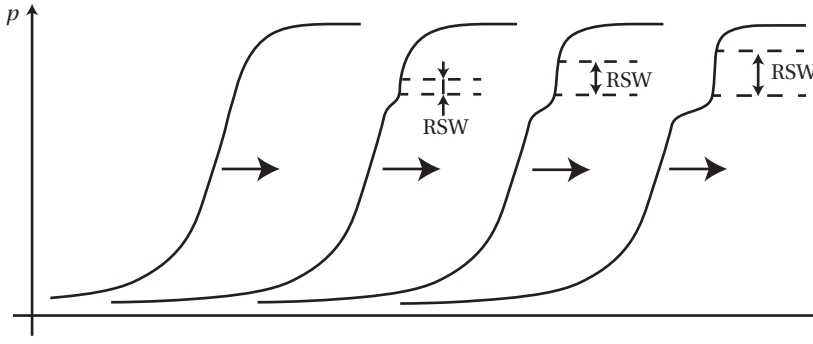


Figure 3.27: Schematic pressure distribution in the shock tube of a forming RSW. Initially a small RSW is formed. This shock accelerates and travels at a supersonic speed. This can create a dilation between the isentropic part of the wave and the shock. The shock grows in pressure jump, and further accelerates. A plateau with a lower pressure slope is created directly after the shock.

that were far away from the BZT zone. Moreover, in the  $N_2$  experiment, described in section 2.3.2, a compression shock is formed in the CT. At the location of sensor PT1 and PT2, the shock had not fully formed, and a similar kink in the pressure diagram is present. It might be that in these experiments, a similar formation of a shock is observed, albeit a double sonic RSW now.

A conjecture about the formation of the kink in the pressure signals can be devised as follows. Figure 3.27 shows schematically the resulting pressure distribution in the shock tube. As part of the expansion is within the negative  $\Gamma$  region, wave steepening and shock formation takes place. As the RSW travels faster than the speed of sound, a jump in propagation speed takes place after the RSW. This is the pressure level at which the kink or plateau forms. Figure 3.28 shows the pressure as would be recorded by the pressure transducers. The size of the plateau increases in space until the shock propagation speed is equal to the post-shock wave propagation speed. Contrary to the expectation, the kink in the pressure diagrams of the conducted experiments is present at a higher pressure level than the pressure at which the wave propagation speed diagram indicate the possible occurrence of a double-sonic RSW.

### 3.5. PREDICTION OF EXPERIMENTAL VALUE OF $\Gamma$

The derivative of the wave speed with respect to pressure is related to the value of  $\Gamma$ ,  $\rho$  and  $c$ , according to Thompson [5] by

$$\frac{dw}{dp} = \frac{\Gamma}{\rho c}. \quad (3.1)$$

The value of the derivative of wave speed with respect to pressure can be obtained by numerical differentiation of the wave speed, as obtained using the method described in section 3.3. In order to limit the noise, a zero-phase digital filter is applied to the wave speed signal, before differentiation. By applying this method to the velocity obtained by correlating the signals from sensor pair PT1/PT2 or PT3/PT4, noise and fluctuations still render impossible

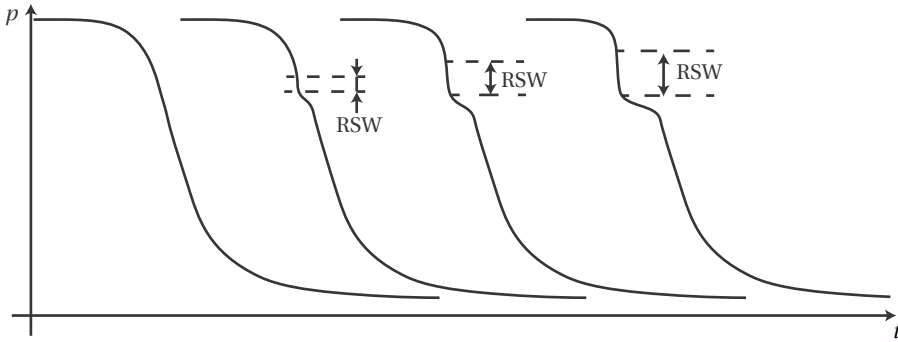


Figure 3.28: Schematic pressure recording at different locations in the shocktube of the formation of an RSW, corresponding to the formation of an RSW displayed in figure 3.27.

to estimate with meaningful accuracy the value of  $dw/dp$ . Applying the method to the velocity signal, acquired by correlating sensors PT1 and PT3, is affected by far less noise, since they are much farther apart, thus the wave propagation duration is longer. In order to obtain an estimate of  $\Gamma$ , also knowledge on the value of  $\rho$  and  $c$  is required. As these quantities are not directly measured, it is impossible to obtain a function relating  $\Gamma$  to the pressure drop in the signal. Instead, the experimental value of  $dw/dp$  is compared to the value obtained with the thermodynamic model of the fluid, see figures 3.29 to 3.33. The experimental value of  $dw/dp$  is higher than the predicted value, except below a pressure difference of -50 mbar and around -0.4 bar. The part of the experimentally determined  $dw/dp$  below -50 mbar is particularly noisy, because it includes the opening sequence of the valve, and the pressure slope is not very steep. The part around -0.4 bar coincides with the kink in the pressure signal. The higher experimental value of  $dw/dp$  compared to the predicted one can be explained either by temperature non-uniformity in the tube, or by the growth of the boundary layer in the tube. The expansion wave has a non-negligible thickness. Immediately after arrival of the first characteristic, a fluid flow starts. Consequently a boundary layer grows in the tube, reducing the effective flow passage area. This in turn accelerates the flow, which then decreases the wave propagation speed of the following part of the wave, as the wave speed equals  $c - u$ .

The value of  $\Gamma$  at stagnation conditions can be estimated by using the obtained experimental value of the speed of sound and a prediction of the density from the thermodynamic model. A selection is made from the  $dw/dp$  diagram taken using sensors PT1/PT3, between -0.07 bar and -0.2 bar, or the maximum undisturbed pressure drop of the signal of PT3. A linear regression is made through this curve, which is extrapolated to the undisturbed state at  $\Delta P = 0$ . Upon multiplication with the experimental value of the speed of sound and the model prediction of the density at this state, an estimate for  $\Gamma$  is obtained. The resulting values of  $\Gamma$  are shown in table 3.3 for all experiments. Even though these values suffer from large uncertainties, due to the extrapolation of  $c$  and derived quantity  $dw/dp$  to the undisturbed state, the values are still remarkably close to the model predictions, which are close to 0. Apart from experiment 3, also the trend is consistent with the thermodynamic model. The value

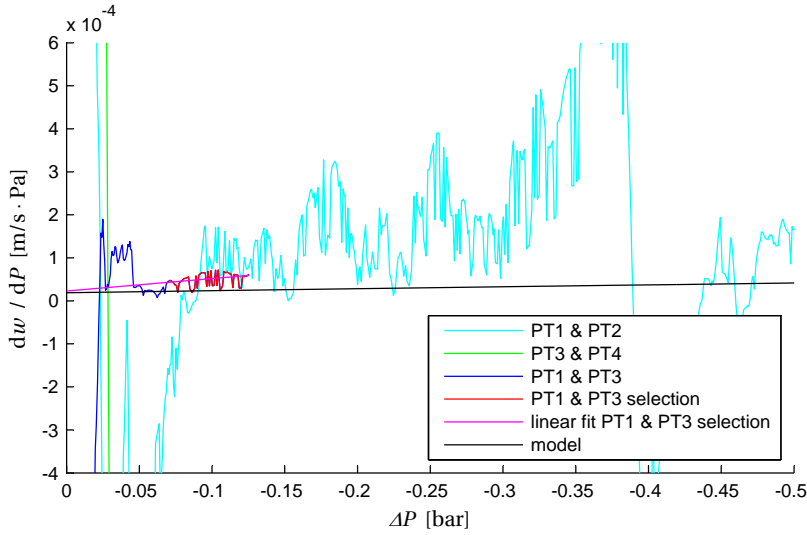


Figure 3.29: Derivative of wave speed with respect to pressure of experiment 1.

| no | $P_{\text{HFT}}$<br>[bar] | $T_{\text{CT}}$<br>[°C] | $\Gamma_{\text{model}}$<br>[-] | $\Gamma_{\text{exp}}$<br>[-] |
|----|---------------------------|-------------------------|--------------------------------|------------------------------|
| 1  | 8.4020                    | 367.6                   | 0.13                           | 0.18                         |
| 2  | 8.4705                    | 367.4532                | 0.09                           | 0.12                         |
| 3  | 8.5570                    | 367.8109                | 0.06                           | -0.14                        |
| 4  | 8.7926                    | 368.8427                | -0.02                          | -0.05                        |
| 5  | 8.7966                    | 368.9676                | -0.01                          | -0.09                        |

Table 3.3: Experimental values of  $\Gamma$  for the BZT experiments.  $\Gamma_{\text{model}}$  gives the predicted value of  $\Gamma$  using the thermodynamic model.  $\Gamma_{\text{exp}}$  gives the value extracted from the experimental data, by using the value of  $c_{\text{exp13}}$ , extrapolation of the value of  $dw/dp$  from sensors PT1 and PT3, and the model prediction of density  $\rho$ .

of  $\Gamma$  is higher in experiment 1 and 2 than experiment 4 and 5. Probably the thermodynamic conditions were not stable and uniform in experiment 3, see figure 3.3.

### 3.6. CONCLUSION & RECOMMENDATIONS

Five experiments using  $D_6$  as working fluid have been performed with thermodynamic states within or in the vicinity to the predicted BZT zone at various pressure and temperature levels. Differences in the thermodynamic quantities during the heating phase and the cooling phase of the experiment are recorded and could be explained in several ways. At low pressures, the uncertainty of the pressure transducer can lead to high deviations in saturation temperature. At higher pressures, it could be that either the fluid stratifies during the cooling phase, inducing temperature gradients in the vapour generator, or that the measurement of the temperature is affected by radiative heat transfer that could introduce an offset in the temperature reading. At the desired temperature, the wall temperature is kept at approx-



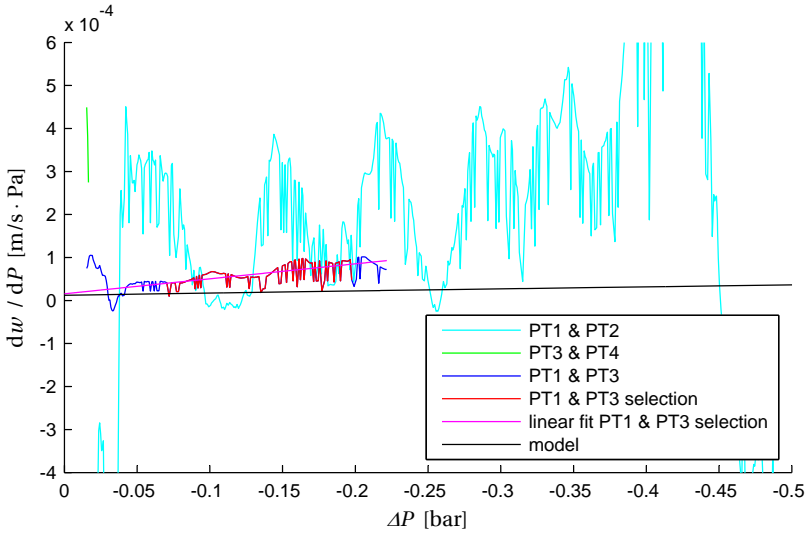


Figure 3.30: Derivative of wave speed with respect to pressure of experiment 2.

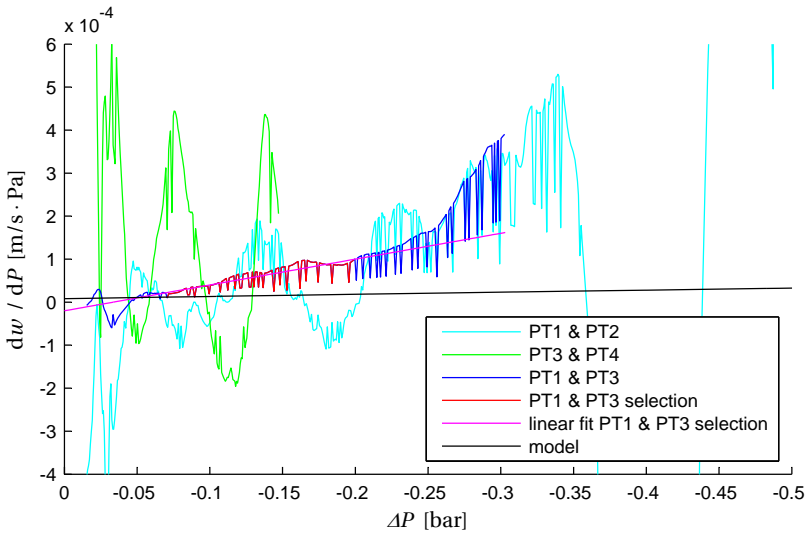


Figure 3.31: Derivative of wave speed with respect to pressure of experiment 3.

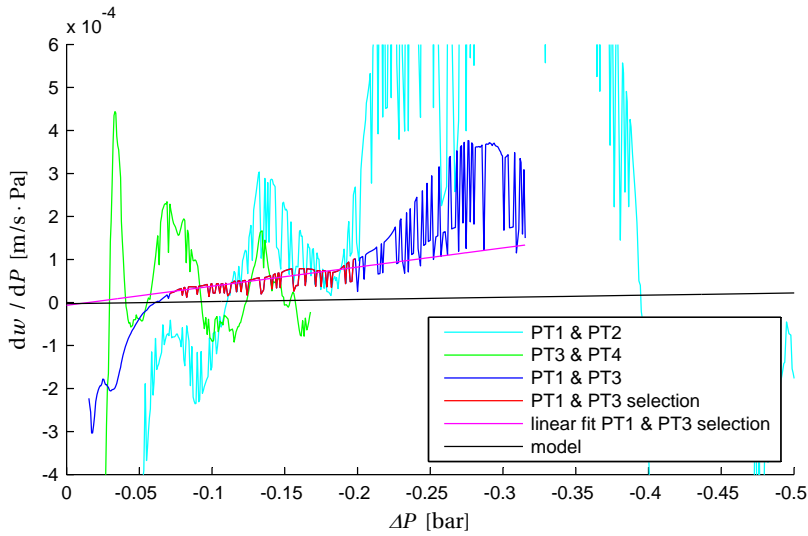


Figure 3.32: Derivative of wave speed with respect to pressure of experiment 4.

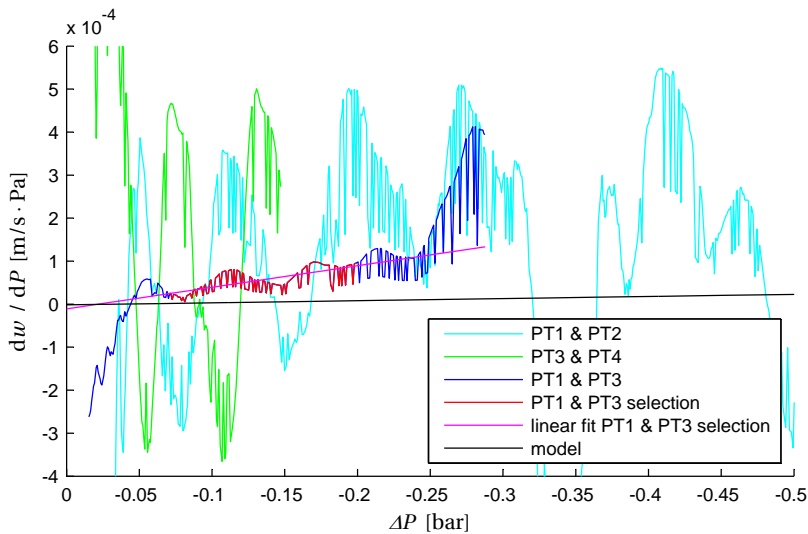


Figure 3.33: Derivative of wave speed with respect to pressure of experiment 5.

imately 5 °C higher than the recorded fluid temperature. The recorded fluid temperature is between 1.5 and 2.5 °C higher than that predicted by the best available thermodynamic model. However, the model is affected by uncertainties, and the influence of the approximately 4 % impurities contained in the working fluid on the saturation line is difficult to estimate.

Recordings of the signals from high-frequency pressure sensors display a clear difference between experiments on D<sub>6</sub> with thermodynamic states with estimated  $\Gamma$  close to zero than those at considerably lower pressure and temperature. In particular the plot of the pressure signal versus time shows a kink starting at a value of the pressure that is 0.4 bar lower than the initial value. Such kink might be explained as the onset of the formation of an RSW, though conclusive evidence is still lacking.

The measurements allow to estimate the speed of sound in the quiescent fluid. The obtained values are between approximately 45 m/s and 55 m/s and deviate by approximately 5 m/s from the values calculated with the best available thermodynamic model, which is also affected by possibly larger uncertainty. Additional sources of uncertainty are: the composition of the fluid, and the thermodynamic state (P and T) of the fluid. In the presented experiments, the indicated amount of superheating was very low in the experiments, down to 0.5 °. The recorded saturation temperature may be affected by measurement error due to radiative heat transfer from the vapour generator wall. The fact that the flow occurring in these experiments is within the NICFD regime, is confirmed by the fact that fluid states at higher pressure and temperature feature lower speed of sound, indicating that  $\Gamma$  must be lower than 1. The value of  $\Gamma$  that can be estimated from the wave speed, is surprisingly close to that predicted by the equation of state model, and is close to zero, showing that nonclassical effects could be expected. The estimation of  $\Gamma$  is however affected by large uncertainties, being derived not only from measured values, but also from an estimation of local density.

In order to conclusively confirm nonclassical gasdynamic phenomena, a more thorough investigation is required for thermodynamic states encompassing the BZT zone. The process start-up time appears to be critical, since possibly the onset of shock formation, but no fully developed RSW has been recorded. It can be considered to remove the nozzle insert. Doing so will decrease the FOV process start-up time with the nozzle start-up duration, at the cost of disturbances being able to travel upstream.

# 4

## SIMULATIONS OF NICFD SHOCK TUBE FLOWS IN THE VAPOUR-LIQUID CRITICAL POINT REGION USING A THERMODYNAMIC MODEL BASED ON SCALING LAWS

Selected contents from:

Nannan, N., Sirianni, C., Mathijssen, T., Colonna, P., Guardone, A. The admissibility domain of fluids in the vapour-liquid critical point region. *J. Fluid Mech.* 56:10, March (2016).

### 4.1. INTRODUCTION

NICFD can occur not only in vapour flows, but also in flows of fluids that are in the liquid-vapour two-phase region. The fluid dynamic theory of these fluid flows can be treated under the assumption of thermodynamic equilibrium of the phases, though this assumption must be carefully verified. Under the assumption of vapour-liquid equilibrium it is possible to define  $\Gamma$  for wet thermodynamics states of the fluid. The speed of sound value changes abruptly at the saturation line [60], i.e., an infinitesimal amount of liquid in vapour or of vapour in liquid greatly affects its value. Examples in which a fluid flow undergoes a phase change and for which the fluid, under certain conditions, may be assumed in thermodynamic equilibrium are the cavitation of a liquid in a pump, the formation of droplets in the expansion of vapour in a turbine, or the formation of fog above the wing of an aircraft flying in humid air conditions. Retrograde fluids, whose thermodynamic properties feature a positive slope of the dew line in the temperature-entropy diagram, can be expanded from the two-phase region into the vapour region, or compressed from the vapour region into

to states in which vapour is in equilibrium with liquid. In all these examples, the speed of sound displays a discontinuity at the liquid-vapour interface. The definition of  $\Gamma$ , as a first order derivative of  $c$ , implies that the value of  $\Gamma$  goes to an infinite value, either positive or negative. NICFD flows can therefore occur, and in case  $\lim \Gamma \rightarrow -\infty$ , nonclassical gasdynamic phenomena can take place [61]. Examples are the evaporation shockwave [62] and shock splitting of a liquefaction shock [63], which are both demonstrated experimentally.

Schlamp and Rösigen [64] give another example of close-to-critical NICFD flows. They measured a shock, whose pre- and post-shock states are on opposite sides of the saturation line. They present a method to obtain a flow in which the fluid is in the critical state or close to it, by using a shocktube to generate a shock or expansion with critical post wave conditions. Such flows are interesting for fundamental studies on the critical point. Flows generated in this manner do not require the long lead time necessary to reach thermal equilibrium as in other experimental methods.

4

Recently, Nannan *et al.* [15] showed that the value of  $\Gamma$  close to the vapour-liquid critical point diverges to  $\infty$  when approached from the single phase or supercritical region, and diverges to  $-\infty$  when approached from the two-phase region. This is distinctively different from crossing the saturation line as discussed above, in the sense that the value of  $\Gamma$  is negative in a finite thermodynamic region, instead of only along the saturation line. Non-classical waves, such as RSWs, can occur in a finite rarefaction shock wave region [65]. In fact, experimental validation for this type of two-phase nonclassical flows may already be present. In 1983, Borisov *et al.* [10] claimed to have measured an RSW in Freon-13 (trifluorochloromethane,  $\text{CClF}_3$ ) in a state very close to its critical point, using a conventional shock tube with diaphragm bursting. The waveform of the propagating rarefaction remained unchanged, indicating the expansion to be an RSW. The authors claim that the shock occurred in the dense vapour of Freon-13. However, on the basis of arguments and computations presented by Ferguson *et al.* [12, 17], Ferguson and Argrow [66] and recently by Nannan *et al.* [15], the results of Borisov *et al.* [10] provide inconclusive evidence of the occurrence of such an event. The measured pressure signal can be explained in different ways, and one of the hypotheses is that the flow under scrutiny occurred with the fluid in states featuring negative values of  $\Gamma$  in the two-phase thermodynamic region.

This chapter presents simulations of shock tube flows that are performed with the aim of numerically verifying the admissibility of nonclassical gasdynamic phenomena in the two-phase region close to the critical point of fluids. The correctness of such simulations depends on the proper estimation of the fluid thermodynamic properties, a non-trivial problem treated in section 4.2. The adopted numerical flow solver is described in section 4.3. Details on the temporal and spatial distribution of formed waves in a shock tube are presented and key requirement parameters for the design of an experimental validation of such flows are identified in section 4.4. This section also contains the description of a newly conceived method to obtain a flow of saturated fluid due to wave splitting with a shock tube. Related flow simulations are also presented. Simulations on such a shock tube experiment is also presented in the same section. Finally some concluding remarks are outlined in section 4.5.

## 4.2. THERMODYNAMIC MODEL

As it is well known, several thermodynamic and transport properties either diverge or go to zero at the vapour-liquid critical point; the slope of the  $P$ - $T$  curve is however an exception, see, e.g. Levelt-Sengers [67]. Notable examples of anomalous trends include the weak divergence of the isochoric heat capacity  $c_v$ , the strong divergence of the isothermal compressibility  $\kappa_T \equiv -1/\nu(\partial\nu/\partial P)_T$ , the weak approach to zero of the thermodynamic (zero-frequency) sound speed at the critical point, and the strong divergence of the thermal conductivity, see for example the works of Michels *et al.* [68], Albright *et al.* [69], Kurumov *et al.* [70] and Levelt-Sengers *et al.* [71] and listed references therein reporting corresponding experimental data. The Helmholtz free energy is non-analytic at the critical point, as the direct consequence of the divergence of  $c_v$  near the critical point. Consequently, classical equations of state (EoS), being analytic functions, cannot correctly model the vapour-liquid critical region. The limitations of cubic equations of state in this respect are well-known, but even the modern, most accurate multi-parameter equations of state, including those incorporating so-called critical terms in their functional form [72], cannot accurately predict the primary thermodynamic properties and even more so secondary or derived properties at the critical point. Colonna *et al.* [73] and Nannan *et al.* [15] pointed out that even the highly accurate reference model of Wagner Setzmann containing critical terms cannot provide correct evaluations of  $\Gamma$  if the considered fluid states are close enough to the critical point.

In order to accurately predict the thermodynamic quantities close to the critical point, one has to resort to scaling principles [67, 74]. These scaling laws models have the advantage of being universal for all fluids governed by close-range forces, so called 3-dimensional Ising-like systems. Balfour *et al.* [75] presented the revised and extended-linear version of the fundamental equation, which expresses the potential  $P/T$  as an expansion in terms of  $1/T$  and  $\mu/T$ , in which  $P$  is the pressure,  $T$  is the temperature and  $\mu$  is the chemical potential. These values are made dimensionless with the critical parameters

$$\tilde{P} \equiv \frac{P}{T} \frac{T_C}{P_C}, \quad \tilde{T} \equiv -\frac{T_C}{T}, \quad \tilde{\mu} \equiv \frac{\mu}{T} \frac{\rho_C T_C}{P_C}, \quad (4.1)$$

in which  $T_C$ ,  $P_C$  and  $\rho_C$  refer to the critical temperature, pressure and density respectively. The fundamental equation is

$$\tilde{P} = 1 + \sum_{i=1}^3 \tilde{P}_i (\Delta \tilde{T})^i + \Delta \tilde{\mu} (1 + \tilde{P}_{11} \Delta \tilde{T}) + \Delta \tilde{P}. \quad (4.2)$$

The terms  $\tilde{P}_{i=1..3}$  and  $\tilde{P}_{11}$  are fluid dependent pressure background parameters.  $\Delta \tilde{T}$  and  $\Delta \tilde{\mu}$  are the difference in temperature and chemical potential respectively from the critical point and are expressed as

$$\Delta \tilde{T} = \tilde{T} + 1, \quad \Delta \tilde{\mu} = \tilde{\mu} - \tilde{\mu}_C - \sum_{i=1}^4 \tilde{\mu}_i (\Delta \tilde{T})^i, \quad (4.3)$$

The non-analytic part of equation 4.2, i.e.  $\Delta \tilde{P}$ , is expressed as

$$\Delta \tilde{P} = ar^{\beta(\delta+1)} [k_0 p_0(\theta) + r^{\Delta_1} k_1 p_1(\theta)]. \quad (4.4)$$

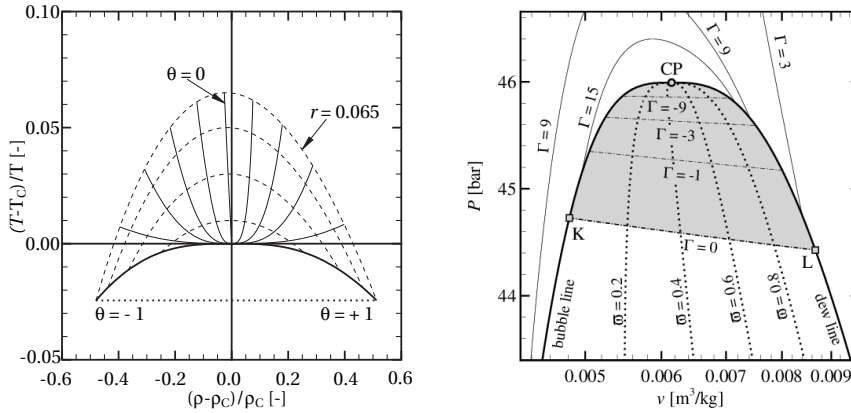


Figure 4.1: Left: Definition of the critical region in terms of the parametric coordinates  $\theta$  and  $r$ , valid for the universality class of 3-dimensional Ising-like systems. Right: Lines of constant fundamental derivative of gas dynamics  $\Gamma$  in the vapor-liquid equilibrium region of methane near its critical point, illustrated in the pressure-specific volume diagram. The shaded region is the  $\Gamma < 0$  region. The gray circle indicates the vapour-liquid critical point. The dotted lines are lines of constant vapour mass-fraction  $\varphi$ .

$\beta$ ,  $\delta$  and  $\Delta_1$  are universal critical exponents,  $a$ ,  $k_0$  and  $k_1$  are substance specific parameters, and  $p_0(\theta)$ ,  $p_1(\theta)$  are auxiliary functions.  $r$  and  $\theta$  are parametric variables first introduced by Schofield [76]. The term  $r$  is a measure for the distance of the thermodynamic state from the critical point, and determines the singular behaviour, such that  $r \geq 0$ . Subsequently,  $\theta$  denotes the distance around lines of constant  $r$  from one side of the coexistence curve to the other.  $\theta = -1$  corresponds then to the dew line and  $\theta = 1$  corresponds to the bubble line, such that  $-1 \leq \theta \leq 1$ . This is visualised in figure 4.1. Balfour *et al.* [75] introduced the expressions of  $\Delta \tilde{T}$  and  $\Delta \tilde{\mu}$  as a function of  $r$  and  $\theta$ , namely

$$\Delta \tilde{T} = r(1 - b^2 \theta^2) - c \Delta \tilde{\mu}, \quad \Delta \tilde{\mu} = ar^{\beta \delta} \theta(1 - \theta^2), \quad (4.5)$$

in which  $b^2$  is a universal constant and  $c$  a fluid-specific parameter.

From equation 4.2, all other thermodynamic properties can be derived. Functions to derive many such thermodynamic variables are explicit in variables  $r$  and  $\theta$ , and are given in the appendix of [15]. Computational fluid dynamic codes commonly require that thermodynamic property estimations are performed with variables other than pressure and temperature. For example, density  $\rho$  and specific internal energy  $u$  are often adopted as primary variables in codes for inviscid compressible flow simulations. In this work, a well-known in-house code [54] has been used as the infrastructure for the evaluation of thermodynamic properties, in which the scaling-law model is implemented. In order to achieve this, it was necessary to develop algorithms to find the value of  $r$  and  $\theta$  based on the bisection and Brent method [77]. Because the solution of the root-finding algorithm depends on more than one variable, viz. two thermodynamic variables, the algorithms turn out to be rather complex, and dependent on the chosen set of input variables. Functions that allow for the calculation

of thermodynamic properties starting from various combinations of input variables have been implemented. Possible couples of input variables are:  $P$  and  $T$ ,  $P$  and  $\rho$ ,  $P$  and  $q$ ,  $T$  and  $\rho$ ,  $T$  and  $q$ , and  $\rho$  and  $e$ . Once  $r$  and  $\theta$  are found, all other thermodynamic properties can be calculated explicitly.

### 4.3. NUMERICAL SOLVER

In this study on unsteady compressible flows, the effects of viscosity, heat conduction, external heating and forces are neglected, such that the conservation laws can be rewritten as the Euler equations, given by

$$\frac{\partial \rho}{\partial t} + \nabla \cdot \rho \mathbf{V} = 0, \quad (4.6)$$

$$\frac{\partial}{\partial t} \rho \mathbf{V} + \nabla \cdot (\rho \mathbf{V} \cdot \mathbf{V}) + \nabla P = 0, \quad (4.7)$$

$$\frac{\partial}{\partial t} E_t + \nabla \cdot (E_t + P) \mathbf{V} = 0, \quad (4.8)$$

with  $E_t = \rho (e + \frac{1}{2} u^2)$ . For the 1-dimensional case, these equations can be written in compact form as

$$\frac{\partial \mathbf{U}}{\partial t} + \frac{\partial \mathbf{F}}{\partial x} = 0 \quad (4.9)$$

with

$$\mathbf{U} = \begin{pmatrix} \rho \\ m \\ E_t \end{pmatrix}, \quad \mathbf{F} = \begin{pmatrix} m \\ mu + P \\ u(E_t + P) \end{pmatrix}. \quad (4.10)$$

where  $m = \rho u$  and  $P = f(\rho, e)$ .

It is assumed that the phase change takes place homogeneously. Moreover, the two phases do not separate, and are thus in thermodynamic equilibrium. For the current study, these assumptions are justified because the density differences are limited and the surface tension is low, due to the proximity to the critical point. Furthermore, the presented experiments feature very limited time at which the fluid is in a thermodynamic state featuring two phases.

Time integration is done using a simple upwind scheme:

$$\mathbf{U}_i^{N+1} = \mathbf{F}_i^N - \frac{\Delta t}{\Delta x} (\mathbf{F}_{i+\frac{1}{2}} - \mathbf{F}_{i-\frac{1}{2}}). \quad (4.11)$$

The Roe type approximate Riemann solver adapted to real gas flows, which is presented by Guardone and Vigevano [78], is used to find a solution to the Euler equations. This method is based on a strictly Jacobian form, in which the Jacobian matrix  $\mathbf{A}(\mathbf{U}) = \partial \mathbf{F}(\mathbf{U}) / \partial \mathbf{U}$  is evaluated in an intermediate state  $\tilde{\mathbf{U}} = \tilde{\mathbf{U}}(\mathbf{U}_L, \mathbf{U}_R)$ . The flux vector now reads

$$\mathbf{F}_{i+\frac{1}{2}} - \mathbf{F}_{i-\frac{1}{2}} = \mathbf{A}(\tilde{\mathbf{U}}(\mathbf{U}_L, \mathbf{U}_R)) (\mathbf{U}_R - \mathbf{U}_L), \quad (4.12)$$



with as a Jacobian matrix

$$\mathbf{A}(\tilde{\mathbf{U}}) = \begin{pmatrix} 0 & 1 & 0 \\ -\frac{\tilde{m}^2}{\tilde{\rho}^2} + \frac{\partial \tilde{P}(\tilde{\rho}, \tilde{e})}{\partial \tilde{\rho}} & \frac{2\tilde{m}}{\tilde{\rho}} + \frac{\partial \tilde{P}(\tilde{\rho}, \tilde{e})}{\partial \tilde{m}} & \frac{\partial \tilde{P}(\tilde{\rho}, \tilde{e})}{\partial \tilde{E}_t} \\ \frac{\tilde{m}}{\tilde{\rho}} \left( -\frac{\tilde{E}_t + \tilde{P}(\tilde{\rho}, \tilde{e})}{\tilde{\rho}} + \frac{\partial \tilde{P}(\tilde{\rho}, \tilde{e})}{\partial \tilde{\rho}} \right) & \frac{\tilde{E}_t + \tilde{P}(\tilde{\rho}, \tilde{e})}{\tilde{\rho}} + \frac{\tilde{m}}{\tilde{\rho}} \frac{\partial \tilde{P}(\tilde{\rho}, \tilde{e})}{\partial \tilde{m}} & \frac{\tilde{m}}{\tilde{\rho}} \left( 1 + \frac{\partial \tilde{P}(\tilde{\rho}, \tilde{e})}{\partial \tilde{E}_t} \right) \end{pmatrix}. \quad (4.13)$$

Unlike the Van der Waals equation of state [78], no exact Roe linearization method is available for the equation of state under scrutiny. Also, a method of calculating the pressure as a function of density and enthalpy is not available for the scaling-law thermodynamic model. The choice made for an intermediate state does not lead to an exact Roe linearisation, because of the selected Roe average for the internal energy. However, Cinnella [79] showed that such intermediate states results in first-order accuracy for converging simulations. The intermediate state vector is given by

$$\tilde{\mathbf{U}} = \begin{pmatrix} \tilde{\rho} \\ \tilde{m} \\ \tilde{E}_t \end{pmatrix}. \quad (4.14)$$

Furthermore, the Van Leer flux limiter is applied to ensure stability of the solution and a Hartman-Hyman entropy fix is applied for transonic calculations.

#### 4.4. SIMULATION RESULTS

This section presents the results of computational fluid dynamic simulations. First, the code is validated by simulating the generation of waves, for which the theoretical results are presented by Nannan *et al.* [16]. The results of this simulation is shown in subsection 4.4.1. The valve opening time or diaphragm breaking time is of crucial importance for the successful experimental validation this type of flow fields. An estimate of the requirement on the maximum time for diaphragm rupture or valve opening is devised, depending on the initial thermodynamic state, and its results for methane and CO<sub>2</sub> are presented in subsection 4.4.2. An experiment is proposed and simulated, featuring an RSW in the two-phase regime of CO<sub>2</sub>, for which the initial thermodynamic states are in the single-phase regime, and is presented in section 4.4.3.

##### 4.4.1. SIMULATIONS OF NONCLASSICAL WAVES IN METHANE

Nannan *et al.* [16] describe the theoretical solution of two examples of nonclassical waves: a post-sonic RSW, and a mixed wave consisting of a post-sonic compression shock, a compression fan and a pre-sonic compression shock, which are referred to the RSW experiment and mixed wave experiment respectively hereafter. The thermodynamic states of these waves are shown in a pressure - specific volume diagram in figure 4.2. The shock adiabat together with a position - time diagram is shown schematically in figure 4.3 for the RSW experiment and in figure 4.4 for the mixed wave experiment.

Results from theoretical calculations, presented in table 4.1, are different from the results reported by Nannan *et al.* [16]. The entropy jump over the RSW is calculated to be  $1.06 \cdot 10^{-3}$  J/kg K. For the mixed wave, the same value of entropy jump, i.e.  $s_2 - s_1 = 2.30 \cdot 10^{-5}$  J/kg K for the first shock in the mixed wave is found, but the second shock has a value of  $s_4 - s_3 = 5.82$

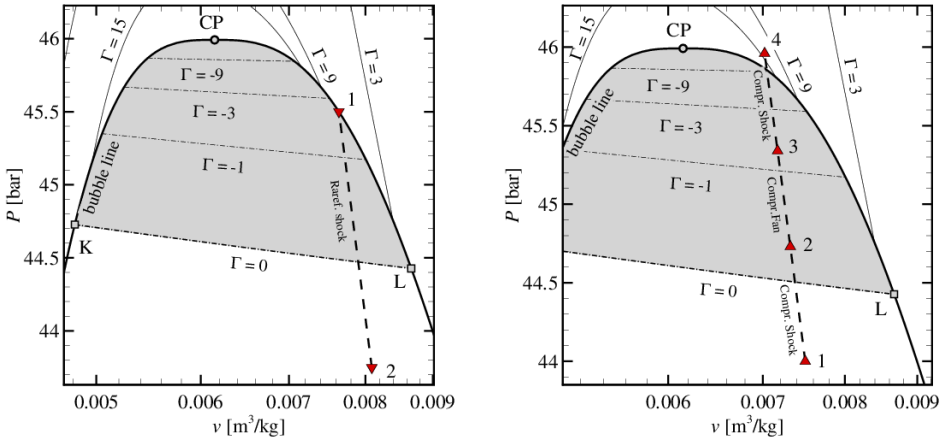


Figure 4.2: Fluid state from Nannan *et al.* [16] in the volume-pressure plane, see Table 4.1, for the rarefaction shock wave described in Figure 4.3 (left) and the composite wave in Figure 4.4 (right). Note that the composite wave is a compressive wave.

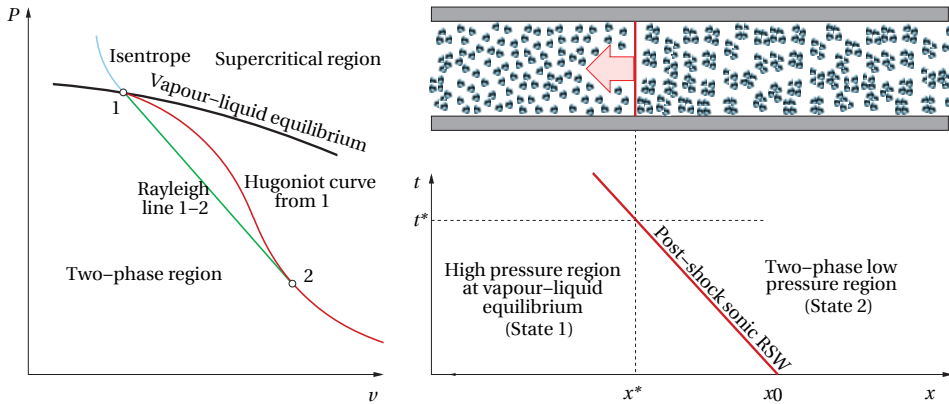


Figure 4.3: Illustrative sketch taken from Nannan *et al.* [16], showing the example, not to scale, of the shock adiabat from state 1, its curvature, and the Rayleigh line connecting pre- and post-shock states 1 and 2 related to an admissible rarefaction shock wave according to Figure 4.2 (left). Also shown is the  $x-t$ -plot and a snapshot of the flow field in a shock tube at time  $t = t^*$  at the corresponding location. RSW is the abbreviation of rarefaction shock wave.

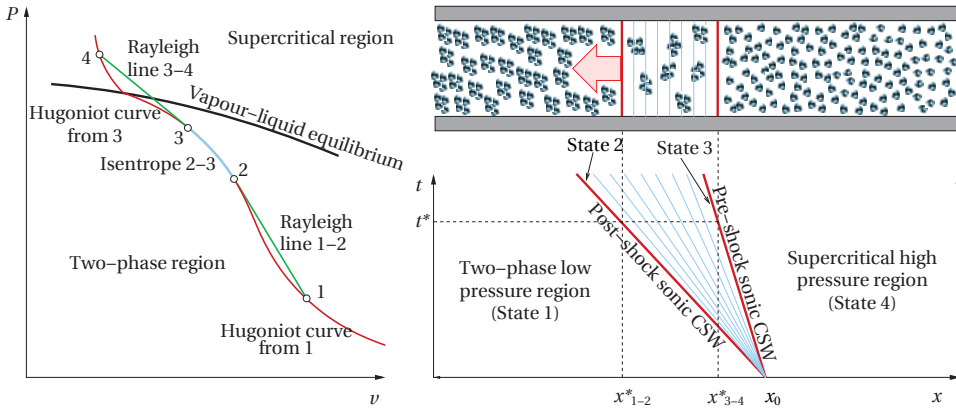


Figure 4.4: Graph taken from Nannan *et al.* [16] with the example of a composite compression wave displaying a non-classical compression shock wave (1 → 2) with a sonic post-shock Mach number ( $Ma_2 = 1$ ), an isentropic compression fan (2 → 3) and a second non-classical compression shock wave (3 → 4) with a sonic pre-shock Mach number ( $Ma_3 = 1$ ). State 1 is in the vapour-liquid equilibrium region with  $\Gamma > 0$  and state 4 is in the supercritical or dense-gas region with  $\Gamma > 0$ . Also shown is the  $x-t$ -plot whereby the compression fan is bounded by two compression shock waves, and a schematic representation (snapshot) of the flow field in a shock tube at time  $t = t^*$  at the corresponding location. CSW is the abbreviation of compression shock wave.

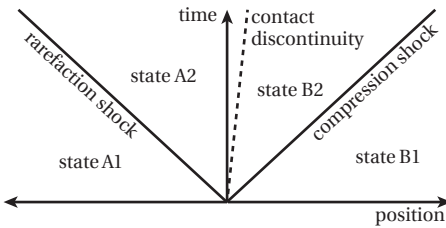


Figure 4.5: Position - time diagram of the Riemann problem of the RSW experiment.

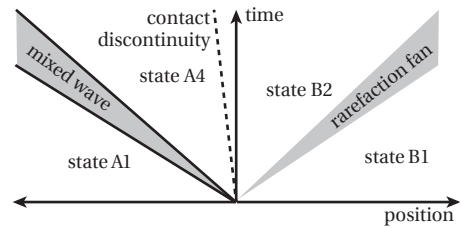


Figure 4.6: Position - time diagram of the Riemann problem of the mixed wave experiment.

$\cdot 10^{-4}$  J/kg K.

A shock tube experiment is simulated in order to numerically verify the theoretical predictions, which would then point to some mistakes in the calculations that led to the results published by Nannan *et al.* [16]. The length of the shock tube is arbitrarily taken as 50 m. A diaphragm separates two equal compartments, with the fluid in the left section of the pipe in pre-shock conditions of the two model waves described by Nannan *et al.* [16]. The conditions of the right section are chosen such that the pressure and velocity comply with the post-shock conditions. The diaphragm breaks instantaneously, inducing the propagation of an expansion wave into the high pressure compartment, and a compression wave into the low pressure compartment. A schematic overview of the solution to the Riemann problem of the RSW experiment is shown in figure 4.5, and of the mixed wave experiment in figure 4.6.

|                        | State | $P$<br>[bar] | $\nu$<br>[m <sup>3</sup> /kg] | $T$<br>[K] | $\Gamma$<br>[-] | Ma<br>[-] |
|------------------------|-------|--------------|-------------------------------|------------|-----------------|-----------|
| Rarefaction shock wave | A1    | 45.50        | 0.00764                       | 190.21     | -2.30           | 1.022     |
|                        | A2    | 43.74        | 0.00809                       | 188.95     | 0.376           | 1.000     |
| Mixed compression wave | A1    | 44.00        | 0.00750                       | 189.13     | 0.288           | 1.002     |
|                        | A2    | 44.73        | 0.00732                       | 189.66     | -0.199          | 1.000     |
|                        | A3    | 45.34        | 0.00717                       | 190.09     | -1.400          | 1.000     |
|                        | A4    | 45.91        | 0.00703                       | 190.50     | 15.47           | 0.685     |

Table 4.1: Thermodynamic conditions leading to the formation of the single rarefaction shock wave in Figure 3 and of the composite wave in Figure 4. The Mach number is computed in the wave reference frame.

After instantaneous diaphragm rupture, a post-sonic RSW propagates into the left compartment, and a compression shock into the right. The RSW pre-shock conditions of the fluid correspond to those of a vapour-liquid state on the saturation line, featuring a negative value of  $\Gamma$ . In reality such initial conditions are very difficult to achieve precisely. The post-shock conditions are inside the two-phase region, but outside the region of negative  $\Gamma$ . The compression wave features only states in the positive- $\Gamma$  region. The solution of simulation at different simulated times is presented in figure 4.7 with a grid size of 8001 cells and a time step of  $10^{-5}$  s. Contrary to single-phase Riemann problems, in two-phase Riemann problems, not only pressure and flow velocity are equal across the contact discontinuity, but also temperature. This is due to the assumption of thermodynamic equilibrium, such that pressure and temperature are coupled in the two-phase regime. On the other hand, a jump in vapour fraction is present.

The simulations are performed in the laboratory reference frame. The results can be displayed in the shock reference frame, by adding or subtracting the covered distance of the shock from the laboratory frame position and the shock velocity. This is done for the RSW using the predicted shock speed, see figure 4.8. In this figure also the theoretically predicted pre- and post-shock values are shown by the dashed lines. The simulated shock matches well with the theoretical predictions. At 1 ms, the contact discontinuity is still visible in the image at  $x = 0.15$  m, because of its proximity to the RSW. Interestingly, a region with a Mach number below 1 is visible in the simulation, despite the fact that the pre-shock Mach number is higher than one and the post-shock Mach number equals unity. This is attributed to the used numerical algorithm [80], which introduces an artificial viscous shock structure in the inviscid computations. Another observation is the relatively high number of nodes that are required to describe the RSW, i.e. 30 nodes in contrast to the 5 to 8 nodes that are typically required for a compression shock in an ideal gas [81]. This is attributed to the value of  $\Gamma$  being close to 0, which is the case for linear degeneracy of the characteristic field.

In the mixed wave experiment, the compression passes through the negative- $\Gamma$  region. This forms a mixed wave, composed of a post-sonic compression shock wave, a nonclassical isentropic compression fan, and a pre-sonic compression shock wave, see figure 4.6. The

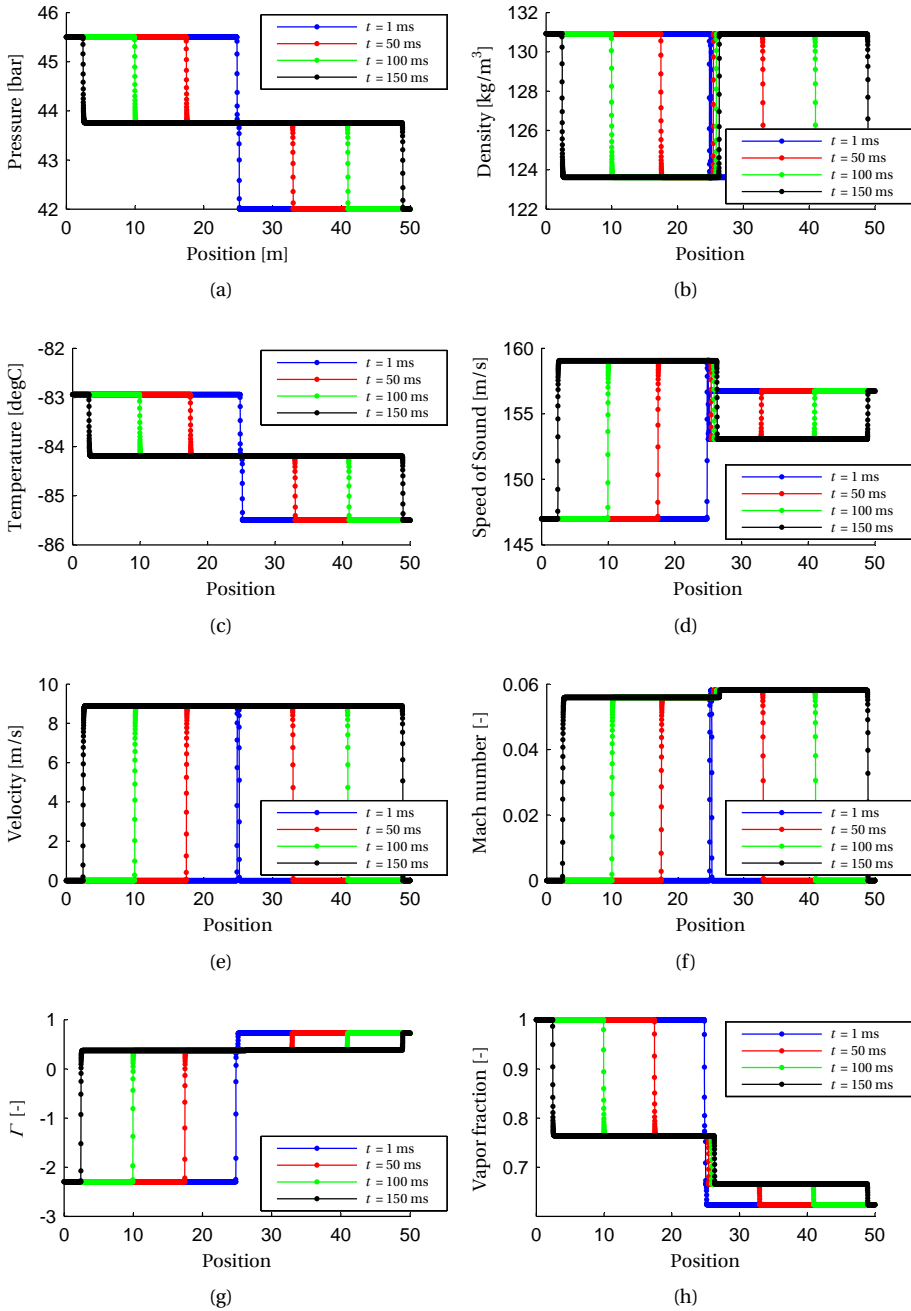


Figure 4.7: Simulation results of the RSW experiment in methane in the laboratory reference frame.

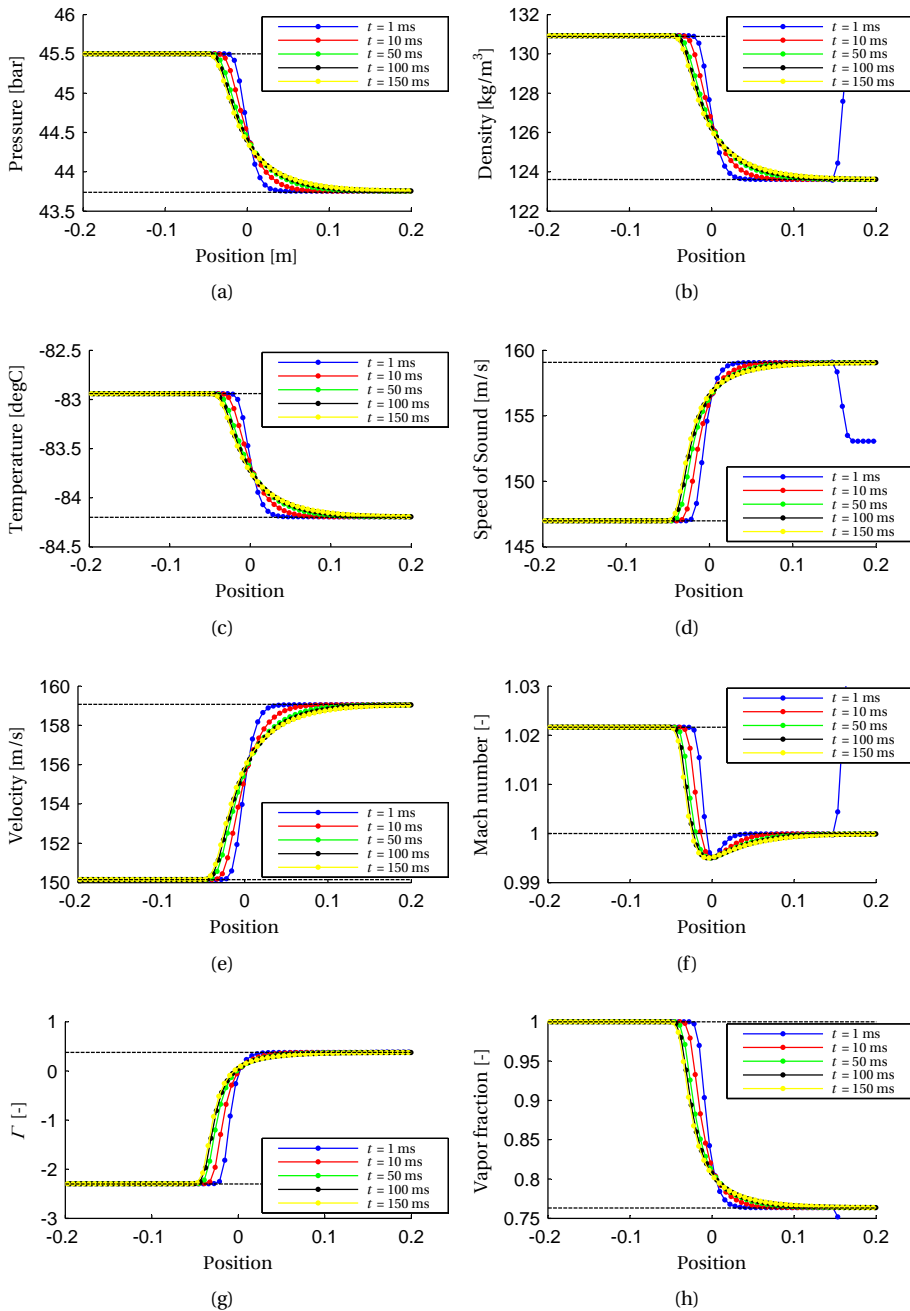


Figure 4.8: Simulation results of the RSW experiment in methane in the shock reference frame.

first shock travels at a higher speed than the second shock, such that the mixed wave as a whole dilates. The solution of the simulation at various time steps is presented in figure 4.9. This simulation uses a grid size of 8001 cells and a time step of  $10^{-5}$  s, equal to the RSW experiment. A similar procedure is applied to the mixed wave experiment as to the RSW experiment to present the simulation result in the shock reference frame for both shocks of the mixed wave. The simulation in the shock reference frame of the first shock of the mixed wave is presented in figure 4.10 and of the second shock in figure 4.11. Also the theoretical prediction of the four pre- and post-shock conditions, state A1 to A4 in table 4.1, are displayed with the dashed lines. The simulated pre- and post-state A1 and A4 comply accurately with the theoretical values. The first shock is immediately followed by the nonclassical compression fan, which in turn is followed immediately by the second shock. Numerical diffusion smooths the shock discontinuity, such that it is impossible to identify the position at which the shock ends and the isentropic compression starts. Consequently, it is impossible to accurately determine the simulated post-shock state of the first shock A2, and the pre-shock state of the second shock A3. On the other hand, it is clear that for the first shock, there is some overshoot on the post-shock Mach number. This is predicted to be 1, as was the case for the RSW experiment, while a value below 1 is simulated. For the second shock, the pre-shock Mach number, which is also predicted to be sonic, is too high in the simulations. Consequently, also the shock speed is 0.2 % higher than predicted.

#### 4.4.2. SHOCK FORMATION

The simulations described in section 4.4.1 are based on an idealised situation in which the two compartments are connected instantaneously. In reality, the two tube sections are typically connected by the breaking of a diaphragm or opening of a valve. Depending on the diaphragm material and temperature, the opening mechanism, and the acoustic impedance of the fluid, it is possible to obtain the breaking of a diaphragm in a time of the order to several hundreds of microseconds [32], while the opening of a fast-acting valve can take milliseconds [82]. In order to obtain merging of the characteristics and formation of a shock wave within the length of the facility, the opening duration must be limited. The maximum duration depends on the merging of the characteristics, defined by the variation of wave propagation speed. The merging rate is proportional to the value of  $\Gamma$ , in which a value of zero means that the characteristics are parallel, a negative value of  $\Gamma$  indicates convergence and merging of rarefaction waves, and a positive value indicates convergence and merging of compression waves. Given a certain value of valve opening time, or diaphragm breaking time, the minimum tube length required to achieve shock formation occurs when all characteristics merge in a single point. The wave propagates as a shock wave after this point. The region in which the shock has not yet formed is a homentropic simple region. A schematic representation of such a case is displayed in figure 4.12. When the characteristic do not merge in a single point, the required tube length is greater, see figure 4.13. The opening sequence of the valve or rupture of the diaphragm thus influences the maximum duration limit.

A simulation of the RSW experiment in methane, in which all characteristics merge in a single point, is executed by imposing a boundary condition at the location of the valve or diaphragm, in which the wave propagation speed is increasing linearly in time. By evalua-

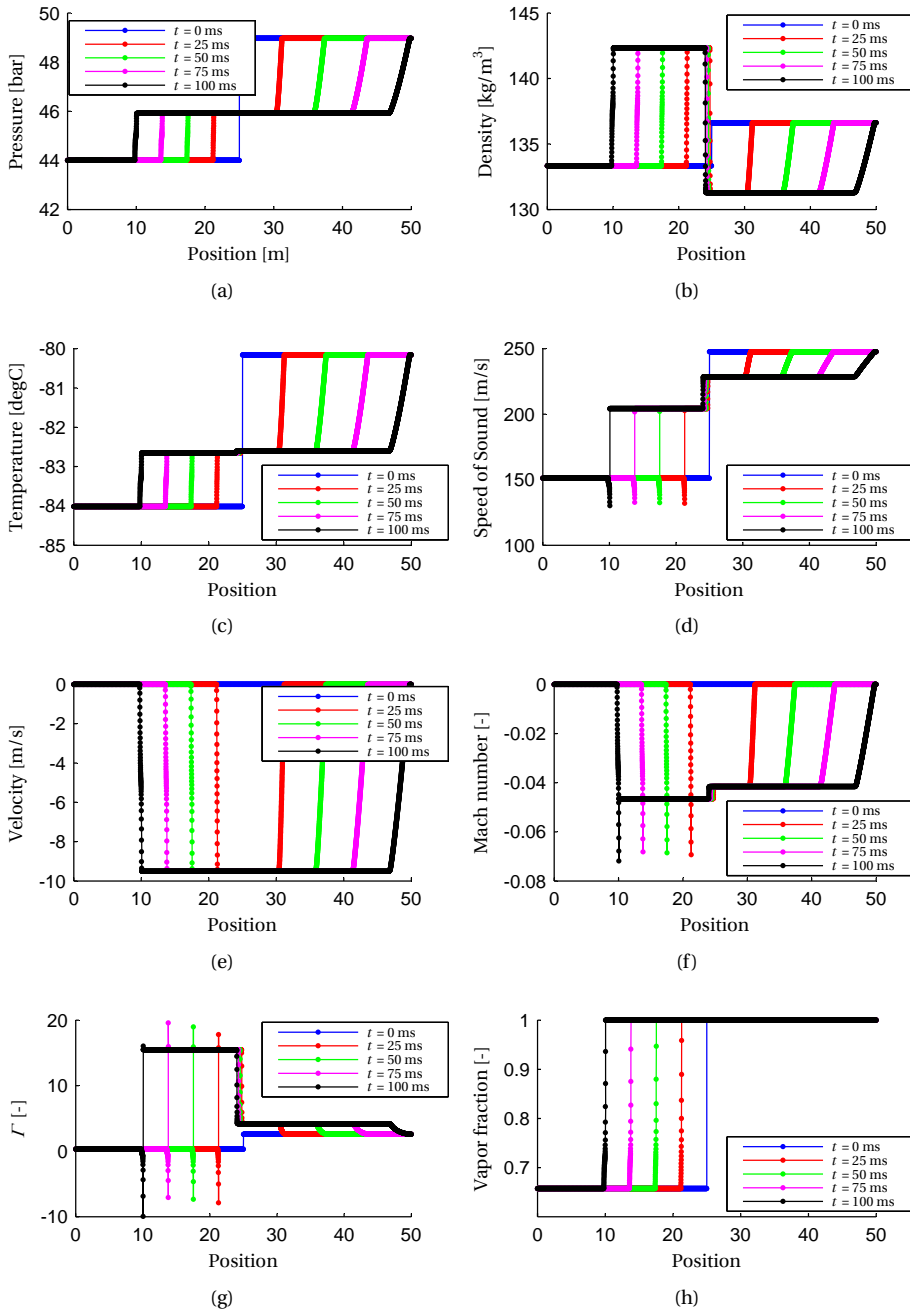


Figure 4.9: Simulation results of the mixed compression wave experiment in methane, displayed in the laboratory reference frame.



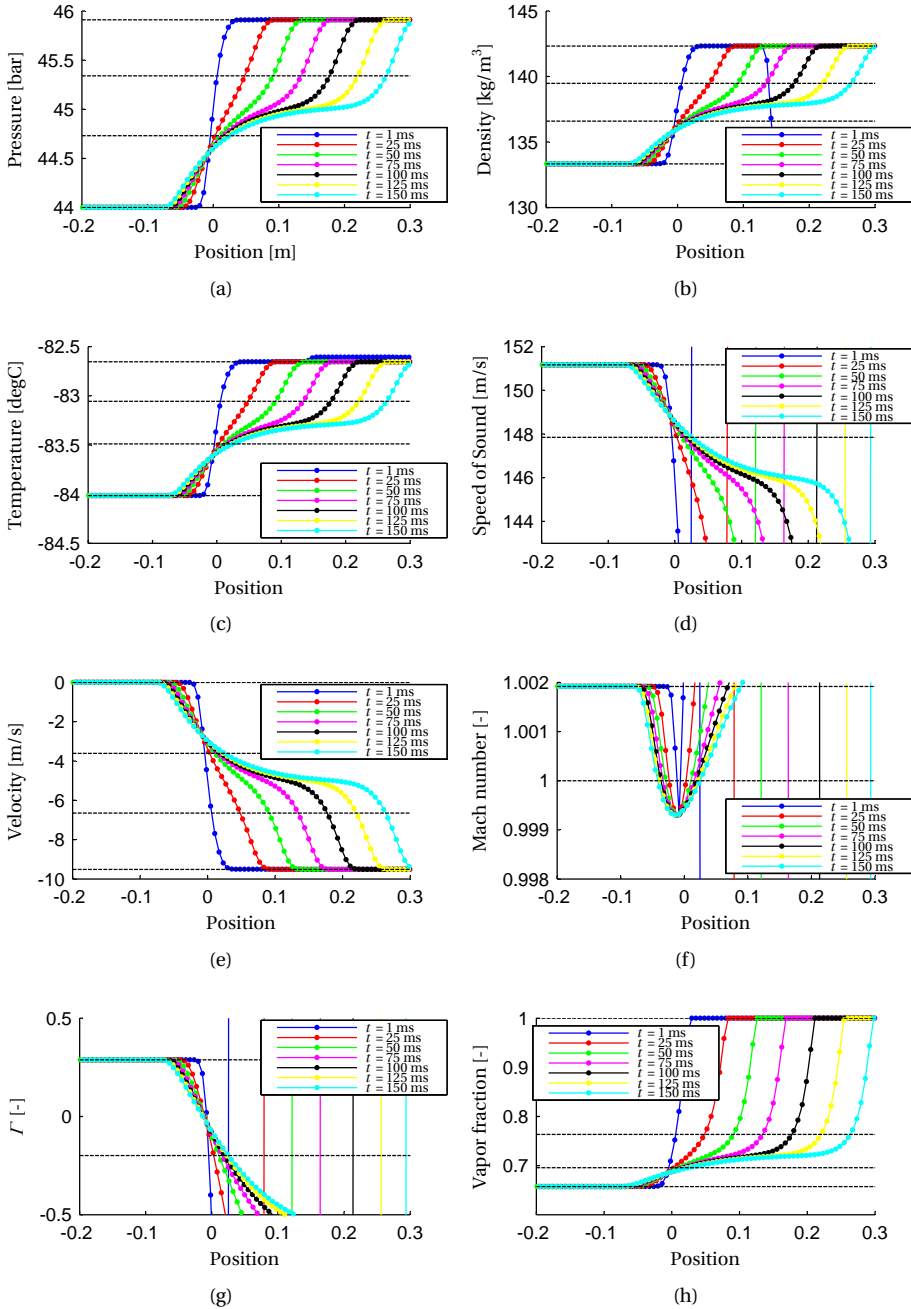


Figure 4.10: Simulation results of the mixed compression wave experiment in methane displayed in the shock reference frame of the first shock.

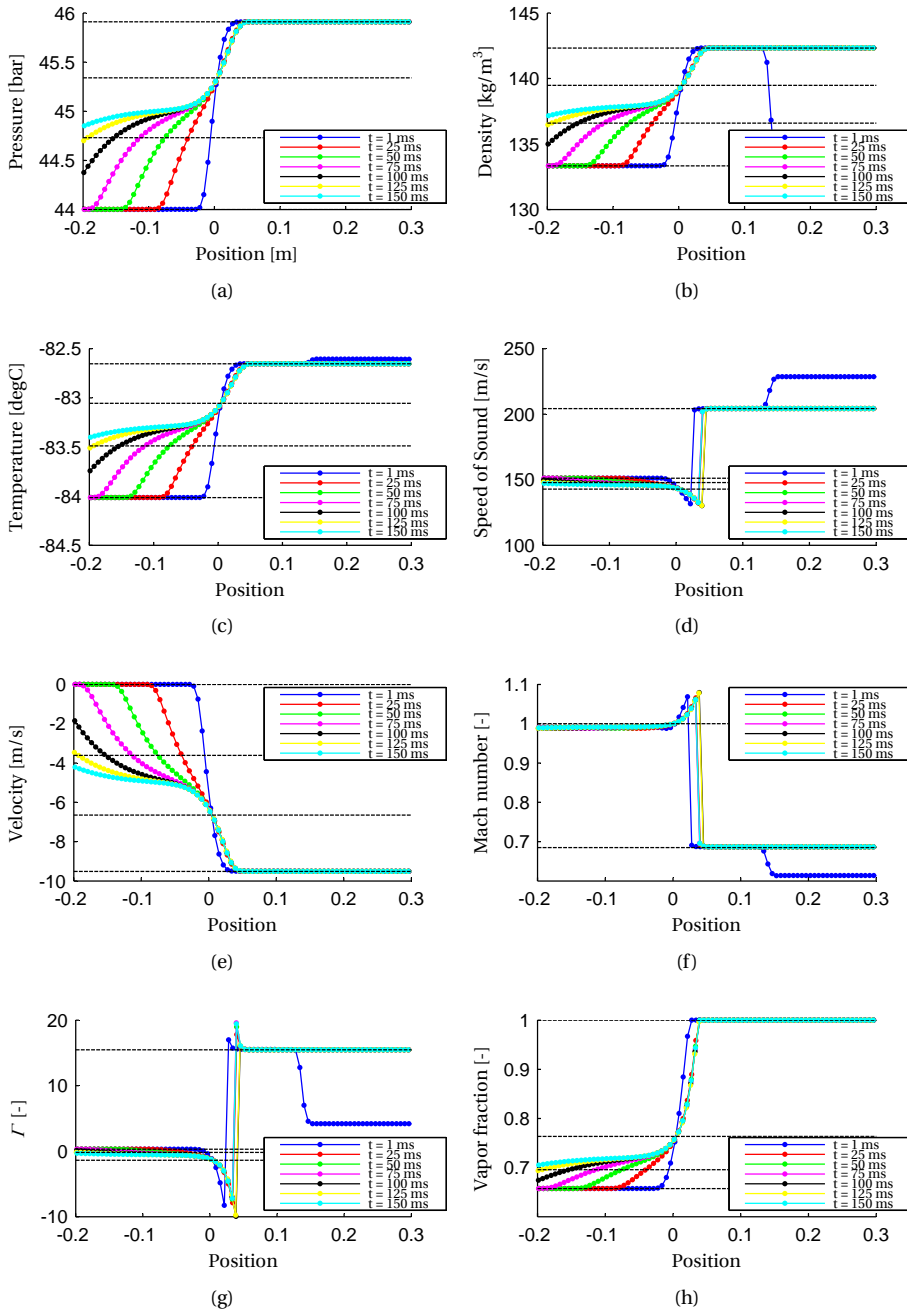


Figure 4.11: Simulation results of the mixed compression wave experiment in methane displayed in the shock reference frame of the second shock.

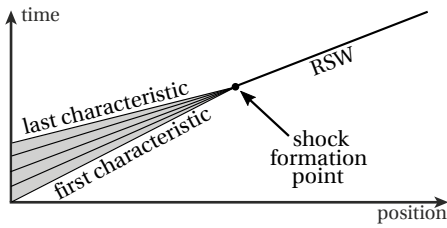


Figure 4.12: Position-time diagram of RSW formation with all characteristics merging in a single point.

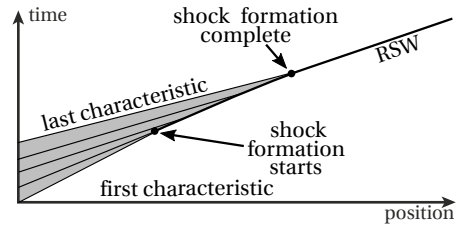


Figure 4.13: Position-time diagram of RSW formation over a finite space.

4

tion of the Riemann invariant in the homentropic region, the pressure, velocity and density profiles at this boundary are determined, which are referred to as the optimal profile. The profile for shock formation at 1 meter distance from the boundary is displayed in figure 4.14. The limiting characteristics are displayed in a position-time diagram in figure 4.15. To obtain an estimate of the maximum allowed opening time, the time difference between the first and last characteristic at the boundary is determined. The maximum opening duration for RSW experiments with post-shock conditions in the positive- $\Gamma$  region cannot be determined, since characteristics diverge in an expansion whenever  $\Gamma$  is positive. In that case, only an RSW can merge with the characteristics, under the condition that the shock propagation speed is higher than the local speed of sound. The opening time is calculated for a large number of experiments with pre-shock conditions throughout the thermodynamic domain featuring a negative of  $\Gamma$  and post-shock conditions at the same isentrope with a value of  $\Gamma$  equal to zero. Figure 4.16 shows the graph that can be obtained, displaying contours of the maximum allowed opening time for methane for a 1-m-long tube. Since  $\Gamma$  goes to  $-\infty$  at the critical point, characteristics merge faster at thermodynamic conditions close to this point, and higher maximum allowed opening times are found. A similar evaluation is conducted in case  $\text{CO}_2$  is used as working fluid, for which the resulting time estimate is displayed in figure 4.17. The opening time estimate scales linearly with the length of the facility, thus a long facility allows for a larger opening time. Multiplying this value with the length of the facility gives an estimate of the maximum facility-dependent opening time.

An RSW experiment is simulated, at which the shock forms at 1 meter distance. The pre-shock state is as reported by Nannan *et al.* [16] and the post-shock state is at the same isentrope with a value of  $\Gamma$  equals 0. The simulation results are displayed in figure 4.18. With the applied discretisation, the pressure gradient in parts of the simulation has a similar gradient as an RSW, such that no distinction is made between such an isentropic expansion and an RSW within the numerical model. Therefore, partial shock formation can be seen at 45.2 bar at  $t = 2.5$  ms. This partial RSW accelerates because of its supersonic nature, and increases its pressure difference. At  $t = 5$  ms, a pressure plateau is visible due to the acceleration of this partial RSW. At  $t = 7.5$  ms, the RSW is fully developed and does not change its waveform, as is visible at  $t = 10$  ms. Despite the formation of a partial shock, the prediction of shock formation at 1 meter distance is accurate, thus the calculated opening time of 0.17 ms is confirmed.

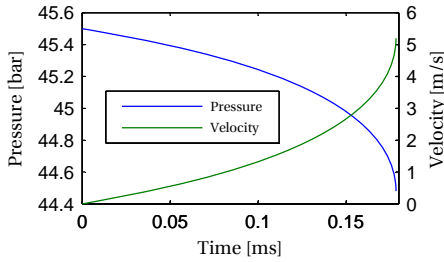


Figure 4.14: Profile of pressure and velocity in case all characteristics merge at 1 meter from the diaphragm for methane.

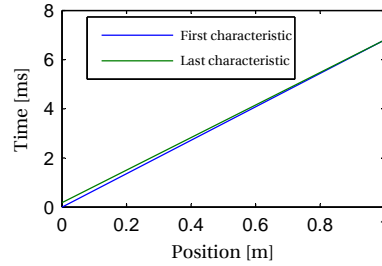


Figure 4.15: The first and last characteristic displayed in a position-time diagram of methane. All characteristics merge at 1 meter from the diaphragm

The calculated value of the opening time limitation is an optimistic estimate, because of the assumption that all characteristics merge in a single point, as displayed in figure 4.12. In reality, a shock will form over a small portion of the pressure difference first, which grows in strength until a full shock has developed, see figure 4.13. The partial shock formation alters the wave propagation speed, since it travels at supersonic speed, and consequently also alters the location at which the shock is fully formed. Thus the opening sequence of the diaphragm or valve determines the pressure profile as the wave emerges, which in turn influences the location and pressure level at which initial shock formation takes place. This has its effect on the time and location at which the shock is fully formed, altering the maximum opening duration. To investigate the influence of the opening pressure profile, a second simulation is performed with a different pressure and velocity profile at the boundary, which mimicks the pressure profile resulting from the opening of a valve or bursting of a diaphragm. The boundary pressure is chosen to be linear in time, and is referred to as the linear profile. All other parameters, such as total pressure drop, mesh size, time step, etc. are kept the same compared to the simulation in which the characteristics merge in a single point. The results are shown in figure 4.18, displayed in the laboratory, as well as and shock reference frame. The formation of the RSW initiates at thermodynamic states with a higher pressure, because  $T$  has its lowest value at that pressure. The RSW propagates at a supersonic Mach number, which increases as the pressure difference across the shock increases. The waveform still changes from 7.5 ms to 10 ms, which indicates that the shock has not been fully formed at that time instant. Consequently, a larger distance is required for the formation of the complete RSW.

#### 4.4.3. SIMULATION OF TRANSCRITICAL NONCLASSICAL FLOWS STARTING FROM SINGLE PHASE STATES

A shock tube experiment, designed for experimental validation of nonclassical NICFD phenomena, is simulated using  $\text{CO}_2$  as working fluid.  $\text{CO}_2$  is a non-toxic, easily obtainable and low-cost gas with a very high degree of purity. Its critical temperature is  $30.957^\circ\text{C}$ , which is close to ambient conditions, making the temperature easy to regulate accurately. The experiment is designed with the fluid in one compartment in supercritical conditions, and on the other in a subcritical vapour state, corresponding to state A1 and B1 in figure 4.21. Achieving

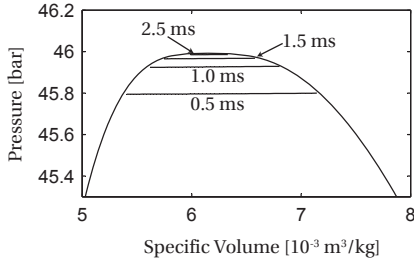


Figure 4.16: Maximum opening time in case all characteristics merge in a single point at 1 meter from the diaphragm for methane.

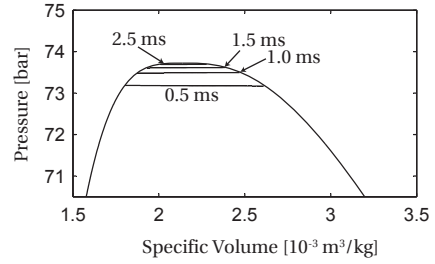
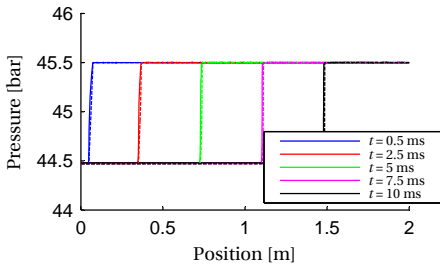
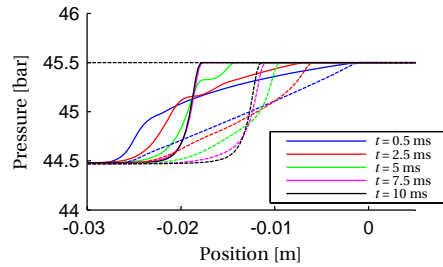


Figure 4.17: Maximum opening time in case all characteristics merge in a single point at 1 meter from the diaphragm for CO<sub>2</sub>.



(a) laboratory reference frame



(b) Shock reference frame

Figure 4.18: Simulation of shock formation. The continuous line shows the formation of a shock using a pressure profile at the boundary such that all characteristics merge at 1 meter distance, given in figure 4.14. The dashed line is the formation of a shock using a linear pressure profile at the boundary.

stable thermodynamic conditions could require a long time. Therefore, the initial states are chosen to be both in the single phase regime, such that no phase separation will occur during the preparation of the experiment. Moreover, the two states are on the same isotherm, such that no heat conduction takes place between the two regions, facilitating the control of the temperature. Upon connecting the two compartments, e.g. by breaking a diaphragm or opening a fast-acting valve, a rarefaction will travel into the high pressure state and a compression into the low pressure state, see figure 4.22.  $\Gamma$  is positive in the supercritical region, meaning that the wave propagation speed, defined as  $c - u$ , decreases in a rarefaction, and consequently the wave dilates and forms an isentropic rarefaction fan. However, as the pressure decreases below the saturation line, the two-phase region is entered. Across the saturation line, both  $\Gamma$  and the speed of sound display a discontinuity. The speed of sound is lower than in the single-phase region, such that the wave propagation speed, defined as  $c - u$ , is also lower.  $\Gamma$  is negative in the critical two-phase region, implying that the rarefaction in the two-phase regime will exhibit wave steepening, and thus form an RSW. Except for initial conditions A1 that are very close to the critical isentrope, the resulting RSW propagation speed is lower than the wave propagation speed of the limiting single-phase characteristic. The rarefaction then splits into a classical single phase rarefaction fan of the supercritical states and a nonclassical two-phase RSW. The flow between the rarefaction fan and the RSW is of uniform nature at exactly saturated thermodynamic conditions, in case instantaneous thermodynamic equilibrium is considered. Due to the possibility that the fluid reaches metastable states, this is unlikely to occur in reality.

A special case occurs in the very close proximity of the critical point. The slope of isentropic curves in the  $P$ - $v$  plane becomes very small, due to the low values of the speed of sound in the near-critical region. Exactly at the critical point, the compressibility diverges and the critical isentrope exhibits a horizontal tangent. As a consequence, in a limited region in the very close proximity of the critical point, the single-phase speed of sound is lower than the speed of a finite-amplitude RSW in the two-phase region and therefore the admissibility region extends into the single-phase supercritical region. The admissibility domain of RSW thus covers a part of the single phase region in the critical region. By connecting the pre-shock and post-shock states of double-sonic shock waves, the boundaries of the admissibility domain are obtained. For the fluids under study, which are  $\text{CO}_2$  and methane, the admissibility domain is calculated and presented in figure 4.19 and figure 4.20 respectively.

An example of a flow featuring an RSW starting in the supercritical region is given in table 4.2. State A1 and B1 are the initial conditions for the shock tube experiment for the high pressure and low pressure compartment respectively. The expansion will take place from state A1 to state A3. This will take place in an isentropic manner from state A1 to state A2, which are chosen to be on the critical isentrope. State A2 lies in the supercritical region, 35 Pa and 0.1 mK above the critical point. From state A2 to A3, the expansion takes place through an RSW. In the low pressure compartment of the shock tube, a compression will occur from state B1 to B2. The initial condition B1 is chosen such that the compression takes place within the vapour region only; no two-phase fluid states are found. Since  $\Gamma$  is positive in this region for the fluids under scrutiny, the compression takes place as a classical compression shock. Because initial state B1 was chosen to be within the range of validity of the thermo-

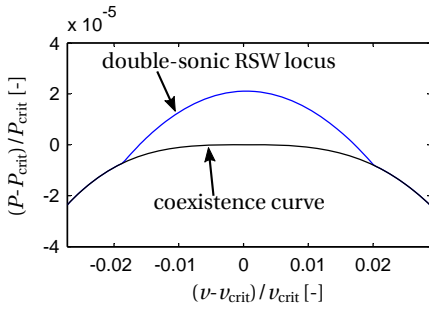


Figure 4.19: The upper bound of the calculated rarefaction shock region for CO<sub>2</sub>. By connecting the states from which a double-sonic RSW can form, the double-sonic RSW locus is formed, which bounds the region where RSW are feasible.

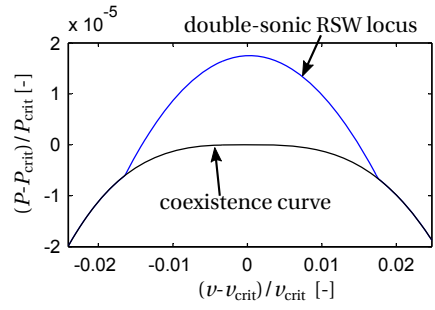


Figure 4.20: The upper bound of the rarefaction shock region for methane. By connecting the states from which a double-sonic RSW can form, the double-sonic RSW locus is formed, which bounds the region where RSW are feasible.

4

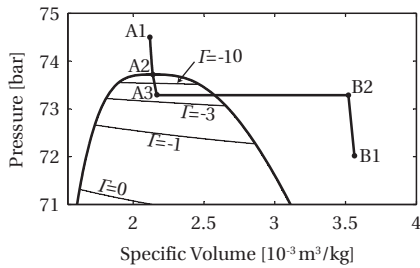


Figure 4.21: Pressure - specific volume diagram for CO<sub>2</sub> with some contour levels of  $\Gamma$ . Number A1 to A3 correspond to the left running wave, and B1 and B2 correspond to the right running wave. State A1 is chosen to be on the critical isentrope. State A2 is only 35 Pa above the critical point.

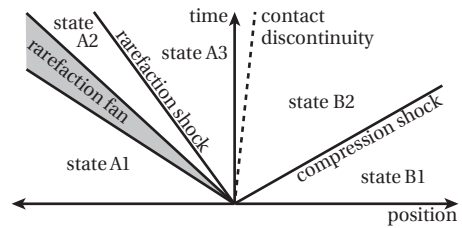


Figure 4.22: Pressure - specific volume diagram for CO<sub>2</sub> with some contour levels of  $\Gamma$ . Number 1 and 4 correspond to the left and right initial state respectively, and 2 and 3 correspond to the states after the waves have passed. In case state 1 is chosen to be on the critical isentrope, then that the last characteristic of the rarefaction fan and the rarefaction shock are merged.

dynamic model, the pressure difference between the states is not high enough to obtain a double-sonic RSW from state A2 to A3. Instead, only the pre-shock Mach number is unity, and the shock is of the pre-sonic type. Consequently, pre-shock state A2 is not located on the double-sonic locus, but between the double-sonic locus and the coexistence curve. The compression shock takes place in the vapour regime and since  $\Gamma$  is positive in this region for the fluid under scrutiny, a classical compression shock forms.

The simulation results are displayed in figure 4.23. Although initial state A1 is chosen to be exactly on the critical isentrope, there is a mismatch of state A2 with the theoretically calculated value. The region between the rarefaction fan and rarefaction shock has constant close-to-critical conditions of 969 Pa above the critical point, and a temperature of 5.7 mK above the critical point. Consequently, the wave propagation speed on the last characteristic of the rarefaction fan in the simulation is approximately 102 m/s, while the RSW travels at 82.8 m/s, thus wave splitting takes place. The reason for the mismatch with the theoretical

|                        | State | $P$<br>[bar] | $\nu$<br>[m <sup>3</sup> /kg] | $T$<br>[°C] | $\Gamma$<br>[-] | Ma<br>[-] | $q$<br>[-] |
|------------------------|-------|--------------|-------------------------------|-------------|-----------------|-----------|------------|
| Rarefaction shock wave | A1    | 74.50        | 0.00212                       | 31.413      | 12.14           | 1.000     | 1.00       |
|                        | A2    | 73.72        | 0.00214                       | 30.957      | 5917.36         | 1.000     | 1.00       |
|                        | A3    | 73.29        | 0.00217                       | 30.699      | -4.14           | 0.943     | 0.46       |
| Compression wave       | B1    | 72.00        | 0.00356                       | 31.413      | 0.95            | 1.006     | 1.00       |
|                        | B2    | 73.29        | 0.00352                       | 32.549      | 1.03            | 0.994     | 1.00       |

Table 4.2: Thermodynamic states of an experiment in CO<sub>2</sub> with state A1 on the critical isentrope. The rarefaction is isentropic and classical from state A1 to state A2, and through a nonclassical RSW from state A2 to A3. State A2 is close to the critical point, the pressure is 35 Pa and the temperature of 0.2 mK above the critical point. State B1 is on the same isotherm as state A1. The change from B1 to B2 is through a classical compression shock wave.

results is because the RSW features some overshoot at pre- and post-shock conditions, as is also shown in section 4.4.1. Small errors can result in large deviations in thermodynamic variables very close to the critical point. In this example the error is only 934 Pa, but it results in a large enough difference of the speed of sound for wave splitting to occur, instead of the expected pre-sonic RSW. In a physical experiment, it is unlikely to observe a pre-sonic RSW due to the small size of the supercritical admissibility region. However, measurement of a two-phase RSW seems certainly achievable.



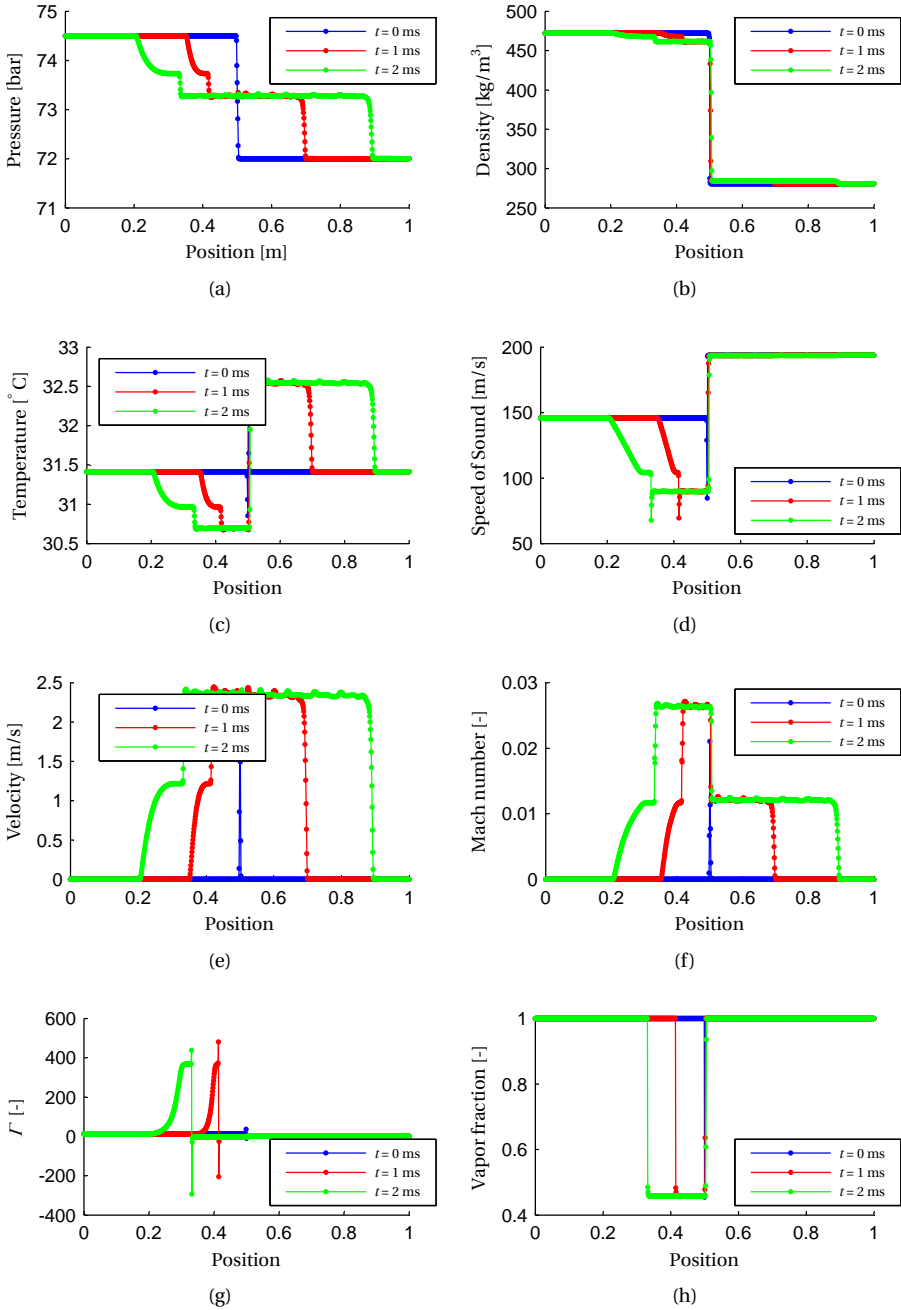


Figure 4.23: Shock tube flow in CO<sub>2</sub> of a left-running rarefaction featuring thermodynamic states along the critical isentrope, which forms an RSW in the two-phase region. The right-running compression takes place entirely in the vapour region.

## 4.5. CONCLUSION

For the numerical study of gasdynamic phenomena close to the critical point, a thermodynamic model based on scaling laws has been implemented into in-house software for the estimation of fluid thermodynamic properties. To this end, root-finding algorithms are developed and implemented to determine thermodynamic properties as a function of  $P$  and  $T$ ,  $P$  and  $\rho$ ,  $P$  and  $q$ ,  $T$  and  $\rho$ ,  $T$  and  $q$ , and  $\rho$  and  $e$ . Specifically the possibility of computing thermodynamic properties of a state with  $\rho$  and  $e$  as fixed variables is essential for performing computational fluid dynamic simulations of the Euler equations. Simulations are performed to validate the thermodynamic model and numerical solver based on theoretical estimations of an RSW and a mixed compression wave example, as described in literature [16].

A design of a shock tube experiment aimed at the generation and characterisation of non-classical vapour-liquid flow fields is made. The minimum time for the rupture of the diaphragm or the opening of the valve has been estimated for initial conditions with a thermodynamic state in the vicinity of the critical point. This estimate varies from several microseconds to more than 2.5 ms for a one-meter-long facility, dependent on the proximity to the critical point. The proposed experiment features initial states in the single-phase region on the same isotherm, greatly simplifying the technical solution to perform such an experiment. Wave splitting of the rarefaction into a classical expansion fan and a nonclassical RSW, which is predicted theoretically, is observed also in the simulations. If instantaneous thermodynamic equilibrium is assumed, the thermodynamic state of the flow between the rarefaction fan and the RSW is exactly at the saturation line. For rarefactions featuring thermodynamic states very close to the critical point, no wave splitting takes place. The reason is that the supercritical wave propagation speed will be lower than the RSW propagation speed. Thus it is theoretically possible to for an RSW to occur having single-phase supercritical pre-shock conditions. The admissibility domain of RSWs thus includes a very small single-phase region above the critical point, apart from a region encompassing a larger domain of thermodynamic states in the two-phase region.



# 5

## DYNAMIC MODELING OF ORC POWER SYSTEMS

Selected contents from:

Casella, F, Mathijssen, T., Colonna, P., van Buijtenen, J. Dynamic Modeling of Organic Rankine Cycle Power Systems. *J. Eng. Gas Turb. Power* 135, 042310, (2013), 12 pages.

### 5.1. INTRODUCTION

Turbomachinery of ORCs, a type of energy conversion system that employs as a working fluid an organic compound, e.g. a hydrocarbon or siloxane, is an already existing application that features NICFD flows. Using these type working fluids allows them to be efficient at a smaller scale than systems that employ water as working fluid. The low speed of sound in such fluids induces high Mach number flows in the expander, often supersonic. These flows induce shock waves, which are highly undesired effects in turbomachinery that reduce efficiency and can cause mechanical failure of components. The understanding of the fundamentals of NICFD flows aids to obtain more efficient designs of such components.

An upcoming challenge in the design of such systems is the optimisation for dynamic operation. Current conventional applications of ORC technology, namely electricity conversion from geothermal reservoirs, biomass combustion and heat recovery from stationary large reciprocating engines are not particularly demanding in terms of system dynamics and control. This scenario is bound to change when new, very promising uses of ORC power systems will gain momentum. A considerable research and development effort is currently focused on the development of smaller systems (from a few to tens of kW<sub>e</sub>) for applications like distributed concentrated solar power conversion, and automotive heat recovery. A possible model for the development of electricity generation in remote areas of the world also demands for dynamic power systems capable of island operation and, at the same time, of exploiting renewable fuel, like biomass from agricultural and forest residues. ORC systems are also uniquely positioned in this respect.

Physically based dynamic models of ORC systems are at the foundation of a design process which accounts for dynamic requirements from the very beginning. Dynamic simulations can be used to support system configuration and the choice of the equipment during the design phase, to develop and test control strategies, to support the detailed design and tuning of the control system, and also to support system commissioning, operation, maintenance and revamping.

For these reasons, the development of lumped parameters dynamic models of ORC systems recently received attention. Wei et al. [83] describe a dynamic model that has been used in the development of a 250 kW<sub>e</sub> ORC turbogenerator for heat recovery applications, which is now commercially available. The validity of the model is partially tested, by comparing simulation results to actual measurements performed on a prototype. The performance of a system model adopting a moving boundary model of the evaporator is compared to another version of the model in which the evaporator is modeled by means of a one-dimensional discretization. The moving-boundary model proved superior in terms of computational speed and it is less complex. Quoilin et al. [84] more recently numerically investigated different control strategies for a small ORC generator adopting a volumetric expander. Also in this case the working fluid is refrigerant R245fa, and the described dynamic model has been developed in a similar manner by resorting to the Modelica modeling language.

From a more general perspective, dynamic modeling of energy systems based on Rankine cycles using water as a working fluid has a much longer tradition. The interested reader can refer to the two-part article by Colonna and van Putten [85, 86] for a compendium of modeling techniques used in this field. Many of the relevant physical phenomena occurring in steam power plants are the same as in ORC systems, and the development of dynamic models of steam power plants is at the basis of ORC system modeling.

This study stemmed from the need of upcoming projects targeting small ORC turbogenerators for tackling demanding challenges related to system dynamics. In order to profit from the use of dynamic simulations, models must be thoroughly validated, and Tri-O-Gen made available for dynamic testing one of its 150 kW<sub>e</sub> units based on high-speed technology and adopting toluene as the working fluid. All the phenomena characterizing the system's dynamic, namely fluid flow and thermal inertia in the heat exchangers, fluid phase transition, shaft inertia, etc., are common, apart from scale, to other systems with similar configuration, therefore the validated model can be used for further engineering studies on new systems of different capacity and adopting other working fluids. These new developments are related to the design of small ORC turbogenerators for solar and heat recovery applications.

This chapter is structured as follows: first the requirements for the modeling are defined in section 5.2. Then a sample case is selected and explained in section 5.3. The developed Modelica model is described in section 5.4 after which the validation of the model including the experiments and the results are described in section 5.5. Some highlights of the possibilities with such a validated model are elaborated in section 5.6. Finally some concluding remarks are given in section 5.7.

## 5.2. MODELING METHODOLOGY

In this section, the requirements of a dynamic modeling environment for ORC power systems are stated. Subsequently, it is shown how the requirements have been met, by using object-oriented modeling methodologies and by effectively re-using prior work in this field.

### 5.2.1. REQUIREMENTS

The main goal of the work discussed in this chapter is to provide an environment and a methodology to test the dynamic response of ORC power systems for stationary electricity generation applications, such as industrial waste heat recovery, off-grid biomass exploitation and solar-thermal plants, as well as heat recovery from mobile reciprocating engines (e.g., prime movers of trucks, ships and trains).

Nonlinear dynamic models based on first principles are thus needed, in order to describe systems that might not yet exist. The aim is to describe the system-level behavior, stemming from the interaction of the system components, rather than focusing on the detailed behavior of single components, which belongs to the realm of CFD and FEM models; therefore, zero-dimensional or one-dimensional models of the components are considered, possibly obtained from detailed 3D analysis performed with other tools, or by fitting the models to experimental data, if available.

The modeling approach must be fully modular, i.e., the system model can be assembled by connecting component models through interfaces representing physical boundaries. Ideally, arbitrary component connections should be possible, as long as they make sense from a physical point of view.

System models should be easily reconfigurable, in order to adapt the degree of detail throughout the project lifetime. During the preliminary design stages, few details are available and coarse models are often used, providing a quick assessment of design alternatives. Later on, the models might be refined in order to assist the detailed engineering phases, and finally they might be tuned with experimental data to support the improvement of the controllers, possible revamping activities, etc.

Reusability and extensibility are essential features of effective modeling environments. On the one hand, there are many commonalities between different projects, so it should be possible to re-use and maintain models that have already been developed, tested and validated during previous projects; on the other hand, it should be as easy as possible to adapt existing models to new needs, or to develop new ones from scratch when required, thus constantly enlarging the scope of the model library.

Last, but not least, although the typical use of such dynamic models is the numerical simulation of transients, it might be very useful if they could also be used for other purposes, such as model-predictive control, diagnostics, optimization, etc.

### 5.2.2. OBJECT-ORIENTED MODELING

Most of the requirements stated in section 5.2.1 are satisfied by adopting an equation-based, object-oriented modeling language such as Modelica [87–89].

First-principle, 0-dimensional and 1-dimensional elemental models can be written directly in terms of differential-algebraic equations; these relate the internal variables among each other and with the variables of the physical ports through which the models can be connected to each other. The physical ports are a-causal, and the connection between two ports corresponds to additional equations relating the corresponding variables, which are added to the set of the component equations, e.g., stating that pressures are equal and that the entering mass flows sum to zero. Adapting these models or writing new ones when needed is straightforward, as the modeling code is very close to how the models are written on paper, and all the burden of solving those equations is shifted from the modeler to the modeling tool.

5

At a higher level, device models and plant models can be built by hierarchically connecting lower-level models, which can be done through the metaphor of object diagrams, using graphical user interfaces, see, e.g., [90, 91]. The Modelica tool then expands all the models and uses sophisticated symbolic and numerical techniques to solve the corresponding differential-algebraic equations and generate efficient simulation code (see [92] for a comprehensive review). The use of such techniques allows the modeller to concentrate on a high-level, declarative mathematical description of the process, while still obtaining simulation code that can be as fast (or faster) as custom-written C or FORTRAN code.

System models can be made highly reconfigurable by means of replaceable components, sharing the same interface. For example, a condenser model has four thermo-fluid ports, two for the inlet and outlet of the condensing fluid, and other two for the inlet and outlet of the cooling fluid. Many different models can be built using this interface, either representing the same physical device with different levels of accuracy, or representing different devices (e.g. a plate rather than a shell-and-tube heat exchanger). All these models can be used in the same place, as they interact with the rest of the system through the same interface. Modelica features powerful mechanisms to manage families of models that can be built by redeclaring parts of a basic model; refer to [93] for an example in the field of nuclear power generation.

Last, but not least, Modelica is a non-proprietary modeling language, which is supported by multiple simulation tools. This has two main advantages: on the one hand, the investment in modeling is not tied, at least in principle, to a specific proprietary simulation software; on the other hand, different tools might be better at one task than at another (e.g.: batch simulation, generation of real-time simulation code, dynamic optimization, etc.), so one might use the same model code with different tools to perform different model-related activities.

### 5.2.3. MODEL RE-USE

The work presented in this chapter was not developed from the grounds up, but rather built on pre-existing foundations, which allowed to reduce the model development time, and to

exploit tested and validated modeling code.

Most of the basic components required for the modeling of ORC power systems were already available in the ThermoPower Modelica library for the dynamic modeling of power plants and energy conversion systems [94, 95]. ThermoPower has been developed at Politecnico di Milano since 2002, and was originally designed to model conventional steam power plants; however, the working medium models (steam, flue gases, fuels, or air) are not directly embedded in the component equations, but are rather represented as replaceable objects. Modeling ORC systems thus mainly required to write an instance of such object to compute the properties of organic fluids, compatible with the interface defined in the Modelica standard library [96], and using an external program to compute the fluid properties [54]. The modelling assumptions made when developing the components using water or steam as a working medium (e.g., single-phase, one-dimensional turbulent flow or two-phase, one-dimensional homogeneous flow for heat exchanger elements, almost incompressible flow for pump models and liquid-handling valves) are in fact not specific for H<sub>2</sub>O and keep their validity also for organic fluids. Therefore, it was possible to obtain the corresponding models for organic fluids just by redeclaring the working fluid model.

In some cases, further adaptations were needed. For example, ThermoPower provides turbine models based on Stodola's law, which are suitable for multi-stage axial turbines such as those typically found in large power plants. ORC turbines usually have few stages (or even one single stage), and operate with choked first-stage nozzles in almost all conditions, therefore the flow model had to be modified, assuming an isentropic transformation in the nozzle with sonic flow conditions in the throat.

The Modelica code implementing the turbine equations is shown as an example in Table 5.1; note how the code is not a sequence of variable assignments (as in the case of FORTRAN or C code), but is rather a declarative collection of possibly implicit equations, whose writing order is arbitrary, and which are written independently from the solution strategy.

One of the results of this work is hence a new library of reusable models, derived from existing ones, including all components typically used in ORC power systems, whereby any pure fluid of the rich external fluid thermodynamic property library can be selected as working medium. The Modelica library for ORC power systems features models of heat exchangers (including condensers), valves, turbomachinery (pumps, turbines), and phase separators. Cooling circuits and flue gas circuits can be assembled by using components from the ThermoPower library.

### 5.3. CASE STUDY: A 150 kW<sub>e</sub> HIGH-TEMPERATURE TURBOGENERATOR

In order to provide a thorough validation of the ORC power systems Modelica library, the Tri-O-Gen high-temperature turbogenerator has been modeled and dynamic simulations have been compared to ad-hoc conceived experiments. The model covers the normal operating conditions of the system, both in design and off-design conditions; start-up and shut-



```

steam_in = Medium.setState_ph(pin,hin);
hiso = Medium.isentropicEnthalpy(pout, steam_in);
hin - hout = eta_iso * (hin-hiso) "Computation of outlet enthalpy";
sin = Medium.specificEntropy(steam_in);
  hin = ht + 1/2*ct^2;
  ht = Medium.specificEnthalpy(Medium.setState_ps(pt,sin));
  ct = Medium.velocityOfSound(Medium.setState_ps(pt,sin));
  rhot = Medium.density(Medium.setState_ps(pt,sin));
  w = rhot * At * ct;
  Pm = eta_mech * w *(hin-hout) "Mechanical power from the steam";
  Pm = - tau * omega "Mechanical power balance";
  u = D/2 * omega;
  Phi = (hin-hiso)/(u^2);
  eta_iso = (a[1]*Phi^2 + a[2]*Phi + a[3]);

// Mechanical boundary conditions
shaft_a.phi = phi;
shaft_b.phi = phi;
shaft_a.tau + shaft_b.tau = tau;
der(phi) = omega;

// steam boundary conditions and inlet steam properties
pin = inlet.p;
hin = inStream(inlet.h_outflow);
hout = outlet.h_outflow;
pout = outlet.p;
w = inlet.m_flow;

inlet.m_flow + outlet.m_flow = 0 "Mass balance";

```

Table 5.1: Modelica code of the turbine equations

down conditions are beyond the scope of the model. The validity of the results is deemed quite general, therefore covering different system configurations, working fluids and power capacities, because the physical phenomena occurring in ORC components are mostly the same in all these cases. A schematic overview of the considered ORC power plant, implementing a regenerative cycle with slightly superheated and subcritical turbine inlet, is given in figure 5.1. Both recuperator and condenser are heat exchangers of the shell and plate type.

A peculiarity of the Tri-O-Gen system is that the main pump, the turbine and generator are all mounted on the same shaft [97]. Lubrication of the hydro-dynamic bearings and cooling of the electrical generator is performed with the working fluid. The whole assembly can therefore be hermetically sealed. A boost pump is needed to supply sufficient pressure in the lubrication circuit.

During normal operation, the system is provided with two main loops controlling turbo-pump speed and the turbine inlet temperature. The turbo-pump speed is controlled by the

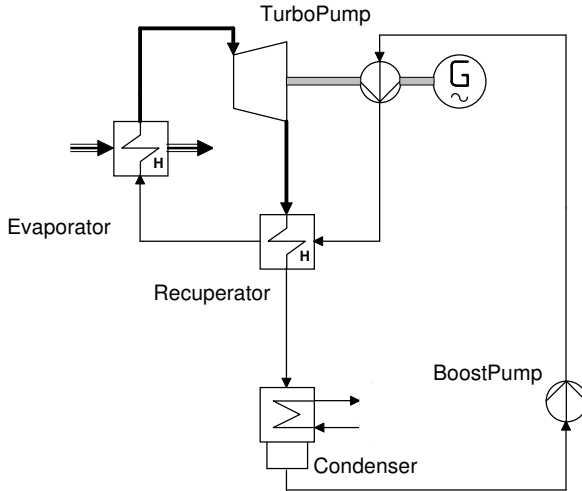


Figure 5.1: Simplified process flow diagram of the Tri-O-Gen ORC power plant.

AC/AC power converter, which turns the variable-frequency electrical power coming from the high-speed generator into 50 Hz, three-phase power suitable for grid connection. The turbo-pump speed set point, which determines the mass flow-rate of the pump, is then used to control the turbine inlet temperature (TIT), by means of a proportional-integral (PI) regulator.

The turbo-pump, the condenser and the recuperator are included in the standard module, while the evaporator design can be adapted to different energy sources. Note that different evaporators imply a different plant-wide dynamics, which in turn require re-tuning of the control system.

## 5.4. SYSTEM MODEL

### 5.4.1. MODEL MODULARITY

The top-level Modelica interface of the plant model is shown in figure 5.2. Starting from the left and going clockwise, it is possible to recognize the evaporator, with flue gas source and exhaust, the piping to the turbine, with the TIT sensor, the turbo-pump model connected to the electrical generator via a mechanical port, the recuperator, the condenser and the boost pump. The additional components connecting the main pump inlet to the recuperator hot inlet and to the condenser represent the flow of pressurized liquid toluene used for the turbo-pump lubrication: a small fraction of this stream leaks to the turbine outlet, and is mixed to the turbine exhaust vapour, while the most of the lubrication liquid flows directly to the condenser. All graphical connections correspond to connection equations, which are balance equations appropriate for the physical domain: same flange angle and torque balance for the mechanical connections, in grey; same pressure, mass balance and

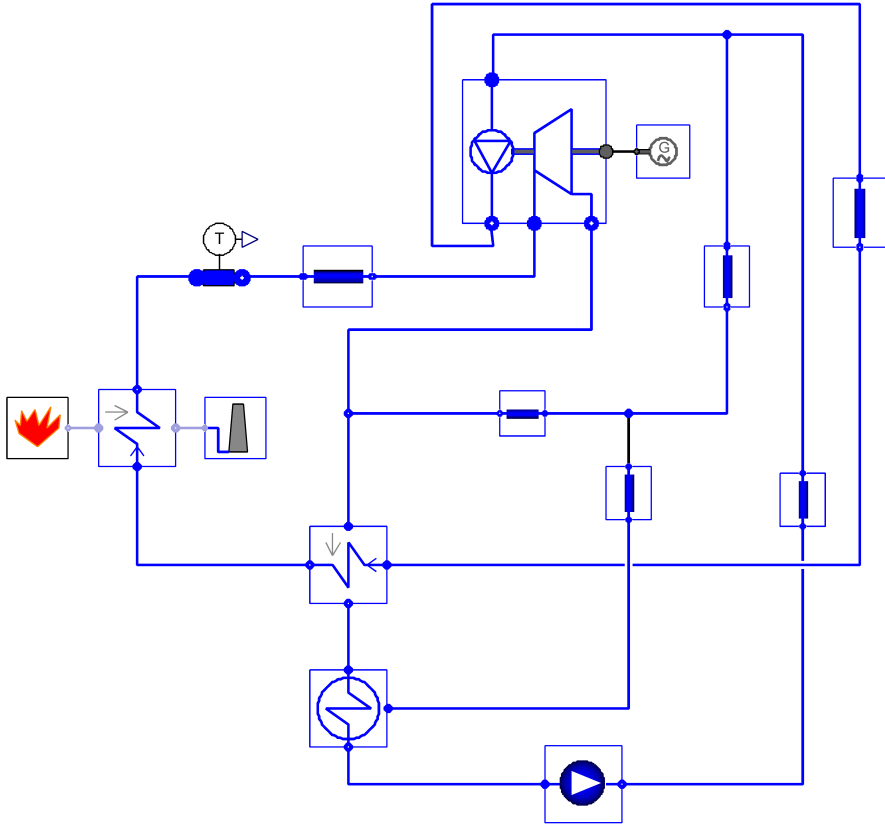


Figure 5.2: Top level object diagram of the Modelica model of the Tri-O-Gen ORC system.

energy balance for the thermo-fluid connections, in blue for the organic fluid and in light grey for the flue gas (see [98] for more details).

The above-described diagram is a framework for a potentially large number of actual plant models, where each component can be implemented in different ways keeping the same interface to the outside worlds (i.e., the same connectors). The actual component models making up the system model of the Tri-O-Gen unit, which has been validated within this work, are detailed out in the following sections.

#### 5.4.2. TURBO-PUMP AND ELECTRICAL GENERATOR MODELS

The turbo-pump model is obtained by connecting the turbine model and the pump model via their mechanical shaft connectors, see figure 5.3. The pump model, taken from the ThermoPower library, is based on a head-volume flow curve which is adjusted for the rotational speed by means of the geometric similarity equation; constant isentropic efficiency is assumed for simplicity and for lack of detailed information on the component.

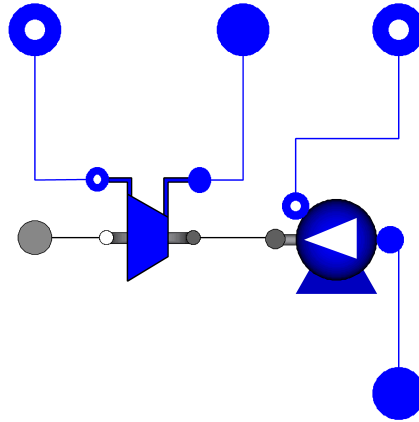


Figure 5.3: Object diagram of the turbo-pump component.

As far as the turbine model is concerned, the flow equations assume an isentropic expansion from the inlet to sonic conditions at the nozzle throat in the stator; the isentropic efficiency is assumed to be a quadratic function of the ratio  $\Phi$  between the isentropic inlet-outlet enthalpy difference and the squared tangential velocity of the rotor blades (see Table 5.1). This function has been tuned in order to obtain a good system-level prediction of steady-state operating conditions at the reference load level, and also at reduced load.

The electrical generator model features a mechanical rotational connector, representing the shaft, and models the electrical generator, and the interface to the grid. For the scope of this work, the actual details of the AC/AC frequency converter and of the turbogenerator speed control are not of interest, since the speed controller is known to operate well and has a much shorter response time than the thermal dynamics of the plant. A trivial model is therefore implemented, whereby the shaft speed is prescribed to be equal to the speed set point input. In case the design of such a controller is of interest, it would be possible to replace this model with a more detailed one, taking into account the shaft inertia, and a suitable representation of the power electronics of the frequency converter.

### 5.4.3. EVAPORATOR

The evaporator, see figure 5.4, is described by the connection of several sub-components, exchanging heat through their 1D thermal ports, shown in orange in the figure: 1D flow models (top and bottom of the diagram), 1D convective heat transfer models and a 1D tube wall model (center of the diagram). A further component swaps the direction of one of the temperature and heat flow distributions, in order to model counter-current flow. The flow models, taken from the ThermoPower library, contain one-dimensional dynamic mass and energy balance equations, discretized by the finite volume method, and static momentum balances, lumped at both ends of the component, and accounting for friction losses. Given the relatively low temperature of the flue gas, only convective heat transfer is considered.

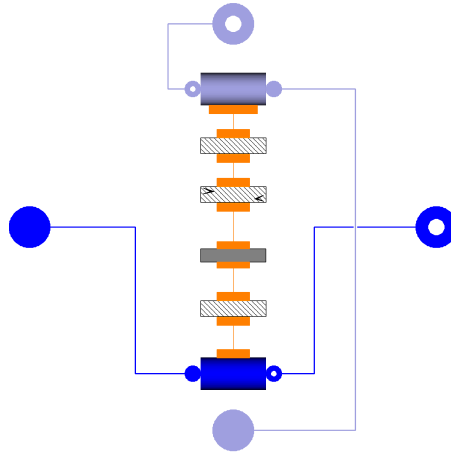


Figure 5.4: Object diagram of the evaporator component.

5

The heat transfer coefficient between the gas and the outer pipe surface is much lower than the one between the inner pipe surface and the toluene flow, so that heat transfer is dominated by the former phenomenon, while the toluene temperature is always quite close to the inner surface temperature of the pipe. It is then important to accurately model the gas-wall heat transfer coefficient, also in off-design conditions; for this reason, the heat transfer coefficient is given by

$$\gamma = \gamma_0 \left( \frac{w}{w_0} \right)^n, \quad (5.1)$$

where  $\gamma$  is the heat transfer coefficient,  $w$  the mass flow rate,  $n$  is a suitable exponent, and the subscript 0 refers to the value at nominal operating conditions. The wall-toluene thermal interaction is instead described by specifying a sufficiently high constant heat transfer coefficient. The pipe wall is also modeled with a 1D dynamic heat balance equation, discretized by finite volumes, neglecting thermal resistance in the radial direction and thermal diffusion in the axial direction.

Alternative model structures can be employed for this component (e.g., moving boundary models), but they are not treated here for the sake of conciseness.

#### 5.4.4. RECUPERATOR

The recuperator is a shell-and-plate heat exchanger. The temperature and heat flux distributions are two-dimensional; however, using 2D discretized models would considerably increase the number of state variables, without substantially increasing the accuracy of the system simulations. Therefore, the recuperator has also been modeled by the counter-current connection of 1D elemental components, much as the evaporator, see again figure 5.4. Equation 5.1 is used for both the hot and the cold side, with coefficients tuned in order to match the outlet temperature in on- and off-design steady operating points. Note in passing that if the purpose of the model was to evaluate alternative equipment, it would have also been

possible to use other correlations, relating the heat transfer coefficient to the geometrical features of the component.

#### 5.4.5. CONDENSER

Two models of the condenser are considered in this study. If the condenser cooling circuit is operated in such a way that the condenser pressure (and therefore also the temperature) is nearly constant, then the component can be trivially modeled as a fixed pressure sink attached to the turbine exhaust and lubricant discharge connectors, and a fixed pressure and temperature source attached to the boost pump connector. This turned out to be a sound choice for one of the experimental setups used for the model validation (see section 5.5.1), in which the condenser pressure is actually controlled. In the other experimental setup, the condenser cooling circuit is operated with a constant water flow, therefore the condenser pressure and temperature decrease significantly when the plant is operated at partial load. In order to accurately simulate this situation, a condenser model explicitly computing the condensing heat transfer between the cooling water flow and the toluene flow has been implemented.

#### 5.4.6. LUBRICATION CIRCUIT AND OTHER PIPING

The lubrication circuit is modeled by means of components representing pressure-dependent leakages, drawing cold toluene from the boost pump outlet and injecting it at the turbine outlet (for a very small amount) and at the condenser inlet (for the most part). The flow coefficients have been tuned in order to match some steady-state values that were obtained from previous studies of the system. Note that these component models affect mostly the computation of the boost pump flow, since the lubricating flow is about 30 % of the total flow through that pump. From an energetic point of view, the lubrication circuit recycles cold fluid from and to the condenser, hence it has only a minor impact on the energy conversion process, and on its dynamics.

The pipe connecting the evaporator outlet to the turbine inlet also has to be modeled explicitly, since there is a difference of several degrees between the temperatures at the two endpoints. The exact source of this discrepancy is still under investigation, as it cannot be fully explained by convective heat loss to a fixed temperature sink; it is probably due to some thermal interaction with nearby components. For the sake of the validation described here, assuming a fixed thermal power drawn from the flowing toluene vapour turned out to be more than adequate to provide a good match with the experimental data. Mass and energy storage in the pipe are also accounted for by a lumped-parameter volume model, since the length of the pipe is non-negligible, as it has to connect an externally built evaporator unit to the core ORC module.

#### 5.4.7. WORKING FLUID

Thermodynamic and transport properties of toluene are computed with an accurate multi-parameter equation of state model [99], and correlations implemented in an external software library [54, 72], accessible via the ExternalMedia Modelica library.

#### 5.4.8. CONTROL SYSTEM

A perfect turbo-pump speed control is assumed in this study. The system model can instead be used to describe, among other things, the dynamics which is relevant for the control of the turbine inlet temperature. As already mentioned in section 5.3, the turbine inlet temperature is controlled by a PI regulator acting on the turbo-pump speed. The temperature set point is chosen in order to obtain slightly superheated conditions at the turbine inlet, while avoiding high temperatures which might lead to thermal degradation of the working fluid.

Two categories of system models were developed: open-loop and closed-loop. In the open-loop model, the field measurements of the turbo-pump speed are directly used as inputs, while the closed-loop model incorporates the PI controller and computes the turbo-pump speed as an internal variable.

#### 5.4.9. OUTLOOK

The system model described in section 5.4 is focused on the modeling of a specific ORC system, i.e., the Tri-O-Gen ORC turbogenerator, under the particular working conditions for which measurements of transients are available for validation. It is however worth stressing the flexibility of the modeling approach.

First of all, the components developed and validated for this specific application (pumps, turbines, heat exchangers) can be readily re-used in other contexts, such as solar or automotive applications. Changing the model of the working fluid only requires a single class to be redeclared at the top level of the model; this can also be used for parametric studies during preliminary design, when the fluid itself has to be selected among several options. Heat exchangers implementing different flow configurations can also be treated in a similar manner.

Another crucial point worth mentioning is the way Modelica allows to manage model variants. In the case under scrutiny, for example, the core ORC module features a standardized design, while the evaporator is customized based on the specific thermal energy source. In order to model different cases, it is then possible to declare a new system model with a specific evaporator using this construct:

```
model PlantForCustomerX
  extends StandardPlant(redeclare EvaporatorModelXYZ evaporator);
end PlantForCustomerX;
```

Note how this is fundamentally different from making a copy of the original ORC system model, and changing the evaporator model for that copy. If the model of the core ORC module is later improved, e.g., by extending its validity range towards partial load operation, or by updating it to better reflect the results of a more extensive experimental validation campaign, all model variants previously derived from it by a copy mechanism will also have to be updated manually, which becomes impractical as the number of variants grows. Using the proposed approach, the model modifications need only to be applied once to the StandardPlant model, and they will be automatically inherited by all models derived from it by redeclaring some components.

Another advantage of the proposed approach is that the difference between the base model and the derived model is immediately apparent from the code, while in the case of modified

copies, differences are usually scattered in many places and might be hard to track afterwards.

## 5.5. VALIDATION

In this section the validation of the Tri-O-Gen ORC system model is illustrated. The experimental setup is described in section 5.5.1. The performed experiments are treated in section 5.5.2, while the corresponding simulations are explained in section 5.5.3. Finally, the comparison of the experimental data with the simulations is outlined in section 5.5.4.

### 5.5.1. EXPERIMENTAL APPARATUS

Measurements were recorded at two locations: one at the Tri-O-Gen test stand and the other one at a plant operating at a customer's site. At the test stand, natural gas is supplied at a maximum available rate of approximately  $110 \text{ m}^3/\text{h}$  to a burner. Cold ambient air is mixed with the combusted natural gas to reduce the flue gas temperature to a level acceptable for the evaporator (approximately  $500^\circ\text{C}$ ). Thermal energy is extracted from the ORC system by a mixture of water and glycol, which is supplied at constant flow rate to the condenser. All other components are standard and form the Tri-O-Gen ORC module, as described in section 5.3.

The second data set is taken from a plant operating as a bottoming cycle of two stationary diesel engines. The exhaust gas of the diesel engines has a temperature of approximately  $450^\circ\text{C}$ , and is supplied at a constant flow rate to the evaporator. In this case, the cooling system is controlled in order to keep a constant working fluid pressure in the condenser.

Both plants feature the same measurement equipment at the same locations within the system, as summarized in table 5.2. Temperature measurements are taken with Wika TR-10C transmitters and pressure measurements are taken with Wika IS-20S pressure probes. Both pressure and temperature measurements feature an estimated accuracy of 0.5 %. The electrical power output is measured with a Merlin Gerin PM500 power meter with an accuracy of 1 %. The turbo-pump rotational speed is obtained from the AC/AC frequency converter, which also acts as speed controller. Data are acquired at a frequency of 1 Hz at the Tri-O-Gen test stand, while at the customer's site, data are sampled at a lower frequency of 0.1 Hz. The mass flow through the turbine is determined based on turbine inlet temperature and pressure, by assuming quasi-1D isentropic choked flow through the turbine nozzle, and the needed toluene properties are calculated with the accurate thermodynamic model [99].

### 5.5.2. MEASUREMENTS AND EXPERIMENTS

The validation is based on two sets of experiments, both starting from steady-state operation. In the first experiment, performed with the test-stand unit, the turbine inlet temperature set point is changed stepwise, while the heat load is kept constant. The control system reacts by adjusting the rotational speed of the pump in order to change the mass flow through the ORC system until the desired temperature is reached. Neither the flue gas flow to the evaporator, nor the cooling water flow are modified during the transients. Two step changes of  $7^\circ\text{C}$ , one upward and one downward, are applied while the gas burner is firing at



| Section     | Place                | Type             |
|-------------|----------------------|------------------|
| Evaporator  | Toluene Inlet        | Temperature      |
|             | Toluene Outlet       | Pressure         |
|             |                      | Temperature      |
|             | Flue gas Inlet       | Temperature      |
|             | Flue gas Outlet      | Temperature      |
| Turbopump   | Turbine Inlet        | Pressure         |
|             |                      | Temperature      |
|             | Turbine Outlet       | Pressure         |
|             |                      | Temperature      |
|             | Pump Outlet          | Pressure         |
| Recuperator | Vapour Outlet        | Temperature      |
|             | Liquid Inlet         | Temperature      |
| Condenser   | Toluene Outlet       | Pressure         |
|             |                      | Temperature      |
|             | Cooling Water Inlet  | Temperature      |
|             | Cooling Water Outlet | Temperature      |
| BoostPump   | Outlet               | Pressure         |
| Inverter    |                      | Electricity      |
|             |                      | Rotational Speed |

Table 5.2: List of Measurements

its maximum rate, corresponding to an electrical power output of about 116 kW<sub>e</sub>. Since the changes are relatively small, one expects the two transients to be symmetrical, in terms of maximum overshoot, settling time, presence and damping of oscillations, etc., as the system response to small perturbations is approximately linear. On the other hand, they are large enough to obtain an acceptable signal-to-noise ratio.

Note that the gas burner is not controlled in any way, so that the disturbances occurring upstream the natural gas supply (e.g., pressure changes due to other gas loads in the factory being turned on or off) affect the heat supply to the system, which in turn affects the measured output. This explains some of the variability in the output transients, which cannot be replicated by the model.

Subsequently, the heat load is reduced until the electrical output is about 69 kW<sub>e</sub> and, after the system has reached a new steady-state, other two small set point step changes are applied in reverse order. In this way, the ability of the model to predict steady-state and transient behavior in off-design conditions is also tested. Note that in this first set of experiment, reliable instantaneous measurements of the flue gas flow rate are not available; the steady-state values are computed based on static thermal energy balances, using the average values of the measurements when no changes (except the unmeasured disturbances in the gas supply) are applied.

The goal of the second set of experiment is instead to validate the ability of the model to predict the dynamic behavior when the heat supplied is changed. Another setup was used, differing from the first one only because of a different evaporator, in order to recover energy from the flue gases of two stationary diesel engines. The ORC unit is operating at a power output of approximately  $150 \text{ kW}_e$ , when one of the engines suddenly trips. This leads to a very fast change of the exhaust gas flow of approximately half of the mass flow within one sampling interval of 10 seconds. The exact timing of the step in the exhaust gas mass flow can be inferred by the small, but fast, change of the exhaust gas temperature, which is due to the fact that the two engines are not perfectly balanced. The turbine inlet temperature controller reacts by drastically lowering the turbo-pump speed, in order to avoid the temperature being reduced too much as the heat flow is nearly halved.

### 5.5.3. SIMULATIONS

For the first set of experiments (the TIT set point changes performed on the test stand machine), both the open-loop and the closed-loop model are simulated. The open loop-model aims at verifying the accuracy of the model: ideally, if the model were perfect, applying the measured control inputs to the model (i.e., the turbo-pump speed) should result in outputs matching exactly the measured outputs. Of course this will never be possible in practice, so some small drifts and discrepancies are observed. The closed-loop model aims instead at validating the capability of the dynamic plant model to support the design of feedback controllers. If the main dynamic features of the simulated system response to a set point step change (stability, rise time and settling time, damping of oscillations) are close to the measured ones, then the description of the plant dynamics in the frequency band of interest for the controller is good enough for this purpose. Finally, since in this experimental setup the condenser pressure is changing with the load level, both systems with explicit condenser models and with trivial condenser model, obtained by redeclaring the component, are compared.

For the second set of experiments, the evaporator model was replaced, in order to match the different type used in this case. Also the recuperator model parameters had to be adapted in order to reflect some smaller design changes affecting the mass of the plates and the heat transfer surface. In this case, the cooling water flow was controlled in order to keep a constant pressure in the condenser, so the model with the trivial, fixed pressure condenser was good enough to replicate the system performance. Only open loop simulations were performed in this case, as the actual set-point time history was not available in the data recording, making it impossible to replicate the closed-loop transient.

### 5.5.4. RESULTS

In figure 5.5 the comparison between the measurements and two simulations is visualized for the TIT set point change experiment at  $116 \text{ kW}_e$  output power. For confidentiality reasons, all variables are normalized so that the initial measured value is scaled to one; time is normalized with respect to the experiment duration, zero being the instant when the perturbation is applied to the system starting from steady-state operation.

The open-loop turbo-pump speed matches the experimental result by construction as the

measurement was actually used as the system input for simulation; however, also the closed-loop transient of that variable, which involves the entire plant as well as the control system models, shows a satisfactory match. The fast oscillation between time 0.25 and 0.45, which are also visible in most other variables, are probably due to some disturbances in the gas supply, as they are not visible in the subsequent set point response transient, which should have roughly the same shape because of close-to-linear operation. The closed-loop transients of both evaporator toluene inlet and turbine inlet temperatures are of course slightly better than their open-loop counterpart, since the feedback controller in the simulator compensates for some of the model error, as it tries to match the TIT set point. All variables in general show a very good match, save perhaps the condenser outlet pressure, which is obviously affected by unmeasured disturbances acting on the condenser cooling system.

Figure 5.6 shows the same variables when stepwise TIT set point changes of the same magnitude as before are applied (in reverse order) at the lower electrical output power of 69 kW<sub>e</sub>. All variables are still normalized to their full-load values, so that the relative changes of the initial steady-state values can be seen for time  $t < 0$ , as well as possible changes in the response amplitude or shape. All variables have lower values, with the exception of the initial TIT, which is the same because it is controlled to the same set point. In steady-state operation at this power level, there is an offset in the open-loop simulation of maximum 3 % with respect to the experimental value, which is indeed satisfactory, considering that the power output has been reduced by 40 %, which is a significantly off-design operating point. Note that the model parameters have mostly been tuned in order to match the full-load operating point; there is some limited ability to also tune the model with respect to off-design operation, e.g., by adapting the exponent  $n$  in equation (5.1), but that is not enough to obtain a perfect match by construction. Also note that the turbine outlet pressure has a 21 % reduction in relative terms, while the condenser outlet pressure shows a much smaller reduction about 12 %: this is due to the significant friction losses through the recuperator in between, which become substantially smaller in reduced load conditions.

In the case of the closed-loop simulations, the PI controller brings the turbine inlet temperature to its set point value and consequently determines a better simulation of the other variables which are closely related to this temperature; in this case, the offset is visible in the turbo-pump rotational speed, which is instead correct by definition in the open-loop simulations. If the steady-state offset, which is relatively small, is discounted, the shape of the transients is matched well for all the variables. This is good, as the performance of a linear controller close to a given steady state mainly depends on the dynamic response of the variables relative to their equilibrium value, rather than on their absolute values.

It is apparent how the system response to a step change in the TIT set point is different in these reduced load conditions, as all variables show less or no overshoot and smoother responses, compared to the full load transients. This phenomenon, which is apparent in the experimental data, is also replicated by the model, which is therefore shown to also be able to capture the changes in dynamic behavior of the plant with the load conditions.

With reference to the closed-loop simulations, since the only input to the model (the TIT

set point) undergoes abrupt step changes, the shape of the ensuing transients is entirely determined by the closed-loop interaction of the TIT controller with the plant dynamics, which is the result of all mass and energy storage phenomena. The good match of that shape with the experimental data allows to conclude that the model does a good job at describing the dynamic behavior of the plant which is relevant to determine its closed-loop operation.

Finally, Figure 5.7 shows the difference between the full condenser model and the trivial one at the lower output power level, for some selected variables. The trivial condenser model prescribes the condensation pressure, which is instead variable in the full condenser model. The trivial condenser model is set up using the nominal load pressure, so it works well there by construction, but when large changes in toluene mass flow occur due to the load reduction, since the cooling water flow is constant, the measured condenser pressure is reduced significantly, while the trivial condenser model still assumes the same value. The full condenser model instead predicts the condenser pressure reduction fairly accurately. As a consequence, other variables that depend on the condenser pressure, such as the turbo-pump outlet temperature, are also predicted more accurately, in particular with regards to their off-design, steady-state values, shown for time  $t < 0$ .

The result of the open-loop 50 % heat load step reduction experiment are shown in Figure 5.8. Again, the measured values of the turbo-pump speed are used as inputs for the model. Note how, despite the very wide and sharp perturbation applied to the plant (abrupt loss of half of the heat load), most variables are predicted quite accurately, with the partial exception of the evaporator toluene inlet temperature; for some reason, the recuperator dynamic response, which is the main factor in determining that variable, over-estimates the reduction in that temperature, both initially and at steady-state. As to the condenser pressure, some change is noticeable in the pressure measurement; however, due to lack of knowledge about the precise behavior of the condenser cooling flow controller, it was not possible to replicate its operation, so a fixed-pressure model was eventually used to allow predicting the other system variables with fairly good accuracy.

In this case, despite the fact that the flue gas flow is halved abruptly at time  $t = 0$ , all the outputs shown in 5.8b-h change more slowly, due to the dynamic effects of mass and energy storage in the plant. It is also apparent how the turbine mass flow transient is much slower than the turbo-pump speed transient (which is the other input to the system), while the evaporator inlet temperature shows an undershoot, which results from the combination of faster and slower dynamics with opposite effects in the system.

Ideally, in order to show what the dynamic effects of storage in the plant are, experiments should have been performed where the physical input variables of the plant, namely the pump rotational speed and the flue gas flow, were changed step-wise in open loop, one at a time: in that case, the shape of the transients would have been entirely determined by the dynamic storage phenomena, and not by the shape of the input signal or by the plant-controller interaction. Unfortunately, it was not possible to perform this kind of experiments due to safety concerns on the experimental set up.

Summing up, it is possible to draw the following conclusions. With respect to the steady state values of all the main variables:

1. at full load, all variables are reproduced with less than 1 % error, which is comparable to the amplitude of the random fluctuations that those variables have in the plant during steady operation;
2. at reduced load (-40 % to -50 % heat load) all variables are reproduced with less than 3 % error;
3. as there are no discontinuities in the plant operation at intermediate load levels, one can reasonably assume that the latter case is the worst case, and that steady-state errors will be less than 3 % in all intermediate steady operating points.

Given all the approximations involved in the modelling process and the uncertainties in the experimental conditions (e.g. the lack of reliable flue-gas flow measurements and the random fluctuations in the heat input), these results can be considered more than satisfactory.

5

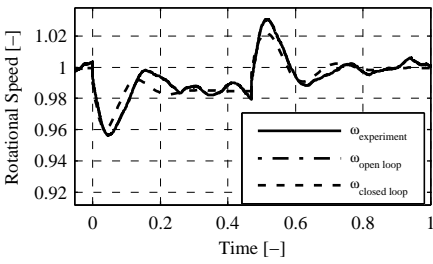
With respect to dynamic conditions, one can evaluate the relative changes of the main variables from their steady-state values following small perturbations, which are mostly relevant for the dynamic performance of linear controllers. More specifically, the main features of those transients, i.e. time and value of maximum overshoot, settling time, frequency and damping of oscillations, final value, can be considered:

1. in most cases, the main features of the transients are predicted with less than 25 % error;
2. larger errors are occasionally found for some of the variables (e.g., the negative spike of the condenser pressure measurement at time  $t = 0.52$  in figure 5.5-h), but in many cases they can very likely be attributed to spurious unmodelled disturbances.

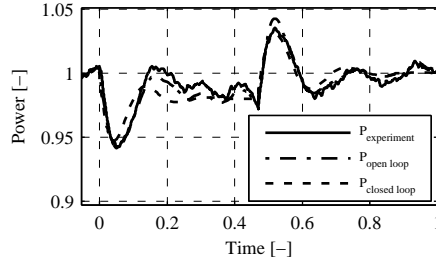
Given the poor signal-to noise ratio, due to measurement noise and spurious fluctuations of the heat load, these results can be considered more than adequate. Note that, for the sake of feedback control design, a well-designed controller will operate in a completely satisfactory way when such discrepancies are found between the model used for design and the actual plant dynamics, because of the inherent robustness of feedback control. Finally, it is worth stressing once more that the match of the main dynamic features of the closed-loop model response with the actual closed-loop experimental data points out that the model is fit to support the design and tuning of such controllers prior to the plant construction and commissioning, which can help design the equipment in order to obtain a better dynamic behaviour and save a lot of time and trouble during commissioning compared to a purely empirical approach to control design and tuning.

## 5.6. PERSPECTIVES ON CHALLENGING CONTROL PROBLEMS

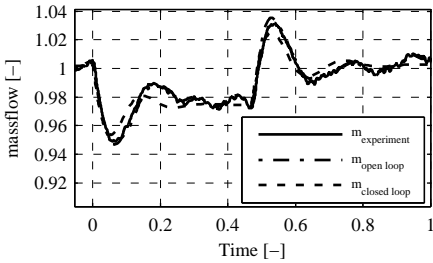
The object-oriented modeling methodology for the dynamic modeling of ORC power systems has been successfully validated on an industrial case study. The case under consideration was not particularly critical from the point of view of control, since the system is



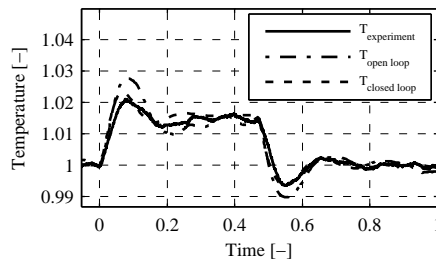
(a) Turbopump rotational speed



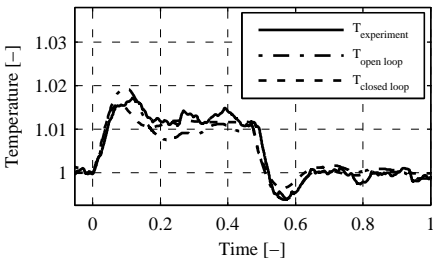
(b) Electrical Output Power



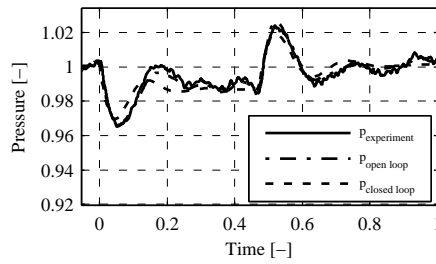
(c) Turbine Mass Flow



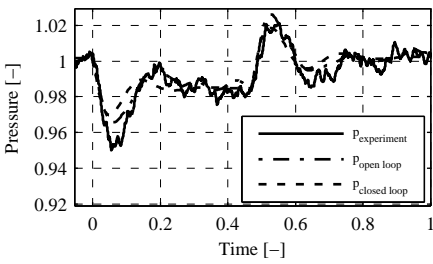
(d) Evaporator Toluene Inlet Temperature



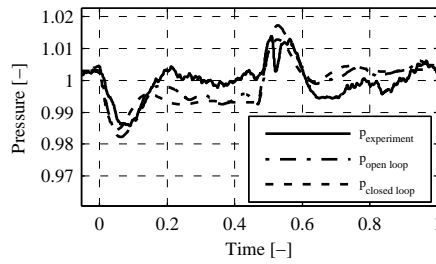
(e) Turbine Inlet Temperature



(f) Turbine Inlet Pressure



(g) Turbine Outlet Pressure



(h) Condenser Outlet Pressure

Figure 5.5: Setpoint change at 116 kW<sub>e</sub> output

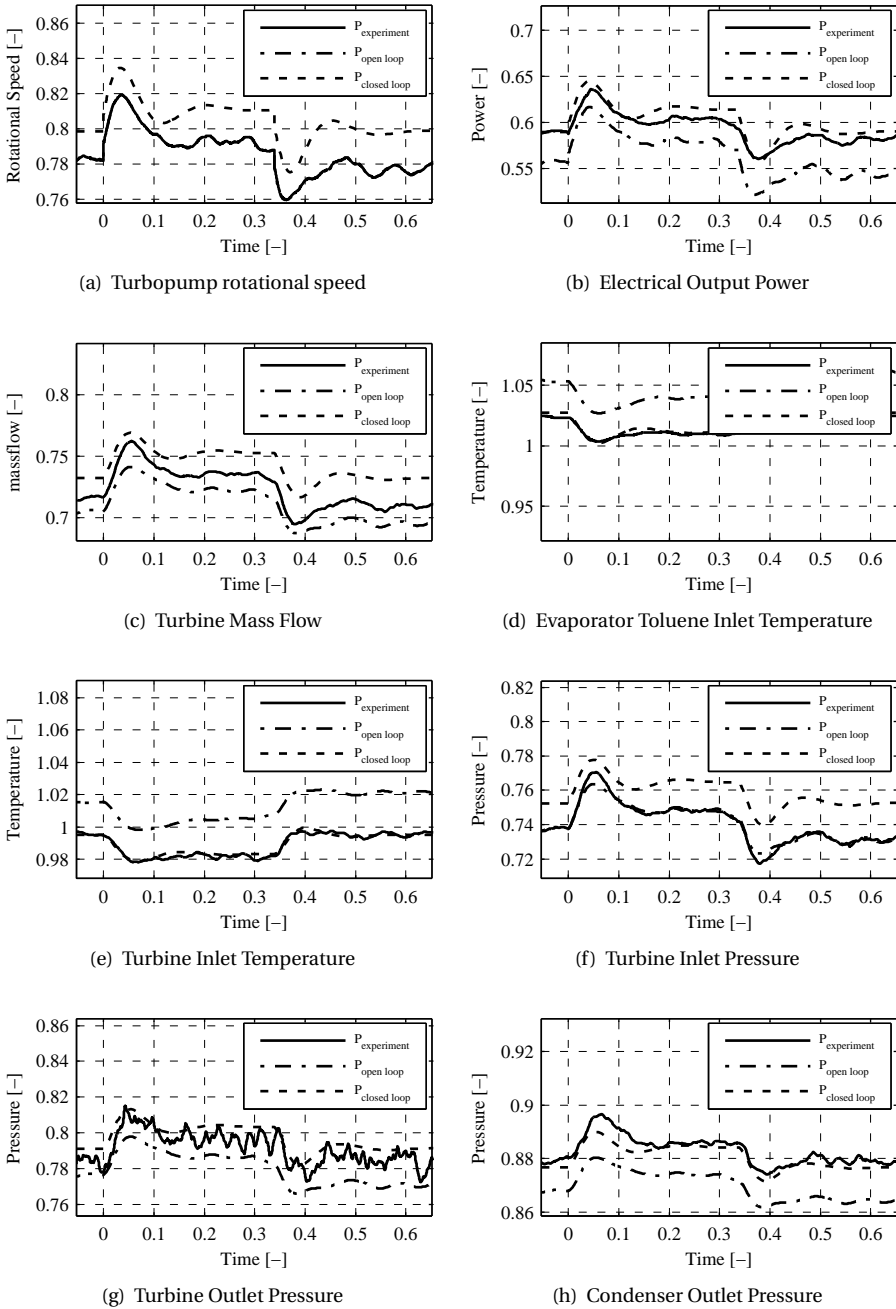


Figure 5.6: Setpoint change at 69 kW<sub>e</sub> output

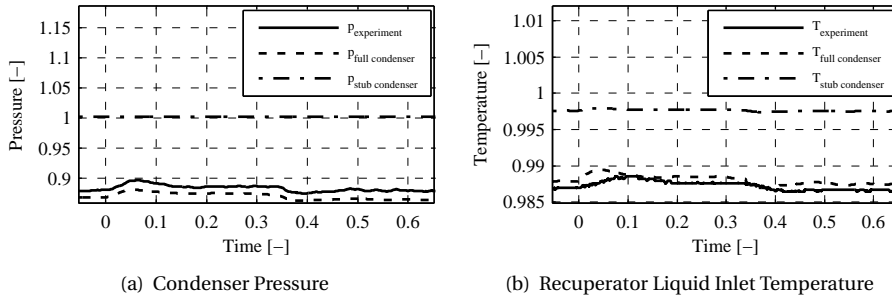


Figure 5.7: Difference between the full condenser and stub condenser model at 69 kW<sub>e</sub> output power

usually operated at constant load near to the design point, in order to maximize the return on investment. However, the developed models can now be used to tackle more challenging design problems, where dynamics and control can play a more crucial role.

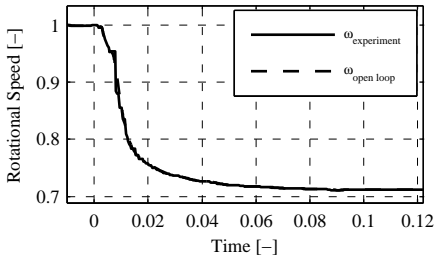
A first interesting case is the design of small units for small scale domestic heat and power generation. The heat load can be strongly time-varying in this case, and the whole range of operation, including hot and cold start-up, must be fully automated and optimized with respect to efficiency, safety, and plant lifetime. Unconventional equipment could be selected for economic reasons, which might result in dynamic behavior which is adverse to effective control, so it is of paramount importance to consider dynamic and control issues from the early stages of design, when different alternatives are evaluated in terms of equipment selection and sizing.

The use of small-size ORC systems for heat recovery from automotive engines is also a promising field of research and development, which also calls for highly dynamic operation and extensive assessment of closed-loop operation under widely changing operating conditions, where the system must run without any kind of expert operator supervision. Dynamic modeling is essential in this area as well.

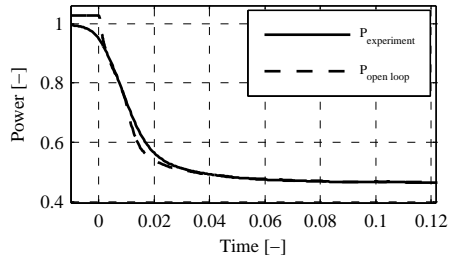
Dynamic performance and control will also be important for off-grid applications, e.g. for use in remote locations or in developing countries without an established grid infrastructure. The control problems here will be significant, since the prime mover must quickly match the time-varying user loads in order to keep power quality at acceptable levels. Object-oriented modeling will also be convenient in this case for its ease in building models of innovative integrated plants, e.g. exploiting batteries, supercapacitors, auxiliary diesel generators, etc. As in the previously mentioned applications, dynamic modeling capability will be useful for equipment selection and sizing, coupled with the assessment of achievable closed-loop performance from the early design stages up to detailed engineering and commissioning.

Last, but not least, the design and successful operation of innovative ORC solar-thermal

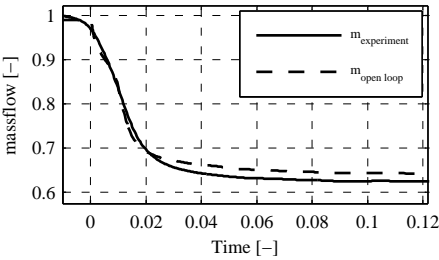




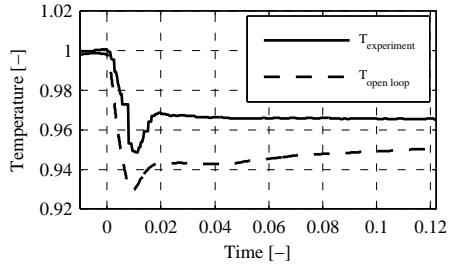
(a) Turbopump rotational speed



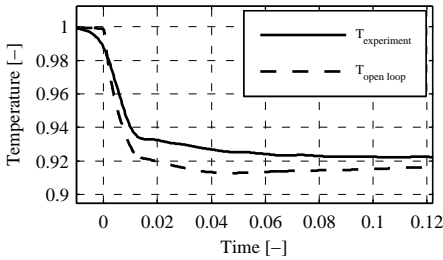
(b) Electrical Output Power



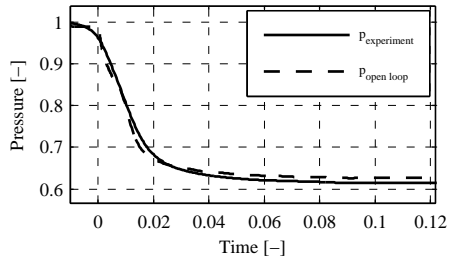
(c) Turbine Mass Flow



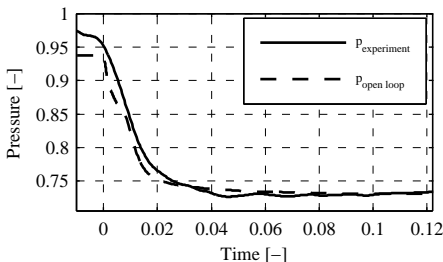
(d) Evaporator Toluene Inlet Temperature



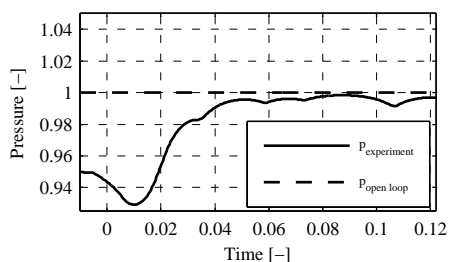
(e) Turbine Inlet Temperature



(f) Turbine Inlet Pressure



(g) Turbine Outlet Pressure



(h) Condenser Outlet Pressure

Figure 5.8: Disturbance rejection of the operational plant

plants requires a thorough understanding and mastery of dynamic operation, both for short-term automatic control to reject the wide and fast changes of solar radiation in cloudy weather conditions, and for longer-term optimal use of energy storage systems coupled with the energy conversion unit. The flexibility and extensibility of the proposed approach will allow to tackle the analysis of control problems also in the case of complex and/or highly integrated innovative plant designs.

As a final remark, the use of the modeling methods described here is not limited to dynamic simulation, used both for open-loop analysis of the process dynamics and for closed-loop assessment of the control system performance under realistic operation scenarios. A very promising emerging field is the direct application of such models in optimal control and model-predictive control of energy conversion systems, and in particular of ORC systems. In this case, the model can be directly used to determine optimal transients off-line, or even to compute the control actions on line, in order to maximize some performance criterion while fulfilling some operational constraints. For an overview of the enabling technologies, see [100].

## 5.7. CONCLUDING REMARKS

In this chapter, an object-oriented approach to dynamic modeling of ORC systems has been presented. The modeling methodology has been validated with an industrial case study, namely the measurements of transient operation performed with a 150 kW<sub>e</sub> Tri-O-Gen turbogenerator for waste heat recovery, using toluene as working fluid. The simulation results confirm the ability of the proposed methodology to predict steady-state and dynamic plant behavior in nominal and off-design operating conditions, and in particular to effectively capture the control-relevant dynamic response. The model library which is the outcome of this work can thus be used as a basis to support the design of innovative ORC systems with highly dynamic operation and challenging control problems, such as in waste-heat recovery on trucks or in concentrated solar energy, as well as to support the improvement and more efficient operation of existing ORC plants.



# 6

## CONCLUSION & OUTLOOK

A novel Ludwig tube-type facility has been commissioned at Delft University of Technology to perform measurements on finite amplitude waves propagating in the NICFD regime. The pressure and temperature of the working fluid can be regulated independently from each other, such that any thermodynamic state can be achieved within the limits of the measurement system of 21 bar and 400 °C. A procedure to estimate the process start-up time of the FOV has been devised, and estimated values range from 2.1 to 9.0 ms. A method to estimate the speed of sound from wave propagation measurements is presented and found to agree within 2.1 % of the predicted value for a variety of incondensable gases. Preliminary experiments on rarefaction waves in the non-ideal regime of siloxane D<sub>6</sub> at temperatures up to 300 °C have been successfully performed, by generating a propagating rarefaction in the facility, which is measured by four pressure transducers. These preliminary experiments provide values of the wave speed that are within 8 % and speed of sound within 1.6 % of the predictions of a state-of-the-art thermodynamic model. However, estimates of the speed of sound calculated with this thermodynamic model are affected by a large uncertainty in the region of interest.

A total of five rarefaction experiments using D<sub>6</sub> as working fluid are performed with initial conditions at various pressure and temperature levels within, or close to the predicted BZT zone. The size of BZT region, and thermodynamic conditions at which it is predicted, depends on the thermodynamic model. Due to the large uncertainty in these models, it may also be possible that the BZT zone does not exist for this fluid. In fact, its existence has never been unequivocally shown experimentally for any fluid. The same procedure as for the preliminary experiments is followed in these five experiments. The wave speed is determined throughout the expansion and the speed of sound is estimated for the initial conditions in the tube using the same procedure as for the preliminary experiments. The speed of sound is found to be approximately 3 m/s to 9 m/s higher than predicted by the thermodynamic model. The speed of sound is found to be lower for the experiments with a high initial temperature than for the experiments with a low initial temperature. This trend is consistent with the predictions from the thermodynamic model, and is indicative of flows in the NICFD

regime.

An increase of wave speed in an expansion is not found in the experiments, such that no proof of a nonclassical isentropic expansion is found. However, there is a possibility of RSWs being present in the flow. These show up as a horizontal line in a wave speed versus pressure drop diagram. In two of the measurements such features are found, although no jump in wave speed is found. Whereas these could stem from the opening of the FOV, it could also indicate the presence of a double sonic RSW in the flow. This is supported by the recordings of the pressure, for which the pressure slope shows a sudden increase at the onset of the RSW. It is compatible with the possible occurrence of a shock formation process. The value of  $\Gamma$  is estimated from the wave speed, and corresponds to the model prediction of a value close to 0, showing that BZT effects could be expected. This value however, is a second derivative from the primary measured value, and is affected by high uncertainties.

In order to conclusively confirm nonclassical gasdynamic phenomena, a more thorough investigation is required for thermodynamic states encompassing the BZT zone. In the presented experiments, the indicated amount of superheating was very low in the experiments, down to  $0.5^\circ$ . The recorded saturation temperature may be affected by measurement error due to radiative heat transfer from the vapour generator wall. The process start-up time appears to be critical, since only the onset of shock formation, but no fully developed RSW has been recorded. It can be considered to remove the nozzle insert. Doing so will decrease the FOV process start-up time with the nozzle start-up duration, at the cost of disturbances being able to travel upstream.

Furthermore, computational fluid dynamic shock tube simulations in the two-phase liquid-vapour critical point region are conducted. A thermodynamic model based on scaling laws was implemented into in-house software library for the estimation of fluid thermodynamic properties. The model is valid only in the vicinity of the critical point region. The admissibility domain for RSWs is determined using  $\text{CO}_2$  and methane as working fluid. Also the maximum allowed valve opening time is estimated as a function of the initial thermodynamic state and the shock tube length. Finally the feasibility of an experiment that generates a two-phase RSW is devised starting from single-phase initial conditions at the same isotherm, greatly simplifying the technical solution to perform such an experiment.

Lastly, an object-oriented generic physically based lumped-parameter system model of an ORC, one of the applications of NICFD, is developed. A case study of transient operation of a  $150 \text{ kW}_e$  power plant is simulated and compared to dedicated experiments at both on- and off-design conditions. The heat transfer coefficients of the model are adapted to fit results in on-design conditions. The model reproduces the steady-state experimental values to within 1 %. For operation at a 40 % reduced load, this is within 3 %, which confirm the ability of the proposed methodology to predict the steady-state and dynamic plant response in nominal and off-design operating conditions, and in particular to effectively capture the control-relevant dynamic response. This is the basis to support the design of innovative ORC systems with highly dynamic operation and challenging control problems, as well as to support the improvement and more efficient operation of existing ORC plants.

# BIBLIOGRAPHY

- [1] J. Van der Waals, *De continuïteit van den Gas- en Vloeistofoestand*, Ph.D. thesis, Hoogeschool Leiden (1873).
- [2] J. van der Waals, *Onderzoekingen omtrent de overeenstemmende eigenschappen der toestands-vergelijkingen der verschillende stoffen*, Koninklijke Akademie van Wetenschappen (1880).
- [3] L. D. Landau and E. M. Lifshitz, *Fluid mechanics*, (Addison-Wesley, Reading, Mass., 1959) p. 373.
- [4] W. D. Hayes, *Fundamentals of gasdynamics*, (Princeton University Press, 1958) Chap. The basic theory of gas dynamic discontinuities, p. 426.
- [5] P. A. Thompson, *A fundamental derivative in gasdynamics*, Phys. Fluids **14**, 1843 (1971).
- [6] P. A. Thompson, *Compressible Fluid Dynamics* (McGraw-Hill, 1988).
- [7] H. A. Bethe, *The theory of shock waves for an arbitrary equation of state*, Technical report 545 (Office Sci. Res. & Dev., 1942).
- [8] Y. Zel'dovich, *On the possibility of rarefaction shock waves*, Zh. Eksp. Teor. Fiz. **4**, 363 (1946).
- [9] C. Zamfirescu, A. Guardone, and P. Colonna, *Admissibility region for rarefaction shock waves in dense gases*, J. Fluid Mech. **599**, 363 (2008).
- [10] A. Borisov, A. Borisov, S. Kutateladze, and V. Nakoryakov, *Rarefaction shock waves near the critic liquid-vapour point*, J. Fluid Mech. **126**, 59 (1983).
- [11] S. S. Kutateladze, V. E. Nakoryakov, and A. A. Borisov, *Rarefaction waves in liquid and gas-liquid media*, Ann. Rev. Fluid Mech. **19**, 577 (1987).
- [12] S. Fergason, T. Ho, B. Argrow, and G. Emanuel, *Theory for producing a single-phase rarefaction shock wave in a shock tube*, J. Fluid Mech. **445**, 37 (2001).
- [13] M. S. Cramer and R. Sen, *Shock formation in fluids having embedded regions of negative nonlinearity*, Phys. Fluids **29**, 2181 (1986).
- [14] P. A. Thompson, *Liquid-vapor adiabatic phase changes and related phenomena*, in *Nonlinear Waves in Real Fluids*, edited by A. Kluwick (Springer-Verlag, New York, NY, 1991) pp. 147–213.

- [15] N. Nannan, A. Guardone, and P. Colonna, *On the fundamental derivative of gas dynamics in the vapor-liquid critical region of single-component typical fluids*, Fluid Phase Equilib. **337**, 259 (2013).
- [16] N. R. Nannan, A. Guardone, and P. Colonna, *Critical point anomalies include expansion shock waves*, Phys. Fluids **26** (2014).
- [17] S. H. Fergason, A. Guardone, and B. M. Argrow, *Construction and validation of a dense gas shock tube*, J. Thermophys. Heat Tr. **17**, 326 (2003).
- [18] L. Calderazzi and C. Colonna di Paliano, *Thermal stability of R-134a, R-141b, R-131I, R-7146, R-125 associated with stainless steel as a containing material*, Int. J. Refrig. **20**, 381 (1997).
- [19] P. R. Dvornic, *High temperature stability of polysiloxanes*, Silicon Compounds: Silanes and Silicones, Gelest Catalog, 419 (2004).
- [20] P. A. Thompson and W. F. Loutrel, *Opening time of brittle shock-tube diaphragms for dense fluids*, Rev. Sci. Instrum. **44**, 1436 (1973).
- [21] A. Guardone, *Three-dimensional shock tube flows of dense gases*, J. Fluid Mech. **583**, 423 (2007).
- [22] P. Colonna and A. Guardone, *Molecular interpretation of nonclassical gas dynamics of dense vapors under the Van der Waals model*, Phys. Fluids **18**, 056101 (2006).
- [23] W. J. M. Rankine, *On the thermodynamic theory of waves of finite longitudinal disturbance*, Phyl. Trans. **160**, 277 (1870).
- [24] P.-H. Hugoniot, *Sur la propagation du mouvement dans les corps et spécialement dans les gaz parfaits*, J. Ecole Polytechnique **57**, 3 (1887).
- [25] P. D. Lax, *Hyperbolic systems of conservation laws II*, Comm. Pure Appl. Math. **10**, 537 (1957).
- [26] O. Oleinik, *Uniqueness and stability of the generalized solution of the Cauchy problem-fora quasi-linear problem*, Usp. Math. Nauk. **14**, 165 (1959).
- [27] A. Kluwick, *Handbook of shock waves*, (Academic Press, 2001) Chap. 3.4. Rarefaction shocks, pp. 339–411.
- [28] A. Guardone, C. Zamfirescu, and P. Colonna, *Maximum intensity of rarefaction shock waves for dense gases*, J. Fluid Mech. **642**, 127 (2010).
- [29] M. Maerefat, S. Fujikawa, T. Akamatsu, T. Goto, and T. Mizutani, *An experimental study of non-equilibrium vapour condensation in a shock-tube*, Exp. Fluids **7**, 513 (1989).
- [30] F. Peters and T. Rodemann, *Design and performance of a rapid piston expansion tube for the investigation of droplet condensation*, Exp. Fluids **24**, 300 (1998).

- 
- [31] J. L. Wagner, S. J. Beresh, S. P. Kearney, W. M. Trott, J. N. Castaneda, B. O. Pruett, and M. R. Baer, *A multiphase shock tube for shock wave interactions with dense particle fields*, *Exp. Fluids* **52**, 1507 (2012).
- [32] D. R. White, *Influence of diaphragm opening time on shock-tube flows*, *J. Fluid Mech.* **4**, 585 (1958).
- [33] P. Gaetani, A. Guardone, and G. Persico, *Shock tube flows past partially opened diaphragms*, *J. Fluid Mech.* **602**, 267 (2008).
- [34] M. S. Cramer, *Shock splitting in single-phase gases*, *J. Fluid Mech.* **199**, 281 (1989).
- [35] B. Brown and B. Argrow, *Application of Bethe-Zel'dovich-Thompson fluids in organic Rankine cycle engines*, *J. Propul. Power* **16**, 1118 (2000).
- [36] P. Colonna, E. Casati, C. Trapp, T. Mathijssen, J. Larjola, T. Turunen-Saaresti, and A. Uusitalo, *Organic Rankine cycle power systems: the path from the concept to current technology, application and an outlook to the future*, *J. Eng. Gas Turb. Power* **137**, 100801 (2015).
- [37] M. S. Cramer and R. N. Fry, *Nozzle flows of dense gases*, *Phys. Fluids. A* **5** (1993).
- [38] A. P. S. Wheeler and J. Ong, *The role of dense gas dynamics on organic Rankine cycle turbine performance*, *J. Eng. Gas Turb. Power* **135**, 102603 (2013).
- [39] J. Harinck, T. Turunen-Saaresti, P. Colonna, S. Rebay, and J. van Buijtenen, *Computational study of a high-expansion ratio radial ORC turbine stator*, *J. Eng. Gas Turb. Power* **132** (2010).
- [40] M. Lampe, C. Kirmse, E. Sauer, M. Stavrou, J. Gross, and A. Bardow, *Computer aided molecular design of ORC working fluids using PC-SAFT*, *Comput. Aided Chem. Eng.* **34**, 357 (2014).
- [41] C. Zamfirescu and I. Dincer, *Performance investigation of high-temperature heat pumps with various BZT working fluids*, *Thermochim. Acta* **488**, 66 (2009).
- [42] T. Conboy, S. Wright, J. Pasch, D. Fleming, G. Rochau, and R. Fuller, *Performance characteristics of an operating supercritical CO<sub>2</sub> Brayton cycle*, *J. Eng. Gas Turb. Power* **134** (2012).
- [43] E. Rinaldi, R. Pecnik, and P. Colonna, *Computational fluid dynamic simulation of a supercritical CO<sub>2</sub> compressor performance map*, *J. Eng. Gas Turb. Power* **137**, 072602 (2015).
- [44] N. Nannan, P. Colonna, C. Tracy, R. Rowley, and J. Hurly, *Ideal-gas heat capacities of dimethylsiloxanes from speed-of-sound measurements and ab initio calculations*, *Fluid Phase Equilib.* **257**, 102 (2007).
- [45] T. Weith, F. Heberle, M. Preißinger, and D. Brüggeman, *Performance of siloxanes mixtures in a high-temperature organic rankine cycle considering the heat transfer characteristics during evaporation*, *Energies* **7**, 5548 (2014).



- [46] A. Spinelli, F. Cozzi, M. Zocca, P. Gaetani, V. Dossena, and A. Guardone, *Experimental investigation of a non-ideal expansion flow of siloxane vapor MDM*, in *ASME Turbo Expo 2016: Turbomachinery Technical Conference*, GT2016-57357 (2016).
- [47] A. Uusitalo, T. Turunen-Saaresti, J. Honkatukia, P. Colonna, and J. Larjola, *Siloxanes as working fluids for mini-orc systems based on high-speed turbogenerator technology*, *J. Eng. Gas Turb. Power* (2013).
- [48] A. J. Head, C. D. Servi, E. Casati, M. Pini, and P. Colonna., *Preliminary design of the ORCHID: A facility for studying non-ideal compressible fluid dynamics and testing ORC expanders*. in *ASME Turbo Expo 2016*, GT2016-56103 (2016).
- [49] P. Colonna, N. R. Nannan, and A. Guardone, *Multiparameter equations of state for siloxanes:  $[(CH_3)_3-Si-O_{1/2}]_2-[O-Si-(CH_3)_2]_{i=1,\dots,3}$  and  $[O-Si-(CH_3)_2]_6$* , *Fluid Phase Equilib.* **263**, 115 (2008).
- [50] N. Nannan and P. Colonna, *Improvement on multiparameter equations of state for dimethylsiloxanes by adopting more accurate ideal-gas isobaric heat capacities: Supplementary to P. Colonna, N. R. Nannan, A. Guardone, E. W. Lemmon*, *Fluid Phase Equilib.* **244**, 193 (2006), *Fluid Phase Equilib.* **280**, 151 (2009).
- [51] N. H. Forster and H. K. Trivedi, *Rolling contact testing of vapor phase lubricants - part i: Material evaluation*, *Tribol. Trans.* **40**, 421 (1997).
- [52] F. Schrijer and W. Bannink, *Description and flow assessment of the delft hypersonic ludwig tube*, *J. Spacecraft Rockets* **47**, 125 (2010).
- [53] H. Knauss, R. Riedel, and S. Wagner, *The shock wind tunnel of stuttgart university - a facility for testing hypersonic vehicles*, in *9th International Space Planes and Hypersonic Systems and Technologies Conference*, AIAA 99-4959 (1999).
- [54] P. Colonna, T. P. van der Stelt, and A. Guardone, *FluidProp (Version 3.0): A program for the estimation of thermophysical properties of fluids*, <http://www.fluidprop.com/> (2012), a program since 2004.
- [55] P. Colonna, *Fluidi di lavoro multi componenti per cicli termodinamici di potenza (Multicomponent working fluids for power cycles)*, Ph.D. thesis, Politecnico di Milano (1996).
- [56] R. C. McMaster, *Nondestructive testing handbook*, 3rd ed., Vol. Volume 1-Leak testing (American Society for Nondestructive Testing, 1997).
- [57] R. Stalker and N. Mudford, *Unsteady shock propagation in a steady flow nozzle expansion*, *J. Fluid Mech.* **241**, 525 (1992).
- [58] D. Cagliostro and J. Johnson, III, *Starting phenomena in a supersonic tube wind tunnel*, *AIAA J.* **9**, 101 (1971).
- [59] E. Lemmon, M. Huber, and M. McLinden, *NIST standard reference database 23: Reference fluid thermodynamic and transport properties-REFPROP, version 9.1*, (2013.).

- 
- [60] R. Menikoff and B. J. Plohr, *The Riemann problem for fluid flow of real material*, Rev. Mod. Phys. **61**, 75 (1989).
- [61] P. A. Thompson, G. Carofano, and Y. Kim, *Shock waves and phase changes in a large-heat-capacity fluid emerging from a tube*, J. Fluid Mech. **166**, 57 (1986).
- [62] T. Kurschat, H. Chaves, and G. Meier, *Complete adiabatic evaporation of highly superheated liquid jets*, J. Fluid Mech. **236**, 510 (1992).
- [63] P. A. Thompson, H. Chaves, G. E. A. Meier, Y. Kim, and H.-D. Speckmann, *Wave splitting in a fluid of large heat capacity*, J. Fluid Mech. **185**, 385 (1987).
- [64] S. Schlamp and T. Rösgen, *Flow in near-critical fluids induced by shock and expansion waves*, Shock Waves **14**, 93 (2005).
- [65] N. Nannan, C. Sirianni, T. Mathijssen, A. Guardone, and P. Colonna, *The admissibility domain of rarefaction shock waves in the near-critical vapour-liquid equilibrium region of pure typical fluids*, J. Fluid Mech. , 241 (2016).
- [66] S. Ferguson and B. Argrow, *Simulations of Nonclassical Dense Gas Dynamics*, in *35th AIAA Thermophysics Conference, Anaheim, CA, U.S.A*, 2752 (2001).
- [67] J. M. H. Levelt-Sengers, *Scaling predictions for thermodynamic anomalies near the gas-liquid critical point*, Ind. Eng. Chem. Fundam. **9**, 470 (1970).
- [68] A. Michels, J. V. Sengers, and P. S. van der Gulik, *The thermal conductivity of carbon dioxide in the critical region II. Measurements and conclusions*, Physica **28**, 1216 (1962).
- [69] P. C. Albright, T. J. Edwards, Z. Y. Chen, and J. V. Sengers, *A scaled fundamental equation for the thermodynamic properties of carbon dioxide in the critical region*, J. Chem. Phys. **87**, 1717 (1987).
- [70] D. S. Kurumov, G. A. Olchowy, and J. V. Sengers, *Thermodynamic properties of methane in the critical region*, Int. J. Thermophys. **9**, 73 (1988).
- [71] J. M. H. Levelt-Sengers, G. Morrison, and R. F. Chang, *Critical behavior in fluids and fluid mixtures*, Fluid Phase Equilib. **14**, 19 (1983).
- [72] E. W. Lemmon, M. O. McLinden, and M. L. Huber, *NIST Standard Reference Database 23: Reference Fluid Thermodynamic and Transport Properties-REFPROP, Version 8.0*, National Institute of Standards and Technology (2002).
- [73] P. Colonna, N. Nannan, A. Guardone, and T. van der Stelt, *On the computation of the fundamental derivative of gas dynamics using equations of state*, Fluid Phase Equilib. **286**, 43 (2009).
- [74] J. M. H. Levelt-Sengers, *From Van der Waals' equation to scaling laws*, Physica **73**, 73 (1973).
- [75] F. W. Balfour, J. V. Sengers, M. R. Moldover, and J. M. H. Levelt-Sengers, *Universality, revisions and corrections to scaling in fluids*, Phys. Lett. A **65**, 223 (1978).

- [76] P. Schofield, *Parametric representation of the equation of state near a critical point*, Phys. Rev. Lett. **22**, 606 (1969).
- [77] W. H. Press, S. A. Teukolsky, W. T. Vetterling, and B. P. Flannery, *Numerical Recipes 3rd Edition: The Art of Scientific Computing*, 3rd ed. (Cambridge University Press, New York, NY, USA, 2007).
- [78] A. Guardone and L. Vigevano, *Roe linearization for the van der Waals gas*, J. Comput. Phys. **175**, 50 (2002).
- [79] P. Cinnella, *Roe-type schemes for dense gas flow computations*, Comput. Fluids (2006).
- [80] M. Arora and P. L. Roe, *On postshock oscillations due to shock capturing schemes in unsteady flows*, J. Comput. Phys. **130**, 25 (1997).
- [81] E. F. Toro, *Riemann solvers and numerical methods for fluid dynamics: a practical introduction* (Springer Science & Business Media, 2009).
- [82] T. Mathijssen, M. Gallo, E. Casati, N. Nannan, C. Zamfirescu, A. Guardone, and P. Colonna, *The flexible asymmetric shock tube (FAST), a Ludwig tube facility for wave propagation measurements in high-temperature vapours of organic fluids*, J. Fluid Mech. (2015).
- [83] D. Wei, X. Lu, Z. Lu, and J. Gu, *Dynamic modeling and simulation of an organic Rankine cycle (ORC) system for waste heat recovery*, Appl. Therm. Eng. **28**, 1216 (2008).
- [84] S. Quoilin, R. Aumann, A. Grill, A. Schuster, V. Lemort, and H. Spliethoff, *Dynamic modeling and optimal control strategy of waste heat recovery organic Rankine cycles*, Appl. Energy **88**, 2183 (2011).
- [85] P. Colonna and H. van Putten, *Dynamic modeling of steam power cycles.: Part I – modeling paradigm and validation*, Appl. Therm. Eng. **27**, 467 (2007).
- [86] H. van Putten and P. Colonna, *Dynamic modeling of steam power cycles: Part II – simulation of a small simple Rankine cycle system*, Appl. Therm. Eng. **27**, 2566 (2007).
- [87] S. E. Mattsson, H. Elmqvist, and M. Otter, *Physical system modeling with Modelica*, Control Eng. Pract. **6**, 501 (1998).
- [88] M. Tiller, *Introduction to physical modelling with Modelica* (Kluwer, 2001).
- [89] P. Fritzson, *Principles of Object-Oriented Modeling and Simulation with Modelica 2.1* (Wiley, 2003).
- [90] F. Casella, *Object-oriented modelling of power plants: a structured approach*, in *Proceedings of the IFAC Symposium on Power Plants and Power Systems Control* (IFAC, Tampere, Finland, 2009).
- [91] F. Casella and P. Colonna, *Dynamic modelling of IGCC power plants*, Appl. Therm. Eng. **35**, 91 (2012).

- 
- [92] F. Cellier and E. Kofman, *Continuous System Simulation* (Springer-Verlag, 2006).
- [93] A. Cammi, F. Casella, M. Ricotti, and F. Schiavo, *Object-oriented modeling, simulation and control of the iris nuclear power plant with modelica*, in *Proceedings 4th International Modelica Conference*, edited by G. Schmitz (Modelica Association, Hamburg, Germany, 2005) pp. 423–432.
- [94] F. Casella and A. Leva, *Modelica open library for power plant simulation: Design and experimental validation*, in *Proceedings 3rd International Modelica Conference*, edited by P. Fritzson (Modelica Association, Linköping, Sweden, 2003) pp. 41–50.
- [95] F. Casella and A. Leva, *Modelling of thermo-hydraulic power generation processes using Modelica*, *Math. Comput. Modell. Dyn. Syst.* **12**, 19 (2006).
- [96] F. Casella and C. C. Richter, *ExternalMedia: a library for easy re-use of external fluid property code in Modelica*, in *Proceedings 6th International Modelica Conference*, edited by B. Bachmann (Modelica Association, Bielefeld, Germany, 2008) pp. 157–161.
- [97] J. Larjola, *Electricity from industrial waste heat using high-speed organic Rankine cycle (ORC)*, *Int. J. Prod. Econ.* **41**, 227 (1995), proceedings of the 12th International Conference on Production Research.
- [98] R. Franke, F. Casella, M. Otter, M. Sielemann, H. Elmqvist, S. Mattsson, and H. Olsson, *Stream connectors - an extension of Modelica for device-oriented modeling of convective transport phenomena*, in *Proceedings 7th International Modelica Conference*, edited by F. Casella (The Modelica Association, Como, Italy, 2009) pp. 108–121.
- [99] E. Lemmon and R. Span, *Short fundamental equations of state for 20 industrial fluids*, *J. Chem. Eng. Data* **51**, 785 (2006).
- [100] J. Åkesson, C. Årzén, M. Gäfvert, T. Bergdahl, and H. Tummescheit, *Modeling and optimization with Optimica and JModelica.org – Languages and tools for solving large-scale dynamic optimization problems*, *Comput. Chem. Eng.* **34**, 1737 (2010).



# ACKNOWLEDGEMENTS

Finishing a PhD is not something that is done alone. Although this dissertation bears my name on the cover, I would not have been able to complete it without the help of many people. Some contributed in an intellectual way, others textually, emotionally or socially. I am indebted to all of you, who have supported me in any of these ways. Although the list may not be conclusive, I would like to write down some names.

I would first like to thank my promotors. I am very grateful to prof. Piero Colonna, who has supervised me throughout the PhD, supported me in difficult times, and also celebrated with me in times of success. I feel lucky to have had you as a supervisor. I greatly admire your never-ending optimism, even at times that the situation seems hopeless. Your ability to motivate and persuade people showed me the extent of achievements this can bring. Moreover, your unsurpassed writing quality, which occasionally brought me to desperation, has been fundamental to my development as an academic. I am thankful for your guidance and the environment you created that allowed me to grow as a person. On top, I always enjoyed your kindness, both inside the office, as well as during one of the warm welcomes at your home. I fully share your vision on a green future, and I sincerely hope you will continue to be successful in contributing to this, as you have been so far. I would also like to thank my other promotor, prof. Alberto Guardone sincerely for his support during the PhD and his hospitality during my two-month visit to Milano. I highly value the scientific discussions I had with you. At times, you were the only person able to grasp my chaotic thoughts on highly complex topics, and to help me structure them in such a way, that they could be explained to other people. The quality of the work would not have been the same without you. Next to that, the kind and friendly nature of your personality makes it very enjoyable to cooperate with you.

A special gratitude goes to Mauro, with whom I worked endlessly on the FAST. I have probably not made it easy for you. Nevertheless, we were a good team. You were my daily sparring-partner, but also my working-partner with whom I shared the dirty and unpleasant parts of the research, such as chemically cleaning a vapour generator from decomposed fluid, or working in shifts to perform measurements for several consecutive days and nights. I am glad that together with you, we were able to achieve several successful experiments in the BZT region, which some people deemed impossible.

Furthermore, I would like to thank my co-workers, peers, supervisors with whom I worked closely together. My thanks go to Ryan Nannan for several aspects. You prepared an excellent starting point for my research. Furthermore, I admire the intelligence you display in your research and your vision at the Anton de Kom University in Suriname. Your hospitality, and also your family's, made both my visits to Suriname memorable and pleasant. I am very grateful for the opportunity you created for me to teach an entire course to undergraduate

students. Moreover, during your visits to the Netherlands, your presence made spending time in the office very enjoyable and fun. Furthermore, I would like to thank Francesco Casella, who supported me on challenging control aspects. You have no idea about the numerous times I had to study after a Skype call to understand in-depth the topics you had been talking about. Emiliano, also your cooperation on the FAST was very valuable. You were also there at 3 am when the first shots in  $D_6$  were done, and I appreciate your help. Gerard, thank you for the countless times you have disassembled and reassembled the valve, and the valuable insight into its technical details. Martijn, thanks for doing all the electrical work. Teus, you were always able to solve any issues on Fluidprop, and helped me a lot with the implementation of the scaling-laws. Also thanks go to Akshay and Adriano, who I supervised. I am glad that you were able to provide me valuable results. I would like to thank STW for the funding, which created the opportunity for this research in the first place. Also the user's committee provided helpful feedback every year. A special mention goes to Fulvio, who already supervised me during my Master thesis, and who first introduced me to academic research. I would also like to thank my coördinators at KNMI, Jan Rozema, Sandra van Dijke and Hans Beekhuis, who have been understanding and supportive for the numerous days I took off to work on my dissertation.

On a personal level, I am grateful to Marjolein, without whom I would not have started the PhD. Things may not have turned out the way we intended, but I am grateful for the support you gave in the first year. My department mates during my Process & Energy time, Sara, Marloes, Stevia, Stephanie, Sergio, Enrico, Carlo, Martina, thanks for the shared lunches, parties, events, bike trips, etc. The same goes to my colleagues during the Propulsion & Power time, Antonio, Salvo, Lucia, Matteo. A special mention to Adam and Sebastian for always being available to drink away the frustrations with many beers and laugh them away with jokes. The same holds for Carsten, who on top of all the drinks, introduced me to the most important person in my life. I would also like to show my gratitude to Barend, Erica and Thomas, not only for being there during the most important moments of my life, but also for helping me during times that things were not going very well. Obviously, I would not forget to thank the BBB's, Ae-Ri, Elske, Arjen, and Ivo, Nico and Daniel. And of course my parents and brothers, Johan, Mia, Romke and Onno, who provided the foundation, for me to be who I am today, and who have always been available when I needed them.

Finally, saving the best for last, I am greatly indebted to my wife Alondra. I have tested your patience to its limits during the numerous sunny days I was working on my dissertation, and I appreciate your understanding. Also I admire your knowledge of human psychology and you have opened my eyes to many aspects of my own personality, and of those of other people. Your love, that seems unlimited, has helped me through difficult times. I enjoy every moment we spend together, and I am looking forward to all the nice moments that are yet to come.

# CURRICULUM VITAE

Tiemo Mathijssen was born in Bandung, Indonesia on the 30<sup>th</sup> of October 1982. After moving to the Netherlands at the age of 3, he followed primary school in Groningen and secondary school mostly in Bergen op Zoom. In 2001, he started his studies in aerospace engineering at Delft University of Technology. He joined the international student association EUROAVIA, where he became Editor in Chief of EUROAVIA News for 1.5 year and President of EUROAVIA Delft for one year. Part of his MSc degree was spent in Maranello, Italy, doing an internship at Ferrari, where he improved the aerodynamics of the F430 GT2 car using computational fluid dynamics. In 2008 he obtained his MSc degree in the field of aerodynamics with his thesis "Stereoscopic PIV on delta wings in a supersonic flow". He moved to Bremen, Germany, to work for EADS Astrium Space Transportation, developing a new upper stage for the Ariane 5 launcher. He worked, among other things, on the preliminary design, doing thermodynamic calculations on the cryogenic fuels in the tank and the attitude control system. In 2011, he started his doctoral research in the field of non-ideal compressible fluid dynamics. Parts of his doctoral degree were spent at Politecnico di Milano in Italy as a guest researcher, and at the Anton de Kom University in Paramaribo, Suriname, where he taught a university course on "Dynamic Modeling of Processes and Energy systems" to undergraduate students. In 2015, he started in a position as a sensor specialist, focused on meteorological instrumentation at the Royal Netherlands Institute of Meteorology (KNMI). Among other sensors, he now specialises in weather radars.



## **Publications**

### **Journal articles:**

N. Nannan, C. Sirianni, T. Mathijssen, P. Colonna, A. Guardone, "The admissibility domain of fluids in the vapour-liquid critical point region", *J. Fluid Mech.* 56:10, March 2016.

T. Mathijssen, M. Gallo, E. Casati, N.R. Nannan, C. Zamfirescu, A. Guardone, P. Colonna, "The Flexible Asymmetric Shock Tube (FAST): A Ludwig tube facility for wave propagation measurements in high-temperature vapours of organic fluids", *Exp. in Fluids* 56:10, October 2015.

P. Colonna, E. Casati, C. Trapp, T. Mathijssen, J. Larjola, T. Turunen-Saaresti, A. Uusitalo, "Organic Rankine cycle power systems: the path from the concept to current technology, application and an outlook to the future", *J. Eng. Gas Turbines Power*, 137 (100801), 2015.



F. Casella, T. Mathijssen, J. van Buijtenen, P. Colonna, "Dynamic modeling of Organic Rankine Cycle power systems", *J. Eng. Gas Turbines Power*, 135 (042310), 2013.

**Conference papers, posters and presentations:**

T. Mathijssen, M. Gallo, E. Casati, A. Guardone, P. Colonna, "Wave speed measurements in non-ideal compressible flows using the flexible asymmetric shock tube (FAST)", *ASME ORC 2015: 3rd Int. Seminar on ORC Power Systems*, Brussels, Belgium, October 12-14, 2015.

T. Mathijssen, A. Guardone, P. Colonna, "Simulations of compressible flows in the liquid-vapour critical region using non-classical scaling laws", *ASME ORC 2013: 2nd Int. Seminar on ORC Power Systems*, Rotterdam, The Netherlands, October 7-8, 2013.

P. Colonna, M. Gallo, E.I.M. Casati, T. Mathijssen, "Flexible Asymmetric Shock Tube (FAST) set up: status and first experiences", *ASME ORC 2013: 2nd Int. Seminar on ORC Power Systems*, Rotterdam, The Netherlands, October 7-8, 2013.

A. Hattiangadi, T. Mathijssen, M. Lampe, D. Pasquale, J. Gross, A. Bardow, P. Colonna, "Development of a tool for the simultaneous optimization of process and working fluid of ORC power systems", *ASME ORC 2013: 2nd Int. Seminar on ORC Power Systems*, Rotterdam, The Netherlands, October 7-8, 2013.

T. Mathijssen, M. Gallo, E.I.M. Casati, P. Colonna, "Flow measurements in a Ludwieg tube set-up for the experimental investigation of rarefaction shock waves: status report, ECCOMAS 2012, Vienna, Austria, 2012.

F. Casella, T. Mathijssen, J. van Buijtenen, P. Colonna, "Dynamics and Control of ORC Power Systems", *1st Int. Seminar on ORC Power Systems*, Delft, The Netherlands, September 22-23, 2011.

P. Colonna, M. Gallo, E. Casati, T. Mathijssen, P. Repetti, "Flow measurements in transonic flows of organic fluids with a Ludwieg Tube type setup", *1st Int. Seminar on ORC Power Systems*, Delft, The Netherlands, September 22-23, 2011.

T. Mathijssen, W.J. Bannink, E. Scarano, "Investigation of a Sharp-Edged Delta Wing in a Supersonic Flow Using Stereo PIV", *39th AIAA Fluid Dynamics Conference*, San Antonio, TX, no. AIAA-2009-389, June 22-25, 2009.

**Technical reports:**

T. Mathijssen, M. Gallo, E. Casati, P. Colonna, "Tests on the vapour generator of the FAST setup", *Delft University of Technology, Process and Energy Department, Energy Technology Section, Leeghwaterstraat 44, 2628 CA Delft, The Netherlands, Scientific Report ET-2564*, June 2013.